Downloaded from orbit.dtu.dk on: Apr 09, 2024

DTU Library

CFD Modelling of the Impact of Flow Conditions on Scale Formation Processes

Bentzon, Jakob Roar

Publication date:
2023

Document Version
Publisher's PDF, also known as Version of record

Link back to DTU Orbit

Citation (APA):
Bentzon, J. R. (2023). *CFD Modelling of the Impact of Flow Conditions on Scale Formation Processes*. Technical University of Denmark.

General rights
Copyright and moral rights for the publications made accessible in the public portal are retained by the authors and/or other copyright owners and it is a condition of accessing publications that users recognise and abide by the legal requirements associated with these rights.

- Users may download and print one copy of any publication from the public portal for the purpose of private study or research.
- You may not further distribute the material or use it for any profit-making activity or commercial gain
- You may freely distribute the URL identifying the publication in the public portal

If you believe that this document breaches copyright please contact us providing details, and we will remove access to the work immediately and investigate your claim.

DTU Construct
Department of Civil and Mechanical Engineering

CFD Modelling of the Impact of Flow Conditions on Scale Formation Processes

PhD Thesis

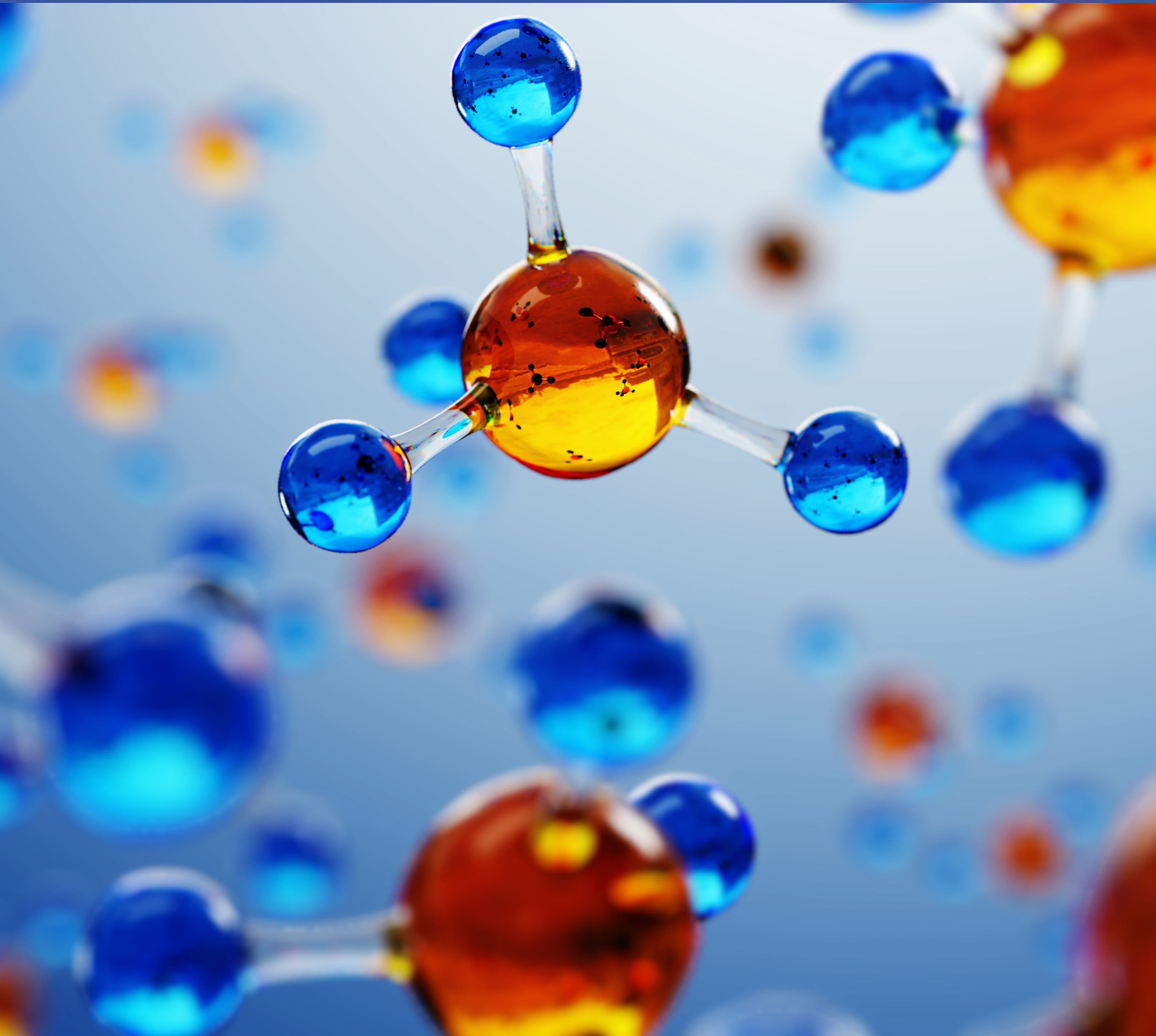

CFD Modelling of the Impact of Flow Conditions on Scale Formation Processes

PhD Thesis	
Submitted:	January, 2023
Prepared by:	Jakob Roar Bentzon
PhD Supervisor:	Jens Honoré Walther
PhD Co-supervisor:	Karen Louise Feilberg
PhD Co-supervisor:	Benaiah Uchechukwu Anabaraonye

Copyright: Reproduction of this publication in whole or in part must include the customary bibliographic citation, including author attribution and report title

Published by: DTU, Department of Civil and Mechanical Engineering, Nils Koppels Allé, Building 403, 2800 Kgs. Lyngby Denmark
www.contruct.dtu.dk

Preface

This thesis is submitted in partial fulfilment of the requirements for obtaining a PhD degree at the Technical University of Denmark (DTU). The PhD project was carried out at the Department of Civil and Mechanical Engineering (Construct) at the Section of Fluid Mechanics, Coastal and Maritime Engineering, in collaboration with DTU Offshore.

The work presented has been carried out between February 2018 and December 2021, with supervision from Professor Jens Honoré Walther and co-supervision from Karen Louise Feilberg and Benaiah Uchechukwu Anabaraonye.

The project was funded by DTU Offshore as part of the cost transformation research programme (CTR 2).

Abstract

Scale formation from mineral crystallization presents a widespread industrial challenge and becomes increasingly costly within modern societies. It is a common cause of process equipment fouling leading to deleterious impacts and sub-optimal operation, resulting in equipment failure, higher energy consumption, and reduced output. Scale prevention and removal processes involve extensive use of reaction inhibitors, solvents, and acids that present a potential threat to aquatic life and ecosystems. Consequently, accurate modelling and prediction of scale formation play a crucial role in efficiently managing the use of such chemicals while minimizing their unfavourable side effects.

While scale formation most commonly causes deleterious effects in the industry, some studies and industries induce scale formation intentionally. A relevant and recent example is the use of carbonate scale as a permanent and stable solution for carbon storage. In such applications, process control and optimization rely on a thorough understanding of the wide range of mechanisms governing crystallization.

Universal to scale formation is the significance of the ionic transport within the fluid from which the scale is crystallized. The present PhD thesis covers work carried out over the last four years to improve the scientific modelling techniques applied in numeric modelling of flow and scale formation. This thesis presents work on computational fluid dynamics (CFD) modelling of the impact of flow conditions on scale formation processes.

The scope of the project is rooted in a specific challenge, namely the formation of barium sulphate scale in the hydrocarbon producing pipelines in the Danish part of the North Sea. Barium sulphate formation incurs significant costs to the industry. The modelling of barium sulphate crystallization processes under flow conditions similar to those faced in hydrocarbon wells require a multi-disciplinary understanding of crystallization.

Barium sulphate formation occurs from the crystallization of barium and sulphate ions within the water. The governing physics of the process is commonly modelled using a thermodynamic equilibrium reaction governed by a transition state from dissolved ions to nuclei and by subsequent growth of those nuclei. This can occur in the fluid bulk as suspended particles or at the interface between the fluid and solids as scale. The rates at which these forming processes occur are controlled by a combination of stochastic processes at molecular scale and larger-scale variations. The molecular scale is studied in the field of physical chemistry, whereas the larger spatio-temporal variations are the subject of three-dimensional modelling methods such as CFD. Within the present PhD thesis, different aspects of the impact of fluid dynamics on barium sulphate formation are examined, and the results have been compiled into research papers.

The first paper published focuses explicitly on the modelling of the turbulent and dispersed two-phase oil-water flow common to the aforementioned pipelines. An implementation of a statistical and adaptive droplet size distribution model into an Eulerian two-fluid model is presented. The model is used to replicate experimental studies of oil-water dispersion quantified through phase distribution and droplet sizes. While the droplet-size distribution results show a notable uncertainty, the ability to dynamically predict droplet sizes significantly aids the ability to determine phase distribution without manual input of droplet sizes. Such modelling helps predict water-wetting, which significantly affects scale formation.

Due to the low solubility of barium sulphate, effective reaction rates are often limited by mixing and transport. Within turbulent flow, mixing is strongly aided by the folding and stretching of fluid structures. At the time of the PhD study, the availability of experimental data to support numerical analysis of these effects was limited. Consequently, the research group decided to build two different flow-reactive experimental setups; a Taylor-Couette reactor and a pipe-flow-through reactor.

Based on experiments using the Taylor-Couette reactor, a research paper has been published on the analysis of turbulent mixing and the impact on barium sulphate reactivity. A validated procedure for such analysis has been presented along with a novel suggestion for a turbulent Peclét number that supports numerical studies of turbulent mixing. The outcome of the paper has given the research group insights into the significance of the hydrodynamics in the reactor for its net reactivity. This research is continued in a subsequent study on inhomogeneous reactivity, which is attached to the thesis as a draft manuscript.

Finally, a phenomenological study of surface barite formation under different surface and flow conditions has been carried out on the pipe-flow reactor. The produced paper discusses transport regimes and how they impact the processes of surface growth. The outcome of the study highlights further areas of research which have been initiated at the time of writing.

In summary, a range of techniques and methods modelling the impact of flow conditions on scale formation have been studied. The process has led to improvements in the current fundamental understanding of scale formation in complex flow conditions. Moreover, a fundamental basis for future research has been laid from the output research papers and data.

Resumé (in Danish)

CFD-modellering af strømningsbetingelsers indflydelse på forkalkningsprocesser

Forkalkning hidrørende fra mineralsk krystallisering udgør et omfattende og tillige stadig mere bekosteligt problem(felt) i det moderne samfund. Forkalkning er ofte årsag til *fouling* på udstyr med skadelige virkninger og nedsat effektivitet til følge. Resultatet er nedbrud af udstyr, øget energiforbrug og nedsat produktion. Forebyggelse af forkalkning kræver ekstensiv brug af *reaction inhibitors*, solventer og syrer, som udgør en potentiel trussel mod vandmiljø og økosystemer. Som følge heraf er nøjagtig modellering og forudsigelighed af kalkdannelse af afgørende betydning for en effektiv brug af de relevante kemikalier med henblik på at minimere deres skadelige bivirkninger.

Mens forkalkning oftest forårsager ødelæggende virkninger i industrien, anvender nogle studier og industrier en målrettet brug af forkalkning. Et nyere relevant eksempel er brugen af mineralske karbonater til stabil deponering af karbondioxid. I denne sammenhæng beror styringen og optimeringen af processen på en grundlæggende forståelse af den brede vifte af mekanismer, som styrer krystalliseringen.

Af afgørende betydning for alle former for forkalkningsprocesser er den ioniske transportproces i den væske, hvorfra kalken udkrystalliseres. Nærværende ph.d.-afhandling er resultatet af fire års arbejde med fokus på at forbedre de videnskabelige metoder i modelleringen af strømning og forkalkning. Afhandlingen præsenterer studier baseret på *computational fluid dynamics* (CFD) modellering af strømningsbetingelsers indflydelse på forkalkningsprocesser.

Projektets fokusområde knytter sig til en specifik problemstilling, nemlig opbygningen af bariumsulfat i olie- og gasproducerende rørledninger i den danske del af Nordsøen. Opbygning af bariumsulfat medfører betydelige omkostninger for industrien. Modellering af bariumsulfat-krystalliseringsprocesser under strømningsforhold svarende til dem, man møder i olie-gas-brønde, kræver en tværfaglig forståelse af krystallisering.

Bariumsulfatdannelse opstår ved udkrystallisering af barium- og sulfat-ioner i vand. Processens fundamentale fysik kan typisk modelleres som en termodynamisk ligevægtsreaktion, som styres af en overgangstilstand fra opløste ioner til kim og af disse kims efterfølgende vækst. Denne proces kan forekomme som suspenderede partikler i væsken eller som kalkaflejringer på overfladen mellem væske og væg. Forkalkningsprocessernes hastighed styres af en kombination af stokastiske processer på mulekylær skala og større variationer. Mens molekylær-skalaen er genstand for den fysisk-kemiske forskning, studeres de større rums- og tidsvariationer på basis af tredimensionale modelleringsmetoder som CFD. I nærværende afhandling undersøges forskellige aspekter af strømningsdynamikkens indvirkning på bariumsulfatdannelse; resultaterne af disse undersøgelser er samlet i nedenstående forskningsartikler.

Den første publiserede forskningsartikel fokuserer eksplicit på modelleringen af de turbulente og dispergerede to-fase olie-vand strømningsforhold som forefindes i førnævnte rørledninger. Heri beskrives en implementering af en statistisk og adaptiv dråbestørrelsesfordelingsmodel i en Eulersk to-faset model. Denne model bruges til at replicere eksperimentelle undersøgelser af olie-vand-dispersion kvantificeret gennem fasefordeling og

dråbestørrelser. Mens resultaterne af dråbestørrelsesfordelingen viser en betydelig usikkerhed, hjælper evnen til dynamisk at forudsige dråbestørrelser betydeligt evnen til at bestemme fasefordeling uden manuel input af dråbestørrelser. En sådan model bidrager til at forudsige *water-wetting*, som påvirker forkalkning betydeligt.

På grund af bariumsulfats lave opløselighed begrænses den effektive reaktionshastighed ofte af sammenblandings- og transportforhold. I turbulent flow er sammenblandingsraten fremmet af foldning og strækning af strømningsstrukturer. Da tilgængeligheden af eksperimentelle data til støtte for numerisk analyse af disse effekter var begrænset på tidspunktet for nærværende ph.d.-studium, besluttede forskningsgruppen at bygge to forskellige flow-reaktive eksperimentelle opstillinger; en Taylor-Couette reaktor og en rørgennemstrømningsreaktor.

Den anden forskningsartikel er baseret på eksperimenter i Taylor-Couette-reaktoren med fokus på analyse af indvirkningen af turbulent blanding på bariumsulfat-reaktivitet. En valideret procedure for en sådan analyse er præsenteret sammen med et forslag til et nyt turbulent Peclét-tal, som understøtter numeriske analyse af turbulent blanding. Resultatet af artiklen har givet forskningsgruppen indsigt i hydrodynamikkens betydning for reaktorens netto-reaktivitet. Denne forskning videreføres i en efterfølgende undersøgelse om inhomogen reaktivitet, som er vedlagt afhandlingen som manuskriptudkast.

Endelig er der udført en fænomenologisk undersøgelse af overflade-bariumsulfatdannelse under forskellige overflade- og strømningsforhold i rør-strømningsreaktoren. I sin publiserede form diskuterer artiklen forskellige transportregimer og hvordan de påvirker forkalkningsprocesserne. Resultatet af undersøgelsen fremhæver yderligere forskningsområder, som er påbegyndt i skrivende stund.

Sammenfattende kan det konstateres at en række teknikker og metoder, der modellerer strømningsbetingelsernes indvirkning på forkalkning, er blevet undersøgt. Denne proces har ført til forbedringer i den nuværende grundlæggende forståelse af forkalkning under komplekse strømningsforhold. Desuden er der lagt et solidt grundlag for fremtidig forskning i de publiserede forskningsartikler og data.

Publications

Benaiah U. Anabaraonye, Jakob R. Bentzon, Ishaq Khaliqdad, Karen L. Feilberg, Simon I. Andersen, and Jens H. Walther, "The influence of turbulent transport in reactive processes: A combined numerical and experimental investigation in a Taylor-Couette reactor," Chem. Eng. J. **421**, 129591 (2021).

Jakob Roar Bentzon, Attila Vural, Karen L. Feilberg, and Jens H. Walther, "Surface wetting in multiphase pipe-flow," Multiph. Sci. Technol. **32**, 137–154 (2020).

Isaac A. Løge, Jakob R. Bentzon, Christopher G. Klingaa, Jens H. Walther, Benaiah U. Anabaraonye, and Philip L. Fosbøl, "Scale attachment and detachment: The role of hydrodynamics and surface morphology," Chem. Eng. J. **430**, 132583 (2022)

A note to the reader

This report wraps the research outcome of the author's PhD scholarship. The format of this report is a 'paper-based' thesis highlighting three published papers and a work-in-progress manuscript. In addition to these research outputs, this report contains an introduction framing the motivation and societal relevance of the presented work, an outline of the fundamental governing physics including the author's notes on the current state-of-the-art, and finally, a summary of the motivation behind the individual research outputs. In essence, the purpose of the introduction is to provide the reader with an overview of the relevant fields and offer the author's justification for the chosen areas of focus but not to present any novel findings.

Author's comments

At the time of the project's initialization, hydrocarbon extraction in the Danish regions of the North Sea remained a critical part of Denmark's energy infrastructure. It was already well-known then, albeit less pronounced than now, that the importance of hydrocarbon extraction was declining. Consequently, it has been the aim of my PhD project to provide broadly applicable contributions to the state-of-the-art knowledge in the field of scale modelling, emphasizing the effects of flow conditions and the advantages of using computational fluid dynamics (CFD). Consequently, the original title of the proposed work: "CFD Analysis of the Impact of the Scale Build-Up on the Liquid Flow in the Wells used for Oil & Gas Production" has been re-scoped to "CFD Modelling of the Impact of Flow Conditions on Scale Formation Processes".

At any rate, the challenges faced in analyzing the impact of scale in oil wells as scoped by the first title would have required initial fundamental studies similar to those carried out in this work. Of equal significance, the outcome of these fundamental studies are generally applicable and broadly contributes to the field of modelling of chemical systems in complex flows. Moreover, current research within carbon capture and storage explores the potential of carbon dioxide mineralization in the form of carbonate scales. As such, the presented work may hopefully contribute to the new strategy of the sponsoring institutions towards carbon capture and storage.

In terms of the produced research papers, the main focus has been on the interaction between the fluid dynamics and the scale precipitation and deposition dynamics. Yet, a single research paper solely focusing on multi-phase oil-water flow was published early in the project. The explanation for this isolated work lies in the practical planning of the PhD work, as in the early stages, we (the research group) did not have any experimental setup available to conduct combined fluid dynamic and kinetic studies. Hence, we conducted a decoupled research based on experiments published by Elseth (2001) and Kumara *et al.* (2009), highlighting methods for analyzing the properties of the oil-water multi-phase flow at conditions similar to those observed in hydrocarbon producing wells.

Contents

Preface ii
Abstract iii
Resumé (in Danish) v
Publications vii
A note to the reader viii
Author's comments viii

1 Introduction 1
1.1 Scope and motivation 1
1.2 Governing physics 2
1.3 Numerical principles 7
1.4 Assessment of the current state-of-the-art 10
1.5 Actions taken in the present work 18
References 24

2 Paper 1: Surface wetting in multiphase pipe-flow 31

3 Paper 2: The influence of turbulent transport in reactive processes: A combined numerical and experimental investigation in a Taylor-Couette reactor 50

4 Paper 3: Scale attachment and detachment: The role of hydrodynamics and surface morphology 64

5 Paper 4: The impact of spatio-temporal variability on the reaction kinetics of miscible fluids 75

6 Conclusion and ongoing work 88
6.1 Conclusions from the published studies 88
6.2 Prospective outcomes of ongoing and future work 89

1 Introduction

1.1 Scope and motivation

Scale formation, i.e., crystallization and adherence of solid material onto a body, is a widespread challenge. The fouling of process equipment, often induced by mineral scale formation, has a deleterious impact on many industries. Examples include efficiency reduction in heat exchangers (Müller-Steinhagen, 2011), flow reduction through filters and membranes (Deshmukh *et al.*, 2018; Sassi and Mujtaba, 2011; Sharifian *et al.*, 2021; Sreedhar *et al.*, 2018), and clogging and subsequent damage to the hydrocarbon producing wells within the petroleum industry (Li *et al.*, 2017; Zhao *et al.*, 2005). However, the formation of scale deposition could also be intentionally induced in some instances. Regardless of its desirability, the understanding and modelling of scale formation are highly relevant to many engineering processes underpinning modern society.

Scales are broadly classified as either organic or inorganic. This study focuses on inorganic mineral scales that form through the crystallization of cation-anion salts. In extracting hydrocarbons from the North Sea, prevention and subsequent removal of barium sulphate scale has proven one of the most costly. Barium sulphate is a near insoluble and mechanically hard scale, making removal difficult. It occurs naturally and is also used widely for industrial purposes such as x-ray imaging (Kresse *et al.*, 2007), highly reflective paints (Li *et al.*, 2021) and enhancement of concrete for radioactive shielding (Gündüz, 1982; Liu *et al.*, 2019). Furthermore, barium sulphate has a simple reaction mechanism compared to more ubiquitous scale types such as calcium carbonate. Therefore, it is widely used as a scaling agent within academia to reduce experimental and phenomenological complexity.

Effective prevention of mineral scale depends on a solid understanding of the fundamental physics (Ruiz-García *et al.*, 2017). Whereas the conceptual mechanisms of scale formation are well understood, due to multiple inter-playing mechanisms such as nucleation, adhesion, detachment and growth, the dynamics and kinetics of scale formation remain a complex and unresolved field (Fischer *et al.*, 2012; Schmelzer *et al.*, 2000).

While fouling is the most common association with scale formation, it is worth highlighting a potential prospect of intended scale mineralization that would benefit from further research. Pogge von Strandmann *et al.* (2019) has shown promising results in utilising carbonate formation (carbonation) to store CO_2. The development of carbon capture and storage technology is becoming increasingly essential with the urgency of climate change mitigation. A key advantage of storing CO_2 through mineralization is the thermodynamic stability of the solid phase; hence its storage is robust compared to stored supercritical CO_2. These methods come at the drawback of being limited by reaction rates and are, therefore, at present, still costly (Neeraj and Yadav, 2020). Intentionally induced formation of minerals has also been studied for reactive barriers in managing nuclear waste (Curti *et al.*, 2019). These examples highlight the potential of mineralization as a tool for long-term storage due to the thermodynamic stability of solid phases.

Fluid transport plays a fundamental role in scale formation. This component has been largely unaccounted for in many kinetic and thermodynamic studies. Supersaturation is typically preceded by the transport and mixing of fluids. In hydrocarbon extraction, injected seawater mixes with reservoir formation water in the well. Similarly, within industrial or laboratory reactors, different brines are mechanically mixed. Under many conditions, reaction kinetic rates are fast compared to the mixing rates, and thus the latter becomes the limiting factor on the net reaction rate (Hjertager *et al.*, 2001). During the mixing, diffusion and turbulent advection are essential for transporting these salts from the fluid bulk to the solid surfaces onto which they attach. Finally, further implications from fluid-fluid interfaces and phase wetting arise in multi-phase flow conditions such as those observed in hydrocarbon extraction wells. Consequently, an enhanced understanding of the coupling between fluid dynamics and scale kinetics will enhance the overall ability to understand and predict mineralization and formation of scale.

With the above-stated motivation for fundamental insights into the effects of hydrodynamics on scale formation, this dissertation will briefly summarise the fundamental governing physics, including the latest research on the topic and a recapitulation of the present work resulting from the PhD project.

1.2 Governing physics

Scale formation is a complex process spanning the traditionally defined scientific disciplines of thermodynamics, physical chemistry, as well as transport processes related to fluid dynamics. For an inorganic scale crystallization, the basis for the process is a dynamic reaction between cations and anions. As an example, barium sulphate precipitates through the reaction of barium cations and sulphate anions:

$$\mathrm{Ba}^{2+} + \mathrm{SO}_4^{2-} \rightleftharpoons \mathrm{BaSO}_4 \tag{1.1}$$

Chemical kinetic rate theory describes the dynamics of chemical reactions. For an elementary reaction, i.e., a reaction with only a single step and a single transition state, the "law of mass action" considers the overall reaction as a combination of a "forward rate" (r_f) and a "backward rate" (r_b). The law of mass action states that the rate of these reactions is proportional to the activity of the reactants (Guldberg and Waage, 1879), such that the forward reaction rate of barium sulphate is described by:

$$r_f = k a_{\mathrm{Ba}} a_{\mathrm{SO}_4} \tag{1.2}$$

where k is a rate constant, a_{Ba} and a_{SO_4} are the chemical activities of barium and sulphate. The law of mass action implies that reaction equilibrium occurs as the rate of the forward and backward reactions are identical. The underlying mechanisms of these rates are studied through the fields of chemical physics and thermodynamics.

1.2.1 Thermodynamics and kinetics of crystallization

Mineral scale formation originates in the crystallization of dissolved cations and anions in a solvent, most commonly water. This process is generally exergonic, i.e., it releases energy to its surroundings and reduces the local entropy of the dissolved species into a well-organized solid lattice, transforming the chemical potential into heat and surface energy.

To determine the state of an equilibrium reaction such as (1.1), the change in Gibbs free energy (∂G) with the change quantity of molecules of each specie (n_i) is considered. The chemical potential is introduced and modelled as (Lewis and Randall, 1961):

$$\mu_i = \partial G / \partial n_i = \mu_i^0 + k_B T \ln(a_i) \tag{1.3}$$

where μ_i^0 is a reference chemical potential, and a_i the chemical activity, k_B is Boltzmann's constant and T is the thermodynamic temperature. The chemical activity of an ionic specie is defined as its molal concentration (m_i) multiplied by an activity coefficient (γ_i).

$$a_i = m_i \gamma_i \tag{1.4}$$

Activity coefficients account for the difference in the chemical potential of the ith specie due to the non-ideal-gas-like behaviour of the solution (Lewis, 1907; Peters, 2017).

$$\gamma_i = \exp\left(\frac{\mu_{i,actual} - \mu_{i,ideal}}{k_B T}\right) \tag{1.5}$$

where the ideal chemical potential corresponds to the ideal-gas-like chemical potential ($\mu_{i,ideal} = k_B T \ln(m_i)$). Various models exist to estimate the activity coefficients; the most commonly applied models are outlined in Section 1.4.3.

Chemical equilibrium is defined as the state where the rate of change in the Gibbs free energy with respect to the extent of the reaction ($\partial \xi$) becomes zero (Lewis and Randall, 1961)

$$\frac{\partial G}{\partial \xi} = \sum_i \nu_i \mu_i = 0 \longrightarrow \textit{Chemical Equilibrium} \tag{1.6}$$

where ν_i is the stoichiometric coefficient of the ith specie. The extent of the reaction is defined as $\partial \xi = \partial n_i / \nu_i$. By introducing the solubility product K_P as the "constant" reference part of the potential,

$$\ln(K_P) = -\frac{\sum_i \nu_i \mu_i^0}{k_B T} \tag{1.7}$$

the equilibrium formulation (1.6) can be rewritten as $\prod_i a_i^{\nu_i} / K_P = 1$. A saturation state Ω is introduced as:

$$\Omega = \frac{\prod_i a_i^{\nu_i}}{K_P} \tag{1.8}$$

With such definition we can easily obtain the surplus Gibbs energy for a given saturation state as

$$\Delta G = k_B T \ln \varOmega \tag{1.9}$$

In a super-saturated brine ($\varOmega > 1$), the energy level of a precipitated crystal is preferable over that of the dissolved ions. However, the crystallization process typically has an unstable transition state between the dissolved state and the solid crystal states. In this transition state, the dissolution of the crystal is predominant. Consequently, sufficient anions and cations have to collect through collisions for a stable crystal to form. Using statistical mechanics, transition state theory models this stochastic process using the level of thermal energy as a driver for the rate of formation of stable crystals. The energy-level after which a crystal becomes stable, i.e., further growth of the crystal is fully exergonic, is referred to as the Gibbs free energy of activation (ΔG_A). Based on transition state theory and originating in Boltzmann statistics and the Maxwell-Boltzmann distribution, different models have been developed to determine the rate at which the transition to a meta-stable state occurs (Arrhenius, 1889; Eyring, 1935). These models agree on the "forward kinetic rate constant", k_f, being proportional to the Boltzmann factor, i.e., to the negative exponential function of the ratio between the Gibbs free energy of activation and the product of Boltzmann's constant and the temperature (T):

$$k_f \propto \exp\left(-\frac{\Delta G_A}{k_B T}\right) \tag{1.10}$$

Classical nucleation thermodynamics describes the Gibbs free energy of activation as the difference between the cost of surface formation and the release of chemical energy. This field has been the base for nucleation across many disciplines, such as droplet condensation in vapour and cavitation in water. Herein, by modelling the Gibbs free energy of activation as a function of nucleus size, the activation energy can be found as the maximum energy state, after which further growth reduces the net Gibbs free energy of the nucleus. An assumption of the nucleus geometric assumption must be taken to determine the relationship between volume and surface area. As shown in figure 1.1, the activation energy is the maximum of the Gibbs free energy as a function of the crystal size (Mullin, 2001).

The nucleation process may occur either "isolated" in the fluid bulk or attaching to foreign interfaces of the solvent. These two processes are categorized as homogeneous and heterogeneous nucleation, respectively. In classical nucleation theory, the thermodynamic difference between the two nucleation processes is typically described using geometric considerations, most commonly that the nuclei are spherical. With a surface tension (σ) and a molar volume of the crystal (V_m), a spherical nucleus becomes stable after reaching its critical Gibbs free energy level (ΔG_c):

$$\Delta G_c = \frac{16\pi\sigma^3 V_m^2}{3\left(N_A k_B T \ln\left(\varOmega\right)\right)^2} \tag{1.11}$$

where N_A is Avogrado's number. For heterogeneous nucleation, the spherical assumption may be altered to account for a different surface-to-volume ratio, thereby lowering the activation energy. This correction is done by introducing a contact angle θ between the

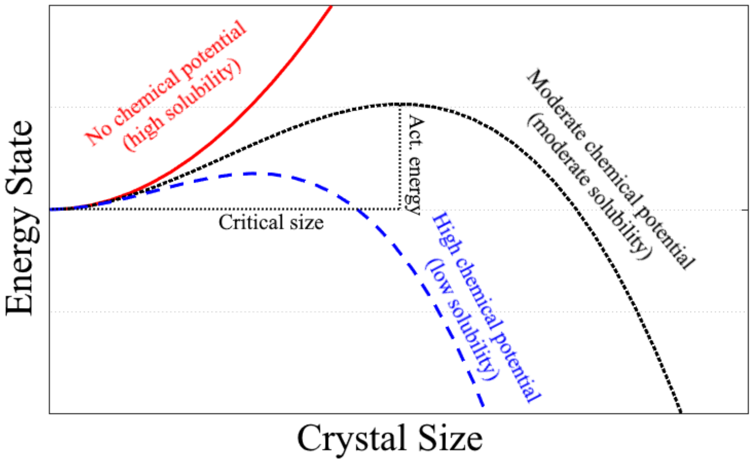

Figure 1.1: Illustration of the Gibbs free energy of activation at different solubility levels.

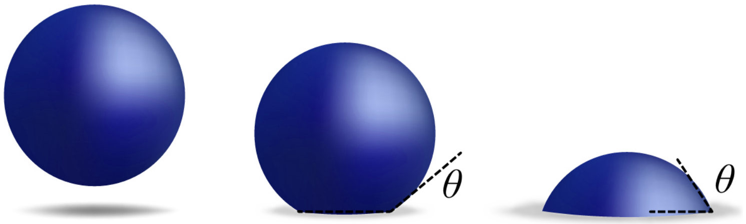

Figure 1.2: Depictions of the spherical nucleus assumptions. Left: Homogeneous nucleation. Middle: Heterogeneous nucleation with a high contact angle ($\theta > 90°$). Right: Heterogeneous nucleation with a low contact angle ($\theta < 90°$).

fluid and the surface as illustrated in Figure 1.2, yielding a partial sphere with the resulting change in activation energy (Mullin, 2001; Volmer, 1939):

$$\Delta G_{c,het} = \frac{(2+\cos\theta)(1-\cos\theta)^2}{4}\Delta G_c \tag{1.12}$$

The term $(2+\cos\theta)(1-\cos\theta)^2/\,4$ takes values between zero and one, and thus (1.12) suggests that heterogeneous nucleation has lower activation energy compared to homogeneous nucleation. It should be noted that other effects such as surface charge might affect nucleation differently than accounted for by the contact angle. Finally, non-smooth surfaces can further alter the formation of the surface nuclei (Grosfils and Lutsko, 2021; Gunn, 1980; Zhang *et al.*, 2015a).

From classical nucleation theory to bridge to reaction kinetics, the statistics of the stochastic process of forming stable crystals are condensed down to a nucleation rate, that is, the rate at which stable crystals (nuclei) are formed. The nucleation rate (J_n) can be modelled using an Arrhenius equation:

$$J_n = A_n \exp\left(-\frac{\Delta G_c}{k_B T}\right) \tag{1.13}$$

where A_n denotes the pre-exponential factor corresponding to the "ideal" nucleation rate if $\Delta G_c \ll k_B T$. Regarding A_n, it should be noted that derived for homogeneous nucleation, it has the units of frequency per volume, whereas, for heterogeneous nucleation, it becomes frequency per area. The fundamental physics of A_n has been studied but is generally complex and most commonly determined experimentally.

By assuming the shape of the crystals and by calculating the volume and therefore the number of moles of specie i for a meta-stable crystal ($n_{c,i}$), the primary nucleation reaction rate can be determined from (1.13):

$$r = n_{c,i} J_n \tag{1.14}$$

Subsequent to the formation of nuclei, crystal growth is governed by ions attaching to the existing nuclei, agglomeration from nuclei collisions, and on-surface coalescence. While the crystal growth process is not subject to the same critical size barrier as nucleation, it is still driven by the stochastic process of ion collisions and could include additional transition states. Similarly to the process of nucleation, this stochastic process may be described by statistical mechanics focusing on the activation energy of the transition state. Eyring's equation gives an analytical definition of a rate employing such characterization:

$$k = \frac{\kappa k_B T}{h} \exp\left(\frac{-\Delta G_A}{k_B T}\right) \tag{1.15}$$

where ΔG_A is the Gibbs energy of activation and h is Planck's constant, κ is often referred to as a "transmission coefficient" accounting for effects such as activation collision angles and statistical state dependencies (Eyring, 1935). While κ could be statistically determined from the system, it is typically experimentally determined due to the complexities of a liquid phase mixture. Most studies assume that the effect of temperature changes on the pre-exponential factor is negligible and fit experimental data to the simpler Arrhenius equation (Arrhenius, 1889).

The physics and thermodynamics of the system demonstrate how a range of different processes and transition states govern the formation and growth of scale. Depending on the underlying chemical reaction, scale formation may occur in different mechanisms undergoing multiple steps. Each of these mechanisms can generally be deconstructed into sets of elementary processes. The interplay and dominance of each of these mechanisms then become highly dependent on space and time and thus spatio-temporal modelling through, e.g., computational fluid dynamics.

1.2.2 Fluid dynamics

The previous section examines the governing physics from a molecular scale to a statistical level in a well-defined thermodynamic ensemble. In the vast majority of engineering applications, spatial and temporal variations in the concentrations and thermodynamic state play a significant role, and thus the simulation of transport processes is essential.

Computational fluid dynamics (CFD) is a standard numerical strategy for resolving the spatio-temporal variability of conserved quantities in fluids. CFD utilizes finite difference and finite volume discretization of the governing conservation equations in space and time.

The governing equations may be defined in a Lagrangian or Eulerian description; Lagrangian models describe the physics from the perspective of the moving object, such as a particle, whereas Eulerian models describe the physics from a given reference frame in which the object moves. Both descriptions may resolve a given system at a sufficiently fine resolution, but each has its advantages in terms of computational efficiency. Lagrangian models allow more direct modelling of particle-particle interactions, whereas Eulerian models rely on higher-order statistical modelling of quantities such as particle concentration. Consequently, Eulerian CFD models are often affected by numerical diffusion of concentrations due to grid interpolation. However, as the number of particles increases, an Eulerian description becomes computationally cheaper than the Lagrangian approach (Loth, 2000; Shirolkar *et al.*, 1996) and, thus, offers higher precision at limited computational resources. Throughout the presented studies, Eulerian models are applied across all the governing physics, specifically the transportation of chemical species and precipitated solids, and the conservation of fluid momentum and mass.

Concentrations of ionic species and dilute crystallized products can be simulated as passive scalars, thereby omitting their effects on the fluid properties and neglecting their momentum, or simulated as separate phases through momentum and mass conservation. In the scope of the present work, the modelled concentrations are sufficiently low and hence the effects of their presence on the fluid dynamics negligible. The Eulerian description for advective-diffusive transport of a passive molal concentration m is

$$\frac{\partial m}{\partial t} = \nabla \cdot (D \nabla m) - \nabla \cdot (\mathbf{u}\, m) + S \tag{1.16}$$

where D is the molal diffusivity of m, $\mathbf{u}$ is the velocity vector field, and S is a source term arising from chemical reactions. The velocity vector field is obtained by solving the equations of mass and momentum conservation, namely the Navier-Stokes equations:

$$\frac{\partial \rho_f}{\partial t} + \nabla \cdot (\rho \mathbf{u}) = 0 \tag{1.17}$$

$$\frac{\partial}{\partial t}(\rho_f \mathbf{u}) + \nabla \cdot (\rho_f \mathbf{u} \otimes \mathbf{u}) = -\nabla p + \rho_f \mathbf{g} + \nabla \cdot \sigma \tag{1.18}$$

where ρ_f is the fluid density, p is the pressure and σ is the Cauchy stress tensor. For an incompressible flow (constant density) with a constant Newtonian viscosity μ_f, the term $\nabla \cdot \sigma$ can be simplified to $\mu_f \nabla^2 \mathbf{u}$. The symbol $\otimes$ denotes the tensor product of the velocity vector field.

1.3 Numerical principles

The governing equations are solved on a discrete computational grid. Whereas some CFD implementations use the finite element methods (FEM), most CFD codes employ the finite volume method. The gradient operators and time derivatives are approximated using finite difference schemes. While these methods ensure convergence of the solution at sufficiently fine grids, grid sizes larger than the smallest wavelengths of variations would induce truncation errors on the derivative approximation. Direct numerical simulation

(DNS) classifies numerical CFD simulations with a grid size that resolves all relevant gradients, thereby solving the governing equations to numerical accuracy. While such simulations are scientifically preferable, computational resource limits make such simulations highly time-consuming and rarely feasible. Where DNS is infeasible, higher-order statistical physics can be introduced into the numerical models. Common examples include the modelling of the effects of turbulence and of the effects of interfacial forces in multi-phase flow.

1.3.1 Modelling the effects of turbulence

Turbulence arises from instabilities of the fluid motion causing chaotic, complex fluid flow patterns. From a mathematical perspective, the chaotic solution to Navier-Stokes equations arises from the non-linear momentum advection term ($\mathbf{u}\otimes\mathbf{u}$). Hence, turbulence is often expected when the magnitude of this term is high compared to the momentum-diffusive term from viscosity. This ratio is commonly described through the Reynolds number of the flow:

$$\mathrm{Re} = \frac{\rho_f U L}{\mu_f} \tag{1.19}$$

where U and L are characteristic velocity and length scales of the flow, respectively.

In turbulent flow conditions, the scale at which variability and thus heterogeneity occurs has been analyzed in (Batchelor, 1959). In a turbulent diffusion-advection system, the Batchelor length scale describes the smallest wavelengths at which variations in concentrations and temperature can be sustained. For most chemical solutions in water, the ratio of the momentum to molecular diffusivity denoted by the Schmidt number (Sc) is multiple orders of magnitude larger than one. Under such conditions, the Batchelor length scale becomes much smaller than the Kolmogorov length scale, which describes the smallest velocity fluctuation.

DNS simulations of turbulent flows would require a computational grid size smaller than the Kolmogorov and Batchelor length scales. Unfortunately, the Kolmogorov and Batchelor length scales get progressively smaller as the Reynolds number increases. Consequently, the most common compromise is to “Reynolds decompose” the equations, i.e., separating each quantity into a fluctuating and a Reynolds-averaged component. With such decomposition, the Navier-Stokes equations can be rewritten into the equations for the average component. This method is commonly known as Reynolds Averaged Navier-Stokes (RANS). As most engineering problems focus on time-averaged metrics, it makes sense not to resolve the fluctuations. However, from the decomposition of the governing equations, it follows that the fluctuations play a role in the non-linear terms of the time-averaged equations. Consequently, the field of turbulence modelling delves into methods of modelling these effects rather than resolving them.

As computational power has increased over the last decades, another method, large eddy simulation (LES), has gained popularity. This method filters the governing equations spatially rather than temporally, allowing both temporal and spatial modelling of variations down to the computational grid size of the model. Consequently, LES is generally considered a middle ground between RANS and DNS modelling. Like RANS decomposition, the filtering of sub-grid-scale eddies leaves an artefact in the filtered equations that LES

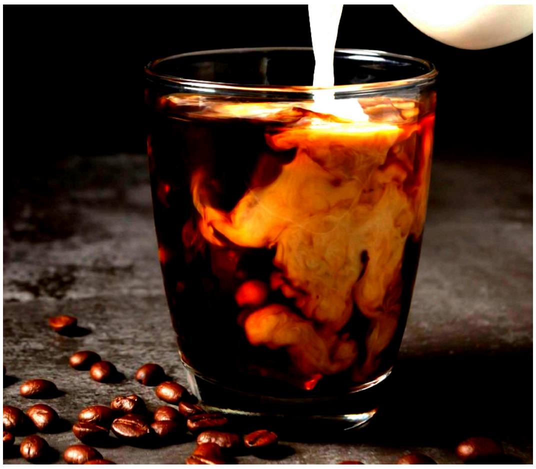

Figure 1.3: Illustration of chaotic mixing of two brines through stretching and folding.

relies on turbulence modelling to resolve. Frequently, LES models provide significantly better accuracy, as the spatially smaller eddies are more homogeneous and isotropic, and therefore the applicability of the turbulence models becomes increasingly general and accurate.

Turbulence modelling has historically focused on the effects of the filtered fluctuations in the velocity field on the diffusion of momentum. This term arises from the filtering of the Kronecker product ($\mathbf{u} \otimes \mathbf{u}$). As the effect of this term mathematically corresponds to added diffusion of momentum, it is dubbed turbulent viscosity or sub-grid-scale viscosity when referred to in LES modelling. For LES modelling, the Dynamic Smagorinsky model (Germano *et al.*, 1991; Meneveau and Katz, 2000) and the wall-adaptive large eddy (WALE) model (Nicoud and Ducros, 1999) have both proven accurate in a range of engineering applications. Within RANS simulations, algebraic models such as the Spalart-Allmaras (Spalart and Allmaras, 1992) and two-equation transport models such as the k-ω (Wilcox, 1988) and k-ϵ model (Launder and Sharma, 1974) are most commonly applied. These models regard the turbulent viscosity as an isotropic quantity, i.e., they assume that the mean diffusion of momentum due to turbulence is uniform in all three Cartesian directions. For situations where turbulence is anisotropic, Reynolds Stress Models (RMS) formulates tracking of a full 3×3 stress tensor. Thus, the best choice of turbulence modelling technique for a given study highly depends on the isotropy of the turbulence and on whether the resolution of the finer eddies is of interest.

Similarly to the increased diffusivity of momentum, when filtering the transport equation (1.16), an additional concentration-diffusive flux arises from the convective term ($\nabla \cdot \mathbf{u}\, m$). The modelling of this diffusivity is typically done through some relationship with the aforementioned turbulent momentum diffusivity. Increased mixing from turbulence occurs due to increased diffusion caused by stretching and folding of interfaces between volumes of higher and lower concentration (Kelley and Ouellette, 2011; Ottino, 1989; Southerland *et al.*, 1994). As an illustrative example, Figure 1.3 shows such effects on a human-visible scale as milk and coffee are mixed.

It is essential to recognize that the added turbulent diffusivity term accounts for an added diffusive flux from one cell to its neighbours. Internally in a CFD finite-volume cell, the concentrations are assumed uniform, effectively filtering away variations smaller than the grid size.

The filtering of sub-grid scale concentration variations impacts the net reactivity within each cell. Turbulence kinetic interaction modelling accounts for the in-cell reactivity dependence on turbulence. Where kinetic rates follow the law of mass action, the reaction rate of a simple system ($A + B \rightleftharpoons P$) in a finite volume cell of volume V with constant density can be calculated as

$$\frac{dm_A}{dt} = \frac{dm_B}{dt} = -\frac{1}{V}\int_V k a_A a_B dV \tag{1.20}$$

In the hypothetical case of perfectly homogeneous reactant concentration throughout a cell, the activities are spatially uniform and equal to the cell average. Thus the right-hand side simplifies to $-ka_A a_B$. However, in the case of local variations within the cell sustained by a concentration gradient across the cell, the cell-averaged rate from (1.20) will differ significantly from the homogeneous case. As such, it is necessary to account for changes in the net cell reaction rate due to concentration variations filtered away through either Reynolds averaging or spatial filtering.

1.3.2 Implications of multi-phase flow

In the case of multiple immiscible fluid phases, such as oil and water flow, added complexity arises from momentum-interaction between the phases. Such flow adds further complexity to the Navier-Stokes equation through complex variations in density and viscosity and added surface tension forces. Commonly applied multi-phase flow modelling techniques consider each phase discrete, either by solving a set of momentum equations for each phase, or by tracking the phase distribution through an Eulerian transport equation. Alternatively, Lagrangian tracking of the droplets of one phase in the other can prove effective for dispersed droplets. For the Eulerian methods, DNS can be achieved by fully resolving the gradients of the interfaces between the fluids. However, achieving such resolution is seldomly possible in dispersed or transitional flows. Eulerian models can therefore be supported by empirical formulations for unresolved interface interaction, e.g., by assuming sub-grid droplet sizes and applying transfer of momentum between the phases based on these assumptions.

Within modelling of mineral deposition, the effects of multi-phase flow conditions may significantly affect formation rates. Typically, scale reactions only occur within the aqueous phase, and consequently, phase distribution may significantly govern the spatio-temporal reactivity. Due to the accelerated crystallization from heterogeneous nucleation and because surface deposition generally is principal in fouling, the degree to which the wall is in contact with water, i.e., water-wetting, becomes an essential metric for scale formation in multi-phase flow.

1.4 Assessment of the current state-of-the-art

Throughout the last century, modelling methods for crystallization prediction and physical chemistry have been studied extensively (Asimov, 1965). However, due to the complexities and non-linear behaviour of most real-life systems, most studies have focused on simplified systems. Experiments aimed at extracting reaction rates and determining kinetic model parameters were, until the emergence of CFD, generally limited to the assumptions that the reactants within their reactor were homogeneously distributed (commonly referred to as perfectly stirred reactors). However, with the emergence of computational modelling techniques and the increase in computational resources, increasingly complex problems can be solved without such homogeneity assumptions (Harris *et al.*, 1996).

In the last decades, DNS studies modelling the kinetics of simple reacting turbulent flows have been published (Minamoto *et al.*, 2015). However, DNS remains infeasible for many systems. RANS and LES models are widely applied for most industrially relevant studies. Examples include studies of diesel combustion (Bösenhofer *et al.*, 2018; Lysenko *et al.*, 2014), corrosion (Jain *et al.*, 2019; Rani *et al.*, 2014), polymerization (Wei *et al.*, 2001; Xu *et al.*, 2017), and, neutralization (Rizzotto *et al.*, 2019). Different models have been proposed within these coarser-discretized simulations to account for the filtered effects of inhomogeneous reactivity.

The eddy dissipation concept (EDC) proposed by Magnussen (1981) is commonly used to account for inhomogeneous reaction rates sub-grid to the computational cell scale. In EDC implementation, a correction factor related to the turbulent intermittency is applied to the reaction rate corresponding to a homogeneous reaction. The fundamental assumption for such correction is that the reaction predominantly occurs within the intermittent fine structures of the turbulence. With this assumption, the model proposes an explicit algebraic correction of the reaction rate and thus does not yield any significant increase in computational costs. The EDC model has been applied in various fields, including combustion modelling (Lewandowski and Ertesvåg, 2018; Panjawani *et al.*, 2010) with success.

Attempts have been made to use the EDC to model liquid phase reactors. Examples include the work by Hjertager *et al.* (2001) and Rizzotto *et al.* (2019) to simulate the experiments by Pohorecki and Baldyga (1983). These studies indicated limits to the EDC model's ability to accurately capture the micro-scale mixing rate indicated by a reaction zone length.

One key challenge to the EDC assumptions is its binary-like consideration of the reaction. In general features, the EDC model yields a measure of the fraction of the cell in which turbulent mixing is sufficient to drive the reaction. An alternative to the EDC approach is to model a probability density function (PDF) of the cell concentrations rather than just the mean (Pope, 1985). From a PDF of each reactant, their joint probabilities and thereby the reaction rate probability can be obtained directly through the reaction model. Such an approach adds valuable information about the kinetic model to the sub-grid scale reactivity. In work by Hjertager *et al.* (2001), it is shown that the PDF models yield better results than the EDC-based models.

A key challenge in the PDF approach is the sub-grid covariance between reactants. The simplest models assume no correlation between each reactant concentration. As the variance is partly driven by fluid displacement, such an assumption is, unfortunately, unlikely to represent reality, and thus, we would expect a negative covariance between reactant concentrations.

The aforementioned techniques give the theoretical foundation for accurate numerical modelling of scale precipitation at an engineering scale. However, few studies have managed to implement such complex modelling practices. Moreover, experimental data necessary to validate and tune the models on turbulence kinetic interaction within crystallization processes is scarce.

1.4.1 Advances in the understanding of crystallization on fluid-solid boundaries

Regarding the effect of the fluid-solid interaction on surface crystallization, experimental research has been carried out to establish an understanding of the shape and rate at which crystals form on different surfaces. These studies outline the wide range of phenomena that occur in the near-solid parts of a reacting flow. Consequently, accurate modelling of the initial surface nucleation rate has a significant degree of uncertainty. Mullin (2001) provides a summary of the theories suggested from a range of the studies on nucleation and subsequent growth upon solid-fluid boundaries carried out leading up to the 21st century.

A velocity gradient is present in most cases of a solid-fluid boundary as one phase moves faster than the other. Consequently, shear forces transfer momentum from one phase to the other. Shear forces result from short-range interaction between the molecules across the interface. As the velocity gradient increases the interaction between the fluid and the solid becomes stronger. It is debated how such interaction may increase deposition rates due to more frequent collisions of ions on the surface yet also increase the detachment of deposited material as shear forces may break off crystals from the surface.

Heterogeneous nucleation onto a solid boundary often appears to be thermodynamically preferable due to lower energy barriers than bulk nucleation. However, certain foreign solid particles may also inhibit nucleation in some instances. In most cases of mineral crystallization, the presence of impurities in the liquid bulk or of solid surfaces enclosing the fluid has shown a significant increase in nucleation rates (Mullin, 2001).

The conditions of a given surface, such as a metal wall, have been shown to affect nucleation significantly (Kazi *et al.*, 2010; Keysar *et al.*, 1994). Surface roughness is generally assumed to enhance heterogeneous nucleation by adding “seed” locations where conditions are preferable for nucleation. Such seed locations could arise from either thermodynamic or hydrodynamic conditions.

Furthermore, as initial crystals have grown either attached to surfaces or in the fluid bulk, secondary nucleation, i.e., nucleation enhanced by the presence of existing nuclei, has been shown to accelerate the overall nucleation rate. A range of fundamental processes has been suggested to contribute to secondary nucleation, including detachment and fragmentation of initial crystals from shear forces or collisions (Strickland-Constable, 1968).

The growth of existing crystals, suspended in the liquid bulk or stationary on a fluid boundary, is governed by a different thermodynamic process compared to nucleation. While different theories have been proposed on the surface growth mechanism, most interpretations are grounded in Gibbs-Volmer adsorption layer theory (Volmer, 1939). The theory proposes an intermediate step in which ions are adsorbed but not yet integrated into the surface lattice. After this adsorption, they will migrate across the crystal surface to a stable location where they are finally bound. The driving supersaturation and molecular struc-

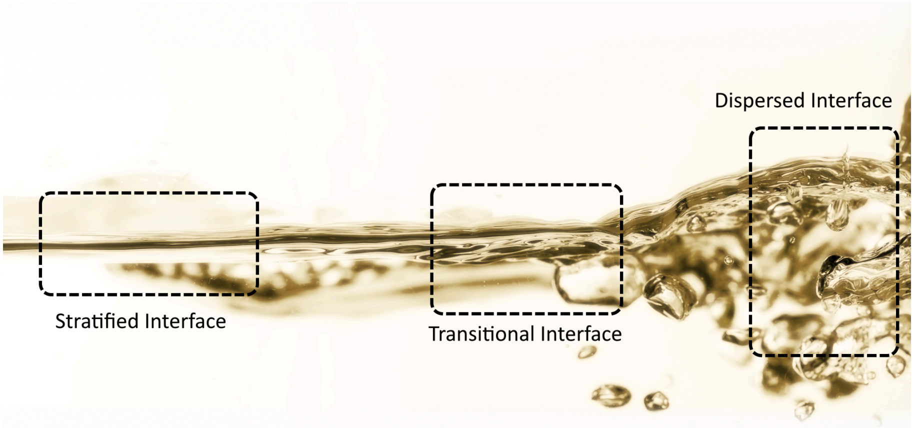

Figure 1.4: Illustration of two-phase flow interface regimes.

ture may lead to different growth patterns and rates. For example, low supersaturation may lead to a layered growth where small islands expand until covering the surface. In contrast, higher saturation levels may cause more dendritic growth, where tree-like structures grow at the corners and tips of the crystals.

The morphology and mechanisms of the growth may play a significant role in the rate at which surface deposition occurs. As such, further degrees of complexity are added to net reaction rates. Furthermore, the growth on a surface leads to local consumption of the reacting species and consequently increases the significance of transport limitations on the reacting system. The entanglement of all of these mechanisms has made modelling of surface deposition a complex subject. The current scientific state-of-the-art offers limited coherence and consistency in its best practices.

1.4.2 Advances in the modelling of multi-phase flow

Similar to interfaces with solid boundaries, fluid-fluid interfaces such as those between oil and water play an important role in both hydrodynamics and reactant mixing. Similarly, the presence of multiple phases adds further complexity to the flow. Multi-phase flow research is predominantly focused on liquid-gas interfaces such as water-air or water-vapour. Examples include modelling of coolant boiling, ocean waves and liquid sprays (Gurakov *et al.*, 2020; Mikkelsen and Walther, 2020; Zhang *et al.*, 2015b).

A key challenge in multi-phase modelling arises as our current computational models are suited for either large flow interfaces which can be partially resolved computationally and tracked, or for dispersed flows in which the interfaces are so small but quantitatively many that they are described more accurately with a statistical representation sub-grid to the cells. Consequently, model choice highly depends on the flow regime sought to be modelled. In general, as the ratio of fluid inertia to surface tension, described by the Weber number (We) is critically high, stratified surfaces become unstable, and the flow regime moves towards a dispersed flow. Figure 1.4 illustrates the complexity of such a transition from a stratified to a dispersed flow.

While the governing theory is similar to water-vapour flow, a few critical aspects of oil-water flow are worth highlighting. Unlike water-air or water-vapour, the interface between water and oil can be considered immiscible, i.e., with a sharp interface. Similarly, it is reasonable to assume that no fluid mass is transferred across the interface. From a modelling perspective, the interaction between the two phases is limited to the transfer of momentum and possibly other scalar quantities such as heat or chemical concentration. Furthermore, the density difference between oil and water is much smaller than between water and air. The density difference is often characterized by the Atwood number:

$$A = \frac{|\rho_1 - \rho_2|}{\rho_1 + \rho_2} \tag{1.21}$$

The Atwood number is an integral parameter in the stability of stratified fluid-fluid interfaces. It is most well known for its appearance in the stability analysis of the Rayleigh-Taylor instability (Rayleigh, 1882; Taylor, 1950) and the Richtmyer-Meshkov instability (Meshkov, 1969; Richtmyer, 1960). It is also inversely proportional to the Richardson number, which is the governing factor in the Kelvin-Helmholtz instability (Goldstein, 1931; Taylor, 1931). In essence, as the Atwood number of oil-water flows is relatively low, the interface between the fluid is relatively unstable, and the transition to dispersed droplet flows occurs more quickly.

Dispersed oil-water flow modelling may play a substantial role in the crystallization processes that occur in hydrocarbon wells. It is generally accepted that the ionic species responsible for barite crystallization only dissolve into water and not into oil. Consequently, the fluid interfaces affect the transport of these species within the water phase as these interfaces may act as barriers. Another significant effect of the oil-water interface is the potential dissolution of other compounds, including sulphur, from the oil into the water. The addition of sulphur into the water may affect the formation of scales and yield other problems for the hydrocarbon industry, including more toxic produced water that requires extensive treatment prior to disposal.

Dispersed multi-phase flows are commonly characterized by a continuous phase in which droplets of the other phase are suspended. Due to the number-density and sizes of the suspended droplets, adequate resolution of the interface of each droplet is seldomly possible. Instead, the multi-fluid models wherein each fluid is solved with a separate set of momentum equations have been widely used (Prosperetti and Tryggvason, 2007).

In modelling such two-fluid flows, droplet drag and lift models may be introduced into the momentum equations. Such models rely on an assumed droplet shape, e.g., a sphere and an expression for the droplet size. Such expression may be algebraic such as the droplet size model proposed by Brauner (2001) or can be modelled using discrete or analytical probability density functions for tracking the distribution of droplets, such as the model proposed by Lo and Zhang (2009).

With the two-fluid approach, the droplet sizes become an essential parameter for characterizing the effects and behaviour of dispersed oil-water flows. Before the prevalence of numerical multi-phase modelling, empirical prediction models have been proposed (Brauner, 2001; Hinze, 1955). While these models are experimentally tuned and vary, they mostly agree that the droplet sizes mainly depend on the Reynolds number and Weber number of the continuous phase.

The water-air interface may also be essential to resolve within simulations of experiments conducted in stirred water reactors. Here, a free surface between the water and surrounding

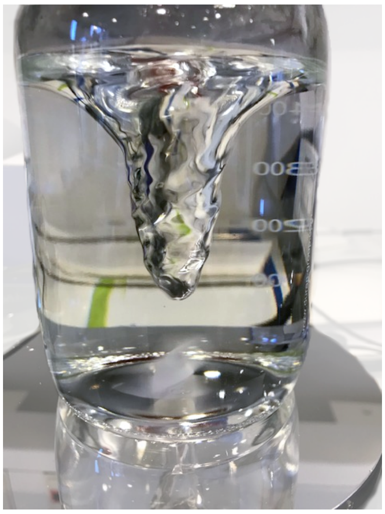

Figure 1.5: Stirred reactor with free air-water surface.

air is present. As the water phase is stirred to mix the brine, this free surface curves from the centrifugal effects, significantly altering the state of the flow in terms of turbulence characteristics and shear forces.

Whereas dispersed flow modelling often is carried out by using a multi-fluid approach, free surface simulations focus on resolving the interface shape between the fluids. The most commonly applied method is the volume-of-fluid (VOF) approach (Hirt and Nichols, 1981). Such simulations have, over the last decades, been successfully applied to a range of simulations such as maritime modelling,

1.4.3 Advances in thermodynamic and kinetic modelling of barium sulphate

Within the thermodynamic modelling of electrolyte chemistry, the activity coefficients of species have been a central focus of research. The main driver for this focus has been that mixtures are highly complex in most engineering aspects and, as a consequence, deviate significantly from ideal-solution-like behaviour. However, even under more idealized experimental conditions, highly insoluble minerals like barium sulphate are significantly affected by the presence of other ionic species.

The concept of chemical activity is introduced to account for the observed difference between the chemical potential of a reactant in a given mixture (μ_i) and its potential in a defined standard state (μ_i^0):

$$k_B T \ln{(a_i)} = \mu_i - \mu_i^0 \tag{1.22}$$

where the standard state is defined as a pure mixture of 1 molal of that reactant (Guggenheim, 1929; Pitzer, 1986). A molal activity coefficient γ_i is introduced as the ratio of the reactant's activity to its molality m_i:

$$\gamma_i = \frac{a_i}{m_i} \tag{1.23}$$

Activities are typically measured experimentally in cation-anion pairs. As such, it makes sense to define a mean activity coefficient $\gamma_{\pm}$:

$$\gamma_{\pm} = \left(\prod_i \gamma_i^{\nu_i} \right)^{1/(\sum_i \nu_i)} \tag{1.24}$$

In dilute ideal solutions, the activity coefficient limits towards unity, whereas for a mixture of increasing complex interaction with other species, the activity coefficient is typically lower than one. Early work on establishing a model for the activity coefficients includes the work by Debye and Hückel (1923), commonly known as the "Debye-Hückel model". In general, the Debye-Hückel models are known to provide accurate results in fairly dilute solutions. Under these conditions, the activity coefficient is considered to mainly be affected by the ionic strength, $I = \frac{1}{2}\sum_j m_i Z_i^2$:

$$\ln \gamma_i = -\frac{A Z_i^2 \sqrt{I}}{1 + B d \sqrt{I}} \tag{1.25}$$

where d is the effective diameter of the ion in angstrom, A and B are thermodynamic temperature-dependent parameters for the solvent (water):

$$A = \frac{N_A^2 e^3 \sqrt{2\rho}}{8\pi\epsilon_0\epsilon_r k_B T \sqrt{\epsilon_r\epsilon_0 N_A k_B T}} \quad , \quad B = \frac{2 N_A e \rho}{\sqrt{\epsilon_r \epsilon_0 N_A k_B T}} \tag{1.26}$$

where e is the elementary charge, ϵ_0 is the permittivity of vacuum, ϵ_r is the dielectric constant of the solvent and ρ the density of the solvent. In solutions with sufficiently low ionic strength, the activity coefficient limits towards:

$$\lim_{I \to 0} \ln \gamma_i = -A Z_i^2 \sqrt{I} \tag{1.27}$$

This is referred to as the "Debye-Hückel Limiting Law".

For molal concentrations larger than approximately 0.01 molal, short-term interactions, which are not accounted for in the Debye-Hückel model, start affecting the activities (Pitzer, 1973; Thomsen, 1997). To better account for these, Kenneth S. Pitzer proposed a model now widely known as the "Pitzer model" (Pitzer, 1973, 1977). Herein, a virial expansion of the excess Gibbs free energy is used to include the effect of more complex ionic interactions.

$$\frac{\Delta G_{ex}}{w_w RT} = f(I) + \sum_i \sum_j m_i m_j \lambda_{ij}(I) + \sum_i \sum_j \sum_k m_i m_j m_k \mu_{ijk}(I) + ... \tag{1.28}$$

where w_w is the mass fraction of the solvent (water), the matrixes λ_{ij} and μ_{ijk} consist of the interaction coefficient with the other ions in the mixture and are symmetric and a function of the ionic strength. The function $f(I)$ accounts for the long-range interactions:

$$f(I) = -\frac{4IA_\phi}{b} \ln\left(1 + b\sqrt{I}\right) \tag{1.29}$$

where b is a constant set to $1.2\,[\mathrm{kg}^{1/2}\mathrm{mol}^{-1/2}]$. From the excess free Gibbs energy, the activity coefficients can be determined as:

$$\ln(\gamma_i) = \frac{\partial}{\partial m_i} \frac{\Delta G_{ex}}{w_w RT} \tag{1.30}$$

Although the work carried out in this project has focused on the implementation of the Pitzer model for activity coefficients, it is also worth mentioning the UNIQUAC model (Abrams and Prausnitz, 1975) extended in various branches such as that by Sander *et al.* (1986a,b) and another by Thomsen (1997).

In modelling barium sulphate kinetics, most studies apply kinetic models that account for changes in reaction rates based on the thermodynamic transition state by extending the fundamental kinetic rate from the law of mass action. In most studies with simple systems and sufficient mixing, the experimental data fit well to the elementary second-order kinetics rate expected from an elementary reaction (Christy and Putnis, 1993; Nancollas and Reddy, 1974; Shen *et al.*, 2009). However, some studies, e.g., (Lu *et al.*, 2020), present experimental cases in which the reaction appears to follow a first-order rate, differing from what the law of mass action would suggest.

There are variations to how this thermodynamic transition state is accounted for across different studies, a common approach is to add a simple linear dependency on the saturation ratio Ω such as that implemented by Zhen-Wu *et al.* (2016):

$$\frac{dm_{BaSO_4}}{dt} = r_f(\Omega - 1) \tag{1.31}$$

where r_f is the forward reaction rate. This fairly simple approach shows good validity in cases where nucleation and surface deposition do not strongly affect the net rate of formation. Some studies have highlighted the significance of primary nucleation in the early phases of the reaction. For example, (Aoun *et al.*, 1999) presents a kinetic model evolving with the growth of the nucleated crystals by adding a kinetic dependency on the average crystal size. Li and Jun (2018) explored explicit modelling of the nucleation kinetics through determination of the pre-exponential factor in (1.13).

1.4.4 Summary

The modelling of scale formation in complex flows is a multifaceted challenge, and each of its fundamental roots presents an area of research where significant gaps are still being explored. Connecting the knowledge from these separate scientific branches to understand scale formation within an industrial context requires extensive cross-disciplinary studies. On this cross-disciplinary scale, computational fluid dynamics offers an essential asset in the toolset.

Whilst the fundamental governing physics of thermodynamics and fluid dynamics are well understood, the broad array of processes driven by chemical reactions such as nucleation and subsequent growth that occur both in bulk or on the surface makes the modelling complex. A range of parameters such as surface conditions, shear forces, concentration ratios and interaction with other chemical species add further complexity to the thermodynamics of the process.

A major concern for accurate scale modelling is fundamentally understanding the role of fluid dynamics. Multi-phase flow affects surface wetting and, thereby, the water-to-surface transport dynamics. Turbulence promotes the mixing of the reactants in the water phase and also affects the phase distribution in multi-phase flows. Surface-fluid interface conditions, such as shear forces and surface morphology, play an important role in the thermodynamics of nucleation and growth.

Finally, an accurate understanding of mixing processes is fundamental to the experimental study of chemical kinetics and thermodynamics. In such studies, correct accounting for the variability of the reaction rates introduced by the flow conditions would advance the accuracy and potentially reduce the frequency of conflicting observations between different studies.

1.5 Actions taken in the present work

The thermodynamic fundamentals of crystallization have been studied thoroughly over the last century. Although the conceptual process is well understood, the coupled dynamics of kinetic reaction rates and surface interaction are still not fully understood. This is primarily due to the complexity of the deposition mechanisms.

In many situations, significant effects on reactivity arise from hydrodynamic conditions related to the transport and mixing of brines. Understanding surface deposition requires cross-disciplinary studies accounting for a range of factors, including but not limited to surface morphology, boundary layer fluid dynamics, turbulence-kinetic interaction, and crystal morphology. Furthermore, reasonably accurate knowledge of in-situ concentration variations near the surface is necessary. Throughout this PhD project, I have sought to advance the current state-of-the-art by publishing scientific papers.

Three journal papers have been published at the time of submission of this thesis, and one manuscript has been drafted for submission. These contributions aim to bridge some of the gaps in accurately modelling scale formation processes identified by the author of this thesis in cooperation with the co-authors of the published papers.

1.5.1 Simulation of phase dispersion and droplet size distribution

The first journal paper titled “Surface wetting in multiphase pipe-flow” (Bentzon *et al.*, 2020), attached in Chapter 2, describes a standalone project on the modelling of surface wetting in multi-phase flow conditions similar to those observed in the wells used for hydrocarbon extraction in the north sea. The study attempts to numerically replicate the dispersion of an oil-water interface presented in experiments by Elseth (2001). The setup is illustrated in figure 1.6. Due to the low density ratio and consequently low Atwood and Richardson numbers, the stability of the oil-water interface is relatively low and high levels of dispersion occur at relatively low interfacial slip velocities. This makes interface tracking methods such as VOF computationally infeasible in the dispersed parts of the

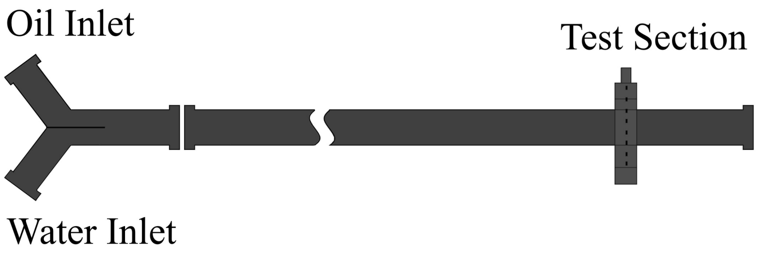

Figure 1.6: Illustration of physical domain for first journal paper.

flow (Kumara *et al.*, 2008). Lagrangian methods would be able to track droplets or clusters of droplets but would be challenged in modelling the transition between the stratified and dispersed regime. For these reasons, the Eulerian two-fluid model was tested as a potential candidate for resolving both the stratified and dispersed regimes and estimating droplet sizes.

The published paper tests state-of-the-art modelling techniques for this approach to simulate the phase distribution and thereby estimate the degree of water-wetting of the walls. The paper employed the S-gamma droplet size distribution model developed by Lo and Zhang (2009) to predict droplet size distribution and fluid-fluid interface area density.

The paper highlights the successful implementation of a dynamically evolving probability density function for the droplet size distribution. Such modelling allows accurate prediction of oil-water interface area for different industrial flow equipment designs. For example, such prediction ability may be used to optimize the design of such equipment to reduce fouling and ensure minimal wastewater pollution after oil-water separation on offshore platforms.

1.5.2 Simulation of mixing in a high-Reynolds number Taylor-Couette reactor

The second journal paper titled “The influence of turbulent transport in reactive processes: A combined numerical and experimental investigation in a Taylor-Couette reactor” (Anabaraonye *et al.*, 2021), attached as Chapter 3, focuses on turbulent mixing in single-phase flow in a liquid-phase reactor. The paper covers both the design and operation of a newly built reactor and simulations of experiments conducted with it, emphasizing the effects of the hydrodynamics within the reactor and, finally, suggestions for a novel parameter for quantification of turbulent mixing obtained from CFD simulations.

At the time of starting the focus on hydrodynamic-kinetic coupling, few good experiments were available for both validations of numerical implementation and subsequent analysis of the subject. A Taylor-Couette reactor was designed and built to promote such studies within crystallization.

A Taylor-Couette reactor is a continuously injected stirred reactor where fluid occupies the space between two concentric cylinders, of which one or both are rotating. Our design of such a reactor consists of a static outer steel casing with an inner rotating cylinder made of polytetrafluoroethylene (PTFE). The steel casing is replaceable so that different surfaces can be tested. The inner cylinder is also changeable to use different diameter

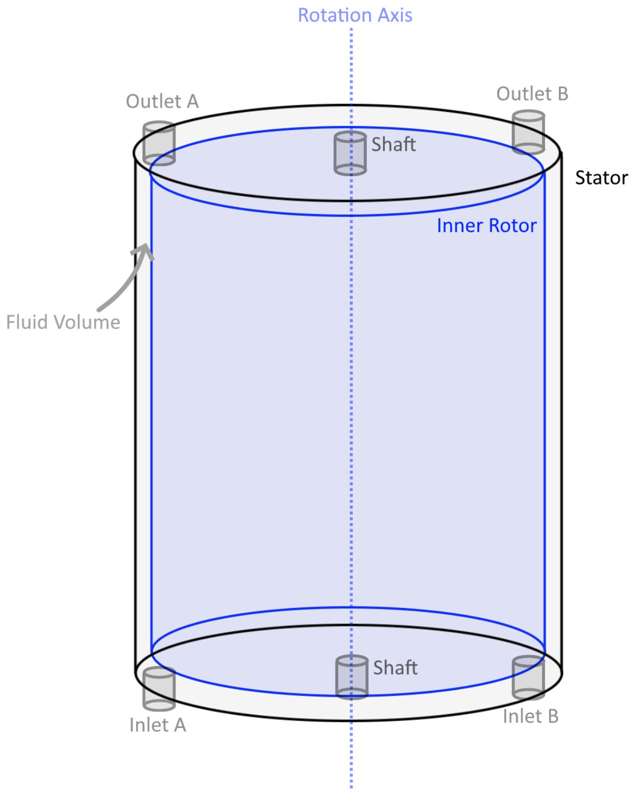

Figure 1.7: Schematic illustration of the Taylor-Couette reactor designed in this project.

rotors. The outer casing is encapsulated in a heat exchanger to control the temperature of the experiments. Two inlets are located at the bottom, allowing injection of different brines and two outlets are attached at the top and connected to an inductively coupled plasma optical emission spectroscopy device (ICP-OES) to analyze effluents in real-time. The reactor design is illustrated in figure 1.7

This reactor design was chosen to provide several advantages, namely:

1. The cell has easily modelled flow boundaries with laminar inlet velocities and no mixing prior to the cell. This makes a numerical model confined to simple and well-defined boundary conditions.
2. The residence time of the reactor, i.e., its volume divided by the flow rate, is decoupled from other flow properties such as Reynolds number and shear stresses and vice versa. This means that the residence time and, thereby, the total injected brine may be kept constant across a series of variation experiments such as differing Reynolds numbers.
3. Two independent parameters, namely the rotational rate and ratio of the rotor radius to the stator radius, allow advanced manipulation of the fluid dynamics within the reactor. This allows us to conduct experiments with, e.g., varied shear stress magnitude under constant Reynolds number.
4. The axis-symmetry of the reactor means that CFD can be modelled with a static mesh, drastically reducing computation time compared to reactors where mesh de-

formation is necessary.

5. Continuous monitoring of effluents. This gives well resolved non-intrusive time-series data to validate CFD against.
6. Easy assembly and disassembly allow for experiments with different surface materials. This means that different surface treatments and conditions can be tested. It has also been conceptualized to use a glass stator to experiment with brines causing fluorometric reactions upon mixing, such as those used in (Wheat and Posner, 2009). Such experiments will illustrate the mixing rate and, thereby, reaction through the fluorescence intensity.

This reactor has been used for the experimental results published in the paper included as Chapter 3 as well as in the manuscript attached as Chapter 5. In the former of those studies, we focused on quantifying the fluid dynamics inside the reactor at a fixed rotor radii of 80 mm yielding a rotor-stator radii ratio of $\eta = r_{rotor}/r_{stator} = 0.82$ operated at turbulent Reynolds numbers in the range of 1×10^4 to 4×10^4. Under these conditions, we conducted non-reactive mixing experiments in tandem with simulations, coherently indicating that the reactants were well mixed, with effluent concentration time-series not showing significant change within the range of Reynolds numbers tested.

In addition to illustrating typical fluid dynamics such as velocity and pressure fields and fluid forces exerted on the surfaces, we went into detail with quantification of the effects of turbulence on the reactor operation. We started this quantification by exploring the effect of turbulence on the Damköhler number, i.e., the ratio of reaction rate to the transport rate. Here we based the reaction rate and transport rates from the terms on the right hand side of the transport equation (1.16). By considering the added turbulent diffusivity as the source of change to the Damköhler number, we arrived at a derivation of a turbulent Peclét number as a candidate for accurately quantifying the expected enhancement of reactivity from turbulence when the Damköhler number is relatively high (meaning reactivity is largely limited by transport).

By comparing simulations of experiments at Reynolds numbers 2×10^4 and 4×10^4 we see a significant increase in the added diffusivity leading to a 29% increase in the turbulent Peclét number. In parallel, we conducted reactive experiments with barium sulphate precipitating from mixing barium chloride and sodium sulphate brines and saw a significant shift in chemical conversion. This finding illustrates the significance of turbulence even under considerably well-mixed conditions.

In summary, we conclude that even though a reactor is well mixed at macro-scale level, turbulence on a micro-scale level plays a significant role for the effective Damköhler number and hence reactivity. We illustrate that through turbulent mixing state quantification such as through the turbulent Peclét number justifies these observations based on data obtained in non-reactive simulations.

After submitting the paper mentioned above, we compared the output of simple reactive simulations to visual observation of deposition patterns on the stator of the Taylor-Couette cell. Apparent coherence between the expected zones of higher turbulent Peclét number and the deposition location was observed for a range of different Reynolds numbers and radii-ratios. An example of such visual comparison is coherence is shown in figure 1.8.

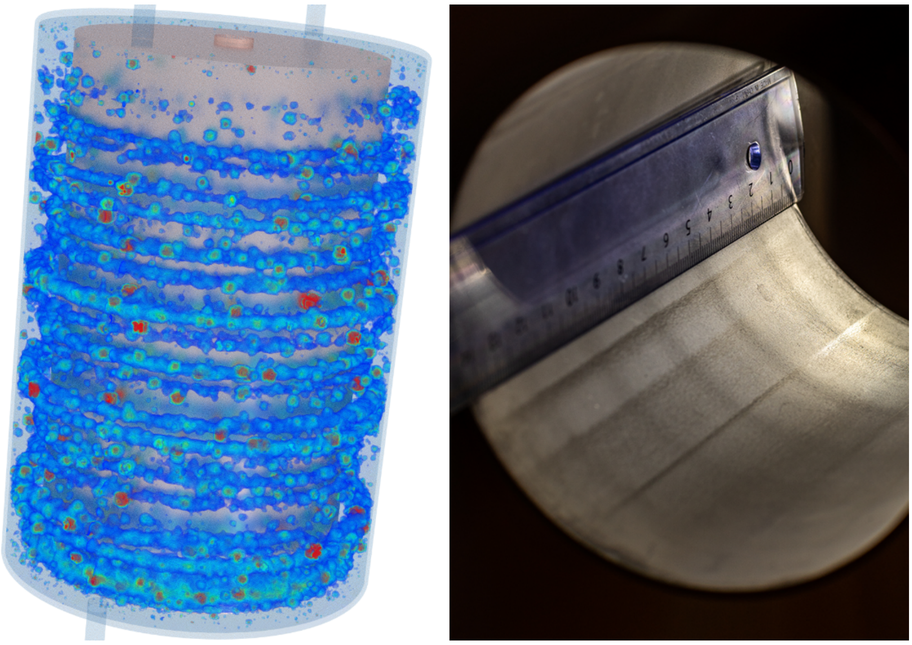

Figure 1.8: Left: Intensity of the simulated effect of micro-scale mixing on reactivity. Right: Observed surface showing barium sulphate deposition after experiment. Voxels: Micro-scale mixing intensity, starts at transparent at low mixing and goes to blue and then through green to red as intensity increases.

With the publication of that study, we have presented the audience with a structured framework for quantifying and comparing micro-scale mixing in terms of expected effects on reactivity. Hopefully, it will stand as an offset for further research in applying such frameworks to enhance the accuracy of scale modelling and prediction.

1.5.3 Phenomenological exploration of scale precipitation in pipe flow under different hydrodynamic and surface conditions

While the second paper predominantly focuses on turbulence and bulk mixing, a different range of studies has been conducted on a more phenomenological stage of surface deposition. The third journal paper titled “Scale attachment and detachment: The role of hydrodynamics and surface morphology” (Løge *et al.*, 2022), attached in Chapter 4, explores the differences observed between experiments using two different surface designs within both turbulent and laminar pipe flow.

The surface characteristics of industrial equipment are typically different from planar smooth walls. Surface roughness resulting from, e.g., the manufacturing of the equipment or from in-service corrosion is likely to impact subsequent scale. By designing one smooth and one threaded cell through which supersaturated brine flows at different rates, we explore how surface characteristics affect the way deposition occurs on the surface under both turbulent and laminar conditions.

In the paper, X-ray micro-computed tomography (CT) has been used to scan cells after different durations of growth. An in-house developed computational model then reconstructs the scans to evaluate and visualize scale deposition in the cell. Numerical reactive flow simulations are used to support these reconstructions in order to enhance the understanding of the experiments. From the reconstructed images and numerical simulations, we qualitatively discuss how crystals build up in the four cases of: Laminar smooth, laminar threaded, turbulent smooth, and turbulent threaded.

Between laminar and turbulent flow, we observe differences in the uniformity of growth. Under laminar flow conditions we observe solitaire crystals forming from a few nucleation sites. In contrast, under turbulent flow conditions we observe crystals growing more uniformly across the surface area. The threaded surfaces experience concentrated crystal formation on the flow facing tips of the threading, contrasting the smooth surface where crystal growth locations appear random. The detachment of formed crystals was more prevalent for the laminar flow cases where single crystals were torn off the surface. In the turbulent flow, detachment generally occurs on a “forest” of crystals as a whole.

From the observations supported by numerical experiments, we show that a high rate of reactant influx governs crystal growth in a turbulent flow due to near-surface eddies. Thus, activation energy barriers for initial nucleation on the surface are more easily overcome, consequently, for the turbulent flow crystal growth uniformly across the surface. In contrast, under the laminar flow, reactant transport to the surface is mainly limited to diffusion. Thus, only selected “good” seeding locations nucleate, and single, solitary crystals grow from those.

1.5.4 Advanced turbulence-kinetic modelling for use in crystallization kinetics

The two published papers on the hydrodynamic-kinetic interactions (Anabaraonye *et al.*, 2021; Løge *et al.*, 2022) highlighted significant high-level effects of the transport and mixing. In (Anabaraonye *et al.*, 2021), we investigated the added grid-level mixing from turbulence and the implicit effects on reactivity through the relative Damköhler number. However, we did not include implications of the implicitly assumed sub-grid-scale homogeneity of the reactants. Considering such implications in the numerical analysis frameworks for modelling and predicting scale would further enhance the ability to close the gap between the hydrodynamics and reactive modelling at lower-than-DNS resolution.

With a fourth paper drafted on the effects of variability of reactant concentration on reactivity, we delve into the topic of sub-grid-scale turbulence kinetics interaction. Using experiments in the aforementioned Taylor-Couette reactor as well as experiments in stirred batch reactors, we explore the ability of CFD models to capture the effects of inhomogeneity in the experiment to correctly account for this in the determination and tuning of fundamental reaction rate models. We employ LES and RANS modelling techniques at different grid sizes using different models to account for the filtered scales of the flow, concentrations and reaction rates.

References

D. S. Abrams, and J. M. Prausnitz (1975), "Statistical thermodynamics of liquid mixtures: A new expression for the excess Gibbs energy of partly or completely miscible systems," AIChE J. **21** (1), 116–128.

M. Aoun, E. Plasari, R. David, and J. Villermaux (1999), "A simultaneous determination of nucleation and growth rates from batch spontaneous precipitation," Chem. Eng. Sci. **54** (9), 1161–1180.

S. Arrhenius (1889), "Über die dissociationswärme und den einfluss der temperatur auf den dissociationsgrad der elektrolyte," Z. Phys. Chem. **4U** (1), 96–116.

I. Asimov (1965), *A Short History of Chemistry* (Anchor Books, New York).

G. K. Batchelor (1959), "Small-scale variation of convected quantities like temperature in turbulent fluid part 1. General discussion and the case of small conductivity," J. Fluid Mech. **5** (1), 113–133.

M. Bösenhofer, E.-M. Wartha, C. Jordan, and M. Harasek (2018), "The eddy dissipation concept—analysis of different fine structure treatments for classical combustion," Energies **11** (7), 1902.

N. Brauner (2001), "The prediction of dispersed flows boundaries in liquid-liquid and gas-liquid systems," Int. J. Multiph. Flow. **27** (5), 885–910.

A. G. Christy, and A. Putnis (1993), "The kinetics of barite dissolution and precipitation in water and sodium chloride brines at 44–85°C," Geochim. Cosmochim. Acta **57** (10), 2161–2168.

E. Curti, J. Xto, C. N. Borca, K. Henzler, T. Huthwelker, and N. I. Prasianakis (2019), "Modelling Ra-bearing baryte nucleation/precipitation kinetics at the pore scale: application to radioactive waste disposal," Eur. J. Mineral. **31** (2), 247–262.

P. Debye, and E. Hückel (1923), "Zur theorie der elektrolyte. I. Gefrierpunktserniedrigung und verwandte erscheinungen," Physikal. Zeitschr. **24**, 185–206.

A. Deshmukh, C. Boo, V. Karanikola, S. Lin, A. P. Straub, T. Tong, D. M. Warsinger, and M. Elimelech (2018), "Membrane distillation at the water-energy nexus: limits, opportunities, and challenges," Energy Environ. Sci. **11**, 1177–1196.

G. Elseth (2001), *An experimental study of oil / water flow in horizontal pipes*, Ph.D. thesis (Telemark University College).

H. Eyring (1935), "The activated complex in chemical reactions," J. Chem. Phys. **3** (2), 107–115.

C. Fischer, R. S. Arvidson, and A. Lüttge (2012), "How predictable are dissolution rates of crystalline material?" Geochim. Cosmochim. Acta **98**, 177–185.

M. Germano, U. Piomelli, P. Moin, and W. H. Cabot (1991), "A dynamic subgrid-scale eddy viscosity model," Phys. Fluids A **3** (7), 1760–1765.

S. Goldstein (1931), “On the stability of superposed streams of fluids of different densities,” Proc. R. Soc. A **132** (820), 524–548.

P. Grosfils, and J. F. Lutsko (2021), “Impact of surface roughness on crystal nucleation,” Crystals **11** (1), 1–20.

E. A. Guggenheim (1929), “The conceptions of electrical potential difference between two phases and the individual activities of ions,” J. Phys. Chem. **33** (6), 842–849.

C. M. Guldberg, and P. Waage (1879), “Ueber die chemische affinität. § 1. Einleitung,” J. Prakt. Chem. **19** (1), 69–114.

G. Gündüz (1982), “Colemanite-baryte frit and polymer impregnated concrete as shielding materials,” Nucl. Eng. Des. **72** (3), 439–447.

D. J. Gunn (1980), “Effect of surface roughness on the nucleation and growth of calcium sulphate on metal surfaces,” J. Cryst. Growth **50** (2), 533–537.

N. I. Gurakov, I. A. Zubrilin, V. Y. Abrashkin, M. H. Morales, Ez, D. V. Yakushkin, V. V. Yastrebov, O. V. Kolomzarov, and D. V. Idrisov (2020), “Validation of the vof method for liquid spray process simulation from a pressure-swirl atomizer,” in *AIP Conference Proceedings*, Vol. 2304 (American Institute of Physics Inc.) p. 0033854.

C. K. Harris, D. Roekaerts, F. J. J. Rosendal, F. G. J. Buitendijk, P. Daskopoulos, A. J. N. Vreenegoor, and H. Wang (1996), “Computational fluid dynamics for chemical reactor engineering,” Chem. Eng. Sci. **51** (10), 1569–1594.

J. Hinze (1955), “Fundamentals of the hydrodynamic mechanism of splitting in dispersion processes,” AIChE J. **1** (3), 289–295.

C. W. Hirt, and B. D. Nichols (1981), “Volume of fluid (VOF) method for the dynamics of free boundaries,” J. Comput. Phys. **39** (1), 201–225.

L. K. Hjertager, B. H. Hjertager, and T. Solberg (2001), “CFD modeling of fast chemical reactions in turbulent liquid flows,” in *European Symposium on Computer Aided Process Engineering - 11*, Computer Aided Chemical Engineering, Vol. 9, edited by R. Gani, and S. B. Jørgensen (Elsevier) pp. 159–164.

K. Jain, A. Gidwani, S. Kumar, and J. V. Cole (2019), “CFD study of carbon corrosion in PEM fuel cells,” ECS Trans **16** (2), 1323–1333.

S. N. Kazi, G. G. Duffy, and X. D. Chen (2010), “Mineral scale formation and mitigation on metals and a polymeric heat exchanger surface,” Appl. Therm. Eng. **30** (14-15), 2236–2242.

D. H. Kelley, and N. T. Ouellette (2011), “Separating stretching from folding in fluid mixing,” Nature Physics **7** (6), 477–480.

S. Keysar, R. Semiat, D. Hasson, and J. Yahalom (1994), “Effect of surface roughness on the morphology of calcite crystallizing on mild steel,” J. Colloid Interface Sci. **162** (2), 311–319.

R. Kresse, U. Baudis, P. Jäger, H. H. Riechers, H. Wagner, J. Winkler, and H. U. Wolf (2007), “Barium and barium compounds,” in *Ullmann’s Encyclopedia of Industrial Chemistry*, Chap. Barium Sulfate (John Wiley & Sons, Ltd) pp. 626–629.

W. A. S. Kumara, G. Elseth, B. M. Halvorsen, and M. C. Melaaen (2008), "Computational study of stratified two phase oil/water flow in horizontal pipes," in *HEFAT 2008* (Citeseer).

W. A. S. Kumara, B. M. Halvorsen, and M. C. Melaaen (2009), "Pressure drop, flow pattern and local water volume fraction measurements of oil–water flow in pipes," Meas. Sci. Technol. **20** (11), 114004.

B. E. Launder, and B. I. Sharma (1974), "Application of the energy-dissipation model or turbulence to the calculation of flow near a spinning disc," Lett. Heat Mass Transf. **1** (2), 131–137.

M. T. Lewandowski, and I. S. Ertesvåg (2018), "Analysis of the eddy dissipation concept formulation for mild combustion modelling," Fuel **224**, 687–700.

G. N. Lewis (1907), "Outlines of a new system of thermodynamic chemistry," Proc. Am. Acad. Arts Sci **43** (7), 259–293.

G. N. Lewis, and M. Randall (1961), *Thermodynamics, Revised by Kenneth S. Pitzer and Leo Brewer*, 2nd ed. (McGraw-Hill, New York).

J. Li, M. Tang, Z. Ye, L. Chen, and Y. Zhou (2017), "Scale formation and control in oil and gas fields: A review," J. Disp. Sci. Tech. **38** (5), 661–670.

Q. Li, and Y.-S. Jun (2018), "The apparent activation energy and pre-exponential kinetic factor for heterogeneous calcium carbonate nucleation on quartz," Commun. Chem. **1**, 56.

X. Li, J. Peoples, P. Yao, and X. Ruan (2021), "Ultrawhite $BaSO_4$ paints and films for remarkable daytime subambient radiative cooling," ACS Appl. Mater. Interfaces **13** (18), 21733–21739.

H. Liu, J. Shi, H. Qu, and D. Ding (2019), "An investigation on physical, mechanical, leaching and radiation shielding behaviors of barite concrete containing recycled cathode ray tube funnel glass aggregate," Constr. Build. Mater **201**, 818–827.

S. Lo, and D. Zhang (2009), "Modelling of break-up and coalescence in bubbly two-phase flows," Int. Comm. Heat Mass Transfer **1** (1), 23–38.

E. Loth (2000), "Numerical approaches for motion of dispersed particles, droplets and bubbles," Prog. Energy Combust. Sci. **26** (3), 161–223.

A. Y.-T. Lu, K. Harouaka, S. Paudyal, S. Ko, C. Dai, S. Gao, G. Deng, Y. Zhao, X. Wang, S. Mateen, A. T. Kan, and M. Tomson (2020), "Kinetics of barium sulfate deposition and crystallization process in the flowing tube," Ind. Eng. Chem. Res. **59** (16), 7299–7309.

D. A. Lysenko, I. S. Ertesvåg, and K. E. Rian (2014), "Numerical simulations of the Sandia flame D using the eddy dissipation concept," Flow Turbul. Combust. **93** (4), 665–687.

B. Magnussen (1981), "On the structure of turbulence and a generalized eddy dissipation concept for chemical reaction in turbulent flow," in *19th Aerospace Sciences Meeting*.

C. Meneveau, and J. Katz (2000), "Scale-invariance and turbulence models for large-eddy simulation," Ann. Rev. Fluid Mech. **32** (1), 1–32.

E. E. Meshkov (1969), “Instability of the interface of two gases accelerated by a shock wave,” Fluid Dyn. **4**, 141–104.

H. Mikkelsen, and J. H. Walther (2020), “Effect of roughness in full-scale validation of a CFD model of self-propelled ships,” Appl. Ocean Res. **99**, 102162.

Y. Minamoto, K. Aoki, M. Tanahashi, and N. Swaminathan (2015), “DNS of swirling hydrogen–air premixed flames,” Int. J. Hydrog. Energy **40** (39), 13604–13620.

H. Müller-Steinhagen (2011), “Heat transfer fouling: 50 years after the Kern and Seaton model,” Heat Trans. Engng. **32** (1), 1–13.

J. W. Mullin (2001), *Crystallization*, 4th ed. (Butterworth-Heinemann, Oxford).

G. H. Nancollas, and M. M. Reddy (1974), “The kinetics of crystallization of scale-forming minerals,” SPE J. **14** (02), 117–126.

Neeraj, and S. Yadav (2020), “Carbon storage by mineral carbonation and industrial applications of CO_2,” Mat. Sci. Energy Technol. **3**, 494–500.

F. Nicoud, and F. Ducros (1999), “Subgrid-scale stress modelling based on the square of the velocity gradient tensor,” Flow, Turbul. Combust. **62**, 183–200.

J. M. Ottino (1989), *The kinematics of mixing : stretching, chaos, and transport* (Cambridge Univ. Press).

B. Panjawani, I. S. Ertesvåg, A. Gruber, and K. E. Rian (2010), “Turbulence combustion closure model based on the eddy dissipation concept for large eddy simulation,” WIT Trans. Eng. Sci **69**, 27–38.

B. Peters (2017), “Chapter 2 - Chemical equilibrium,” in *Reaction Rate Theory and Rare Events Simulations* (Elsevier, Amsterdam) pp. 19–37.

K. S. Pitzer (1973), “Thermodynamics of electrolytes. I. Theoretical basis and general equations,” J. Phys. Chem. **77** (2), 268–277.

K. S. Pitzer (1977), “Electrolyte theory - improvements since Debye and Hueckel,” Acc. Chem. Res. **10** (10), 371–377.

K. S. Pitzer (1986), “Theoretical considerations of solubility with emphasis on mixed aqueous electrolytes,” Pure Appl. Chem **58** (12), 1599–1610.

R. Pohorecki, and J. Baldyga (1983), “New model of micromixing in chemical reactors. 1. General development and application to a tubular reactor,” Ind. Eng. Chem. **22** (4), 392–397.

S. B. Pope (1985), “PDF methods for turbulent reactive flows,” Prog. Energy Combust. Sci. **11** (2), 119–192.

A. Prosperetti, and G. Tryggvason (2007), *Computational methods for multiphase flow* (Cambridge University Press).

H. P. Rani, T. Divya, R. R. Sahaya, V. Kain, and D. K. Barua (2014), “CFD study of flow accelerated corrosion in 3D elbows,” Ann. Nucl. Energy **69**, 344–351.

Rayleigh (1882), “Investigation of the character of the equilibrium of an incompressible heavy fluid of variable density,” Proc. Lond. Math. Soc **s1-14** (1), 170–177.

R. D. Richtmyer (1960), “Taylor instability in shock acceleration of compressible fluids,” Commun. Pure Appl. Math. **13** (2), 297–319.

M. Rizzotto, F. Florit, R. Rota, and V. Busini (2019), “A CFD hybrid approach to simulate liquid-phase chemical reactors,” Chem. Eng. J. **377**, 120365, iSCRE 25 Special Issue: Bridging Science and Technology.

A. Ruiz-García, N. Melián-Martel, and I. Nuez (2017), “Short review on predicting fouling in RO desalination,” Membranes **7** (4), 62.

B. Sander, A. Fredenslund, and P. Rasmussen (1986a), “Calculation of vapour-liquid equilibria in mixed solvent/salt systems using an extended UNIQUAC equation,” Chem. Eng. Sci. **41** (5), 1171–1183.

B. Sander, P. Rasmussen, and A. Fredenslund (1986b), “Calculation of solid-liquid equilibria in aqueous solutions of nitrate salts using an extended UNIQUAC equation,” Chem. Eng. Sci. **41** (5), 1197–1202.

K. M. Sassi, and I. M. Mujtaba (2011), “Optimal design and operation of reverse osmosis desalination process with membrane fouling,” Chem. Engng. J. **171** (2), 582–593.

J. W. P. Schmelzer, J. Schmelzer, and I. S. Gutzow (2000), “Reconciling Gibbs and van der Waals: A new approach to nucleation theory,” J. Chem. Phys. **112** (8), 3820–3831.

R. Sharifian, R. M. Wagterveld, I. A. Digdaya, C. Xiang, and D. A. Vermaas (2021), “Electrochemical carbon dioxide capture to close the carbon cycle,” Energy Environ. Sci. **14**, 781–814.

D. Shen, G. Fu, H. A. Al-Saiari, A. T. Kan, and M. B. Tomson (2009), “Barite dissolution/precipitation kinetics in porous media and in the presence and absence of a common scale inhibitor,” SPE J. **14** (03), 462–471.

J. S. Shirolkar, C. F. Coimbra, and M. Q. McQuay (1996), “Fundamental aspects of modeling turbulent particle dispersion in dilute flows,” Prog. Energy Combust. Sci. **22** (4), 363–399.

K. B. Southerland, R. D. Frederiksen, W. J. A. Dahm, and D. R. Dowling (1994), “Comparisons of mixing in chaotic and turbulent flows,” Chaos Solit. Fractals **4** (6), 1057–1089, Special Issue: Chaos Applied to Fluid Mixing.

P. Spalart, and S. Allmaras (1992), “A one-equation turbulence model for aerodynamic flows,” in *30th Aerospace Sciences Meeting and Exhibit* (AIAA).

I. Sreedhar, S. Khaitan, R. Gupta, B. M. Reddy, and A. Venugopal (2018), “An odyssey of process and engineering trends in forward osmosis,” Environ. Sci.: Water Res. Technol. **4**, 129–168.

P. A. Pogge von Strandmann, K. W. Burton, S. O. Snæbjörnsdóttir, B. Sigfússon, E. S. Aradóttir, I. Gunnarsson, H. A. Alfredsson, K. G. Mesfin, E. H. Oelkers, and S. R. Gislason (2019), “Rapid CO_2 mineralisation into calcite at the CarbFix storage site quantified using calcium isotopes,” Nature Commun. **10** (1), 1983.

R. F. Strickland-Constable (1968), *Kinetics and Mechanism of Crystallization* (Academic Press).

G. I. Taylor (1931), "Effect of variation in density on the stability of superposed streams of fluid," Proc. R. Soc. A **132** (820), 499–523.

G. I. Taylor (1950), "The instability of liquid surfaces when accelerated in a direction perpendicuar to their planes," Proc. R. Soc. Lond. **201**, 192–196.

K. Thomsen (1997), *Aqueous Electrolytes Model Parameters and Process Simulation*, Ph.D. thesis (Technical University of Denmark).

M. Volmer (1939), *Kinetics of Phase Formation: (Kinetik Der Phasenbildung)*, Chemische Reaktion (T. Steinkopff).

X. Wei, H. Takahashi, S. Sato, and M. Nomura (2001), "Continuous emulsion polymerization of styrene in a single Couette–Taylor vortex flow reactor," J. Appl. Polym. Sci. **80** (11), 1931–1942.

P. M. Wheat, and J. D. Posner (2009), "Quantifying mixing using equilibrium reactions," Phys. Fluids **21** (3), 037101.

D. C. Wilcox (1988), "Re-assessment of the scale-determining equation for advanced turbulence models," AIAA J. **26** (11), 1299–1310.

C.-Z. Xu, J.-J. Wang, X.-P. Gu, and L.-F. Feng (2017), "CFD modeling of styrene polymerization in a CSTR," Chem. Eng. Res. Des. **125**, 46–56.

C. Zhang, J. Lin, H. Sun, and X. Shi (2015a), "Influence of characteristics and roughness of nucleation in conical pits on surface heterogeneous nucleation," Procedia Engng. **121**, 1281–1288.

R. Zhang, T. Cong, W. Tian, S. Qiu, and G. Su (2015b), "CFD analysis on subcooled boiling phenomena in PWR coolant channel," Prog. Nucl. Energy **81**, 254–263.

Q. Zhao, Y. Liu, C. Wang, S. Wang, and H. Müller-Steinhagen (2005), "Effect of surface free energy on the adhesion of biofouling and crystalline fouling," Chem. Eng. Sci. **60** (17), 4858–4865.

B. Y. Zhen-Wu, K. Dideriksen, J. Olsson, P. J. Raahauge, S. L. S. Stipp, and E. H. Oelkers (2016), "Experimental determination of barite dissolution and precipitation rates as a function of temperature and aqueous fluid composition," Geochim. Cosmochim. Acta **194**, 193—210

2 Paper 1: Surface wetting in multiphase pipe-flow

Multiphase Science and Technology, 32(2):137–154 (2020)

SURFACE WETTING IN MULTIPHASE PIPE-FLOW

Jakob R. Bentzon,[1,*] Attila Vural,[1] Karen L. Feilberg,[2] & Jens H. Walther[3,4]

[1]*Department of Mechanical Engineering, Technical University of Denmark, Kgs. Lyngby, Denmark*

[2]*The Danish Hydrocarbon Research and Technology Centre, Technical University of Denmark, Kgs. Lyngby, Denmark*

[3]*Department of Mechanical Engineering, Technical University of Denmark, Kgs. Lyngby, Denmark*

[4]*Computational Science and Engineering Laboratory, ETH, Zürich, CH-8092, Switzerland*

*Address all correspondence to: Jakob R. Bentzon, Department of Mechanical Engineering, Technical University of Denmark, Kgs. Lyngby, 2800, Denmark, E-mail: jroben@mek.dtu.dk

Original Manuscript Submitted: 7/15/2019; Final Draft Received: 2/17/2020

The present study examines the quantity of surface wetting in a two-phase oil and water pipe flow. The study is performed by employing an Eulerian-Eulerian computational fluid dynamics model using the S-gamma droplet size distribution model within STAR–CCM+. In the North Sea, production of oil and gas, water-phase surface processes such as scale and corrosion account for 40–50% of operating expenses. The objective of the study is to investigate best practices for the prediction of phase distribution aimed at evaluating the degree of the wall in contact with the water phase (water-wetting). The model is validated by performing detailed numerical simulations corresponding to the experimental studies by Kumara, Halvorsen, and Melaaen (Meas. Sci. Technol., vol. ***20****, p. 114004, 2009). The comparison yields good agreement with the observed measurements with slight deviations in the predicted dispersion rate but accurate prediction of the liquid holdup. Comparison of droplet sizes to those observed in experiments by Elseth (PhD, Telemark University College, 2001) indicates that tuning of the S-gamma model is necessary to provide accurate droplet size predictions. The surface wetting is then evaluated with its interdependence with liquid holdup and dispersion rate. Increase in the dispersion with a decrease in the Richardson number is observed in agreement with stability analysis of the Kelvin-Helmholtz instability.*

KEY WORDS: *multiphase, CFD, Euler-Euler, water-wetting, liquid holdup, STAR–CCM+, S-gamma, droplet size, oil, surface wetting*

1. INTRODUCTION

Flow assurance is a major challenge in the oil and gas industries and amounts to 40–50% of the total operating expenses in many wells due to costly mechanical and chemical intervention. The presence of hard and soft scales (e.g., $CaCO_3$, $BaSO_4$, $FeCO_3$, FeS) might lead to loss of

0276–1459/20/$35.00 © 2020 by Begell House, Inc. www.begellhouse.com

production due to scale build up and enhanced corrosion rates due to galvanic effects and fouling of equipment, which can lower the production rates and ultimately render oil-wells unrecoverable. Consequently, it is of major importance to understand the mechanisms and the rates of corrosion and scale deposition under hydrodynamic conditions and realistic flow in the production wells.

Understanding the proportion of wall in contact with the water phase, a property known as water-wetting is crucial for the development and analysis of mitigation measures. The flow regime varies from stratified to fully dispersed throughout the well; therefore, a fully qualified model should capture the physics of both flow regimes. The application of the volume-of-fluid (VOF) approach to model dispersion of the phases requires interface resolution of the droplets in the flow (Hirt and Nichols, 1981). The average droplet sizes in fully dispersed flows are estimated to be on the order of 1 mm based on the maximum diameter observed in experiments by Elseth (2001). This makes the use of the VOF model infeasible for the dispersed flow regime. In contrast, the Eulerian-Eulerian two-equation approach allows for subgrid, droplet-dispersion modeling through empirical closure laws and is used throughout this work. This method has been used successfully for a number of liquid-liquid and liquid-gas flows (Prosperetti and Tryggvason, 2007).

Attempts to simulate the study by Kumara et al. (2008) using the VOF approach shows good prediction of the velocity profiles and pressures but does not describe the dispersion of the phases. A Eulerian-Eulerian approach using droplet sizes determined from the correlations by Brauner (2001) has been studied by Pouraria et al. (2016) to replicate the results from Elseth (2001) and has achieved fairly good agreement. The accuracy of the Eulerian-Eulerian approach depends on the models for determining the transfer of momentum between the phases. Typically, this included drag, lift, surface tension, virtual mass, and surface contact forces. These models depend on an estimate of the droplet size. Modeling attempts with a constant droplet size have proven to have limited success in predicting dispersion adequately. Consequently, the present study employs the S-gamma droplet size distribution model described by Lo and Zhang (2009).

From the aforementioned work, it is clear that the Eulerian-Eulerian model has good potential as a tool for studies of two-phase flow in oil wells. Thus, a thorough study to validate the model and its parameters is essential for further research. The objective of the present study is to validate and optimize the numerical procedure for two-phase oil and water pipe flows against the experiments from Elseth (2001) and Kumara et al. (2009). The resulting distribution of the phases is compared to gamma densitometry measurements of cross-sectional phase distributions by Kumara et al. (2009). Similarly, the droplet sizes obtained by the S-gamma droplet size distribution model is compared to droplet sizes obtained by visual inspection in the study by Elseth (2001).

To analyze surface wetting, the consequence of liquid holdup (i.e., flow properties causing one fluid to move slower than the other and thereby increasing its share of cross-sectional area in the pipe) is analyzed. Additionally, the rate of dispersion affects how much of each phase is in contact with the wall. Using a validated model, these two phenomena can be analyzed for different flow properties.

2. METHODOLOGY

A numerical computational fluid dynamics (CFD) model is set up in the STAR–CCM+ version 13.04 to investigate the best modeling settings for replicating the experimental study by Elseth (2001) and Kumara et al. (2009). The test rig illustrated in Fig. 1 consists of a pipe section with

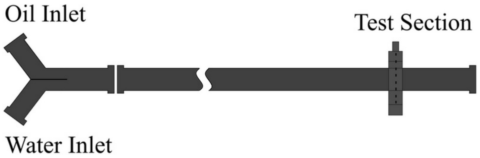

FIG. 1: Illustration of the experimental model described in Elseth (2001)

diameter $D = 0.0563$ m and length 12 m (213 diameters), followed by a test section where time-averaged gamma densitometry measurements were taken across a set of cords in the horizontal direction. The pipe section is preceded by a Y-junction from which oil and water flows into each inlet. The flow is controlled by the flow rate of each phase k ($k \in w, o$, where o denotes oil and w denotes water) and is reported in terms of mean velocity $U = (\dot{V}_w + \dot{V}_o)/(D^2\pi/4)$ and water-cut $\psi = \dot{V}_w/(\dot{V}_w + \dot{V}_o)$, where $\dot{V}_w$ and $\dot{V}_o$ are the volumetric flow rates of water and oil. The CFD model assumes symmetry in the plane spanned by the axial direction of the pipe and the gravitational direction.

2.1 Governing Equations

The numerical simulations are based on the Eulerian-Eulerian two-fluid approach. This treats both phases as a continuous phase, each with its own velocity field $\mathbf{u}_k$ but with a shared pressure field p (Ishii and Hibiki, 2006). The fluids are considered isothermal, immiscible, and incompressible. Hence, only mass and momentum conservation is considered. Both equations are averaged with a Reynolds decomposition to obtain a solution for the mean flow. This gives a set of volume-fraction-Averaged Reynolds averaged Navier-Stokes (RANS) equations for each of the two phases

$$\frac{\partial \alpha_k}{\partial t} + \nabla \cdot (\alpha_k \mathbf{u}_k) = 0 \tag{1}$$

$$\begin{aligned}\frac{\partial \alpha_k \rho_k \mathbf{u}_k}{\partial t} + \nabla \cdot (\rho_k \alpha_k \mathbf{u}_k \mathbf{u}_k) = -\alpha_k \nabla p + \alpha_k \rho_k \mathbf{g} \\ + \nabla \cdot \left\{\alpha_k \mu_{k,\text{eff}} \left[\nabla \mathbf{u}_k + (\nabla \mathbf{u}_k)^T\right]\right\} + \mathbf{M}_k\end{aligned} \tag{2}$$

where ρ_k and α_k are the density and volume fraction of the kth phase, **g** is the gravitational vector set to $\mathbf{g} = (-9.82 \sin \beta, -9.82 \cos \beta, 0)$ m/s^2, where β is the inclination angle of the pipe. $\mu_{k,\text{eff}} = \mu_k + \mu_{k,t}$ is the effective dynamic viscosity composed of the dynamic viscosity of the fluid (μ_k) and the turbulent viscosity ($\mu_{k,t}$) from the RANS decomposition, cf. Ishii and Hibiki (2006). A realizable k-ϵ model is used to determine the turbulent viscosity (Shih et al., 1995). All model parameters are left as per STAR–CCM+ defaults. The term $\mathbf{M}_k$ corresponds to the exchange of momentum between the two phases. The interfacial momentum transfer forces are subdivided into drag ($\mathbf{M}_{D,k}$), lift ($\mathbf{M}_{L,k}$), turbulent dispersion ($\mathbf{M}_{T,k}$), virtual mass ($\mathbf{M}_{V,k}$), and surface tension ($\mathbf{M}_{S,k}$):

$$\mathbf{M}_k = \mathbf{M}_{D,k} + \mathbf{M}_{L,k} + \mathbf{M}_{T,k} + \mathbf{M}_{V,k} + \mathbf{M}_{S,k} \tag{3}$$

where each of the interfacial forces are modeled using empirical closure laws.

2.2 Interfacial Forces

The interfacial drag, lift, turbulence dispersion, and virtual mass forces (generically denoted $M_{F,k}$) are modeled in three different regimes based on the volume fraction of water α_w. The two primary regimes are namely, the $D_{w/o}$ (dispersed water-in-oil) for $\alpha_w < 0.3$, the $D_{o/w}$ (dispersed oil-in-water) for $\alpha_w > 0.7$, cf. Cerne et al. (2001). In the intermediate range, a volume fraction averaged force is used. Between the two dispersed regions and the intermediate region, a blending zone of width 0.1 volume fraction is used.

$$\mathbf{M}_{F,k} = \begin{cases} \mathbf{F}_{F,w/o} & \alpha_w < 0.3 \\ \mathbf{F}_{F,o/w} & \alpha_w > 0.7 \\ f_w \mathbf{F}_{F,o/w} + f_o \mathbf{F}_{F,w/o} & \alpha_w \in [0.3, 0.7] \end{cases} \tag{4}$$

where the blending function f_k is given by

$$f_k = \begin{cases} \frac{0.4}{0.1}(\alpha_k - 0.3) & \alpha_k \in [0.3, 0.4] \\ \alpha_k & \alpha_k \in [0.4, 0.6] \\ 0.6 + \frac{0.4}{0.1}(\alpha_k - 0.6) & \alpha_k \in [0.6, 0.7] \end{cases} \tag{5}$$

The drag force $\mathbf{F}_{D,d/c}$ of a dispersed droplet of phase d in the continuous phase c is computed as follows:

$$\mathbf{F}_{D,d/c} = \frac{1}{2}\rho_p C_D |\mathbf{u}_d - \mathbf{u}_c|(\mathbf{u}_d - \mathbf{u}_c)\frac{A_{CD}}{4} \tag{6}$$

where A_{CD} is the mean interfacial area obtained from the droplet size distribution described in Section 2.3.

The drag coefficient in the $D_{w/o}$ and $D_{o/w}$ regimes are computed using the Schiller-Naumann model (Schiller and Naumann, 1933):

$$C_D = \begin{cases} \frac{24(1 + 0.15\mathrm{Re}_D^{0.687})}{\mathrm{Re}_D} & \mathrm{Re}_D \leq 1000 \\ 0.44 & \mathrm{Re}_D > 1000 \end{cases} \tag{7}$$

where the Reynolds number of the droplets (Re_D) is defined as:

$$\mathrm{Re}_D = \frac{\rho_c |\mathbf{u}_d - \mathbf{u}_c| d_{32}}{\mu_c} \tag{8}$$

where d refers to the dispersed phase (water for $D_{w/o}$ and oil for $D_{o/w}$) and c the continuous phase, d_{32} is the Sauter mean diameter of the droplets described in Schümann et al. (2015) and Lo and Zhang (2009).

As a dispersed droplet moves relative to a shear flow, it will experience a lift force perpendicular to the relative velocity proportional to the curl of the continuous phase velocity (Auton et al., 1988).

$$\mathbf{F}_{L,d/c} = -C_L \rho_c \alpha_d (\mathbf{u}_d - \mathbf{u}_c) \times (\nabla \times \mathbf{u}_c) \tag{9}$$

where the lift force coefficient C_L is set to a constant of 0.25, cf. Lance and Bataille (1991).

As a dispersed droplet accelerates relative to the continuous phase, the acceleration of a part of the continuous phase requires modeling of the added mass (Auton et al., 1988)

$$\mathbf{F}_{V,d/c} = C_{VM} \rho_c \alpha_d \mathbf{a}_{\mathrm{rel}} \tag{10}$$

where C_{VM} is the coefficient of virtual mass derived from inviscid flow theory to 0.5 for a sphere (Lamb, 1932) and $\mathbf{a}_{\text{rel}}$ is the relative acceleration of the phases

$$\mathbf{a}_{\text{rel}} = \frac{D\mathbf{u}_d}{Dt} - \frac{D\mathbf{u}_c}{Dt} \tag{11}$$

When applying the Reynolds averaging to the drag term, the nonlinear term gives rise to an extra turbulent dispersion term. This can be modeled as a dispersion drag coefficient C_{TD} on a turbulent dispersion velocity $\mathbf{u}_{TD}$.

$$\mathbf{M}_T = C_{TD}\mathbf{u}_{TD} \tag{12}$$

The turbulent dispersion velocity has its origin in the phase and Reynolds averaging and is approximated through the Boussinesq closure to

$$\mathbf{u}_{TD} \approx -\frac{\mu_{c,t}}{\rho_c \sigma_\alpha}\left(\frac{\nabla\alpha_c}{\alpha_c} - \frac{\nabla\alpha_d}{\alpha_d}\right) \tag{13}$$

where α_c, α_d are the Reynolds-averaged volume fractions of the continuous and dispersed phase, σ_α is the a coefficient describing the ratio of turbulent dispersion of volume fraction to that of momentum and is set to unity in this work. The turbulent dynamic viscosity is obtained from the k-ϵ model.

The turbulent dispersion drag coefficient, C_{TD}, is defined from a Stokesian drag coefficient and linearized with the relative velocity of the two averaged phases

$$C_{TD} = \frac{A_{CD}}{8}\rho_c C_D |\mathbf{u}_c - \mathbf{u}_d| \tag{14}$$

The droplet drag coefficient C_D is modeled using a Schiller-Naumann drag coefficient described by Eq. (7). The determination of which phase is continuous and dispersed is handled similarly to the drag force by Eq. (4).

Surface tension forces arises directly in the interfaces between the fluids. The Eulerian-Eulerian two-fluid model does not explicitly track the interface between the phases. To account for surface tension in the physical interface on larger fluid structures, the continuum surface tension model proposed by Brackbill et al. (1992) and described for a Eulerian-Eulerian two-fluid by Strubelj et al. (2009) is used. The numerical procedure is to reconstruct the surface normal based on one (primary, e.g., water) of the phases $\mathbf{n}_p$ and curvature κ_p

$$\mathbf{n}_p = \frac{\nabla\alpha_p}{|\nabla\alpha_p|} \tag{15}$$

$$\kappa_p = -\nabla \cdot \mathbf{n}_p \tag{16}$$

On the basis of the curvature, the surface tension force at the interface becomes

$$\mathbf{F}_S = \sigma\kappa_p\nabla\alpha_p \tag{17}$$

where σ is the surface tension in units force per length. The force is split between the two phases by dividing the force in the momentum equations relative to the local volume fraction

$$\mathbf{F}_{S,k} = \alpha_k\mathbf{F}_S \tag{18}$$

To simulate the interaction of the interface at the wall, the wall wetting contact angle θ_w is implemented by defining the interface normal vector of the first computational cell as a transformation of the unit normal vector of the wall $\mathbf{n}_w$ and tangential vector $\mathbf{t}_w$

$$\mathbf{n}_{p,\text{wall}} = \mathbf{n}_w \cos\theta_w + \mathbf{t}_w \sin\theta_w \tag{19}$$

With limited fluid properties available for the given mixture of water and oil, the wetting angle θ_w is set to 41 deg based on measurements of deacidified deasphaltened crude oil on stainless steel surfaces in a pure water solution by dos Santos et al. (2006).

In order to accurately determine the volume fraction gradients at interfaces, an interface compressing scheme was suggested by Strubelj et al. (2009). The interface sharpening method technique described by Coste (2013) has been used to produce a sharp interface marker function from comparison of cell surface volume fractions. This marker function is used to adaptively shift between the interface compressing high resolution interface capturing (HRIC) scheme described by Muzaferija and Peric (1997) and the total variation diminishing (TVD) scheme to avoid artificially sharpening interfaces in naturally dispersed regions.

2.3 Droplet Size

A key to modeling the interfacial forces is the correct estimation of droplet sizes and area density. For this purpose, the present study employs the S-gamma statistical droplet size distribution model developed by Lo and Zhang (2009). The S-gamma model describes the particles through three moments S_γ, where $\gamma \in 0, 2, 3$. Numerically, the model solves for the second moment, S_2, which describes the interfacial area density, and optionally it can additionally solve for the zeroth moment, S_0, describing the particle number density. The third moment, S_3, describes the volume density of the droplets and is thus directly correlated to the volume fraction of the dispersed phase

$$S_{3,k} = \frac{6}{\pi}\alpha_k \tag{20}$$

In this study, only the second moment is used and modeled for both phases. This is computationally simpler but limited to model the Sauter mean diameter, d_{32}, but does not yield the variance of the droplet size distribution. The second moment is formulated as the integral over the droplet size distribution of the square of the diameter and hence represents the droplet mean interfacial area (A_{CD}) divided by π

$$S_2 = \int d_p^2 n(d_p) d(d_p) = \frac{A_{CD}}{\pi} \tag{21}$$

By assuming spherical droplets, the Sauter mean diameter can be calculated as follows:

$$d_{32,k} = \frac{S_{3,k}}{S_{2,k}} \tag{22}$$

The S_γ moments are modeled as convective scalars tracked with a scalar transport equation

$$\frac{\partial S_{\gamma,k}}{\partial t} + \nabla \cdot (S_{\gamma,k}\mathbf{u}_k) = s_{br,k} + s_{cl,k} \tag{23}$$

The source terms $s_{br,k}$ and $s_{cl,k}$ model breakup and coalescence through empirical models described in Lo and Zhang (2009). The critical Weber number used in these models is set to 0.5 for both phases, cf. Hill (1998).

To ensure a stable simulation, the droplet size is initially modeled empirically. Here, a model by Brauner (2001) is employed to estimate the maximum droplet diameter

$$\frac{d_{\max}}{D} = 7.61\mathrm{We}_c^{-0.6}\mathrm{Re}_c^{0.08}\left(\frac{\alpha_d}{\alpha_c}\right)^{0.6}\left(1+\frac{\rho_d}{\rho_c}\frac{\alpha_d}{\alpha_c}\right)^{-0.4} \tag{24}$$

where We_c and Re_c are the Weber and Reynolds number of the continuous phase. The Reynolds number is the ratio of inertial to viscous forces; whereas, the Weber number is the ratio of inertial forces to surface tension

$$\mathrm{Re} = \frac{\rho U D}{\mu} \tag{25}$$

$$\mathrm{We} = \frac{\rho U^2 D}{\sigma} \tag{26}$$

Empirical studies and observations from experiments typically report the maximum diameter $d_{\max}$. The ratio between the maximum observed diameter and the Sauter mean diameter has been reported from experimental studies by Angeli and Hewitt (2000) to

$$d_{32} = 0.48\, d_{\max} \tag{27}$$

2.4 Flow Conditions

The physics describing the model shows the complex array of parameters affecting the flow. The parameters of the validation are described in Table 1. To simplify the variation study, flow parameters are described in terms of nondimensionalized numbers. A variety of different dimensionless quantities can be considered. In this study, the Atwood and Richardson numbers are studied to account for Rayleigh-Taylor and the Kelvin-Helmholtz instabilities. These two instabilities are considered relevant for the stability of the interface and thus the transition between flow patterns. Aside from the aforementioned, the more typical fluid dynamics characteristics are described through the Reynolds and Weber numbers from Eqs. (25) and (26) as well as the Froude number (Fr), which characterizes the ratio of gravity to inertial forces

$$\mathrm{Fr} = \frac{U}{\sqrt{g_y D}} \tag{28}$$

TABLE 1: Parameters from experimental reference study (Elseth, 2001; Kumara et al., 2009) and wetting contact angle estimated from dos Santos et al. (2006)

Parameter	Value
Pipe diameter, D	0.0563 m
Oil density, ρ_o	790 kg/m^3
Oil viscosity, μ_o	0.00164 Pa s
Water density, ρ_w	1000 kg/m^3
Water viscosity, μ_w	0.00102 Pa s
Surface tension, σ	0.043 N/m
Wetting contact angle, θ_w	41°

The Atwood number describes the ratio of the difference in density to the average density and is often arises as a factor for instabilities in two-phase flows. The Atwood number arises analytically from analysis of the Rayleigh-Taylor instability (Glimm et al., 2001; Taylor, 1950)

$$\mathrm{A} = \frac{\rho_w - \rho_o}{\rho_w + \rho_o} \tag{29}$$

The Richardson number describes the ratio of buoyancy forces to shear forces. It arises from stability analysis of the Taylor-Goldstein equation as the criterion for stability of the Kelvin-Helmholtz instability. This describes the stability of a shear flow with a density gradient (Goldstein, 1931; Taylor, 1931). Locally for a pure shear flow in an inviscid incompressible fluid with a uniform density gradient, it is defined as follows:

$$\mathrm{Ri} = \frac{-g_y}{\rho} \frac{\partial \rho / \partial y}{|\partial u_x / \partial y|^2} \tag{30}$$

For an interface with a nonuniform density or velocity gradient, an average global cross-sectional Richardson number is approximated as the ratio of the Atwood number to the square of the Froude number

$$\mathrm{Ri} = \frac{\rho_w - \rho_o}{\rho} \frac{g_y D}{U^2} \approx \frac{2A}{\mathrm{Fr}^2} \tag{31}$$

For inviscid stratified pure shear flow, stability analysis shows that all wavelengths are stable for $\mathrm{Ri} > 0.25$ (Hazel, 1972). For the viscous flow, viscosity acts as a damping factor when Re is low but has more complex effects in higher Reynolds numbers, where the surface tension further dampens the instability of the interface (Drazin and Reid, 2004; Turner, 1973).

The flow conditions of the present study are of a more complex nature with phase distribution and boundaries giving lead to nonuniform density and velocity gradients. Hence, the criterion of Ri is not well-defined. However, the expected trend is that the stability of the interface is stabilized with increased Atwood number or decreased Froude number.

2.5 Numerical Model

The domain boundary is divided into two inlets, a symmetry plane, a wall, and an outlet as illustrated in Fig. 2. The inlets are given Dirichlet boundary conditions with prescribed phase-velocities $\mathbf{u}_k$, volume fraction α_k, droplet sizes $d_{32,k}$, turbulent intensity I_k, and viscosity ratio $\mu_{k,t}/\mu_k$. The pressure is extrapolated from the domain through reconstruction gradients. The turbulent intensity is set to 0.01, and the viscosity ratio to 10 as per STAR–CCM+ defaults. Variation of inlet turbulence has been tested with little effect on the downstream results. The inlet droplet Sauter mean diameter is defined with a mean and variance of both $0.7D/2$.

The outlet is modeled by specifying the pressure to the hydraulic pressure based on the flow-rate averaged density using a Dirichlet condition. Other flow variables are extrapolated.

Symmetry in the plane spanned by the gravitational vector and axial direction of the pipe is exploited by a symmetry boundary condition (homogeneous Dirichlet on the normal component of the flow and homogeneous Neumann condition on the normal derivatives of all other equation variables).

The walls are modeled as no-slip walls with homogeneous Dirichlet conditions on the velocity field. The turbulence is modeled using a high y^+ wall treatment model because the wall boundary layer is not sought to be resolved (Shih et al., 1995).

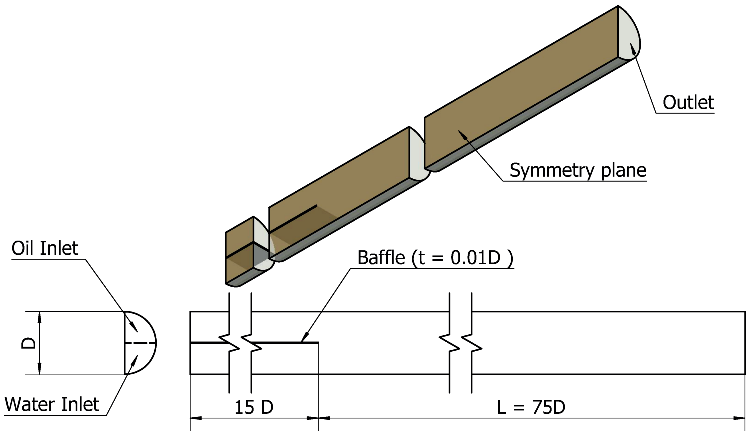

FIG. 2: Illustration of the computational domain. The length of $L = 75D$ is established by a pipe-length study described in Section 2.

The procedure of obtaining a numerical solution to the two-fluid model is split into three steps for the sake of numerical stability and convergence. Initially, a steady-state version of Eqs. (1) and (2) is solved by setting the time derivatives to zero. This has proven numerically unstable along with the droplet size distribution model and is instead carried out with a static constant droplet size determined by Eq. (24). The steady-state analysis is run for 1000 iterations. Subsequently, the simulation is switched to a transient analysis. Here, the S-gamma droplet size distribution is solved passively, i.e., without coupling the resulting droplet size to the terms for the momentum equation. This second step is solved with a Courant number of 5 and 40 inner iterations for a physical time of $tU/L = 0.7$. Finally, the droplet sizes used in the momentum equation is coupled to the S-gamma model and solved for another $tU/L = 0.75$ of physical time with a Courant number of 0.1 and a time-step convergence tolerance of 10^{-6} on all equation residuals.

The domain is presented in a Cartesian coordinate system with its origin at the mixing point of the incoming flows, the x-axis following the axial direction of the pipe, the z-axis horizontal in the gravitational field, with the y-axis following the pipe, aligned with gravity for the horizontal pipe. The computational domain is discretized by a rectangular trimmer mesh-grid, with cells in the axial direction of the pipe twice as long as in the radial. The grid sizing is controlled with a single nondimensional parameter $\hat{\delta}$. The cells located in the core of the domain is set to size $\delta = \hat{\delta} D$, where D is the diameter of the pipe. The traverse directions are refined to 0.25δ, and the boundaries are kept as quadratic with a maximum cell-to-cell stretch of 2. This gives a mesh as shown in Fig. 3.

The computational domain corresponding to the full experimental setup is computationally expensive to run. Therefore, a study is carried out to evaluate the necessary length of pipe needed for the phase distribution to have reached a constant state.

The validation is carried out by comparing the densitometry measurements presented by Kumara et al. (2009) to the postprocessed Reynolds-averaged numerical results. The postprocessing takes the cross-sectional volume fraction average in the z-direction to replicate the density line measurements of the densitometry. The data presented on a plot with the average volume fraction on the horizontal axis and the radius-normalized y-position on the vertical axis. From the

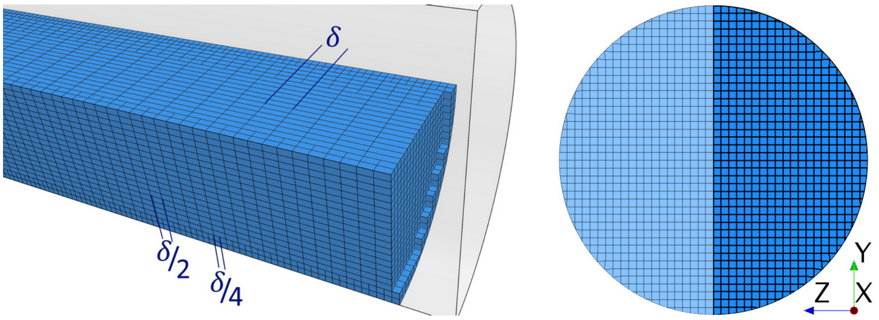

FIG. 3: (left) Illustration of the grid and picture extracted at the outlet of the pipe seen from the symmetry plane with a section cut out to reveal the interior of the grid domain. (right) Cross-sectional mesh (with opaque symmetry).

phase distributions, the level of dispersion and liquid holdup can be evaluated from Eq. (32). An example of such a cross-sectional volume fraction density plot can be seen in Fig. 4.

In a horizontal steady flow, a simple force consideration on the two fluids is employed in the x direction; each phase has a pressure gradient, viscous forces, and interfacial forces acting on it. The interfacial forces exerted are Newton's third law pairs. Given a fixed pressure gradient, the location of the interface is controlled by a force balance of the viscous and pressure gradient. For identical viscosities, the solution would tend to equal the inflow ratio such that the area integral of the volume fraction of water (α_w) over a cross section would equal the water-cut. As the viscosities differ, the interface moves and one phase moves slower relative to the other. This difference in velocity gives rise to liquid holdup, i.e., the phase volume ratio in the pipe of each phase is not equal to the water-cut. With the higher viscosity of the oil, a higher holdup of oil is expected. As the pipe is inclined (with the flow moving upward), gravity acts stronger on

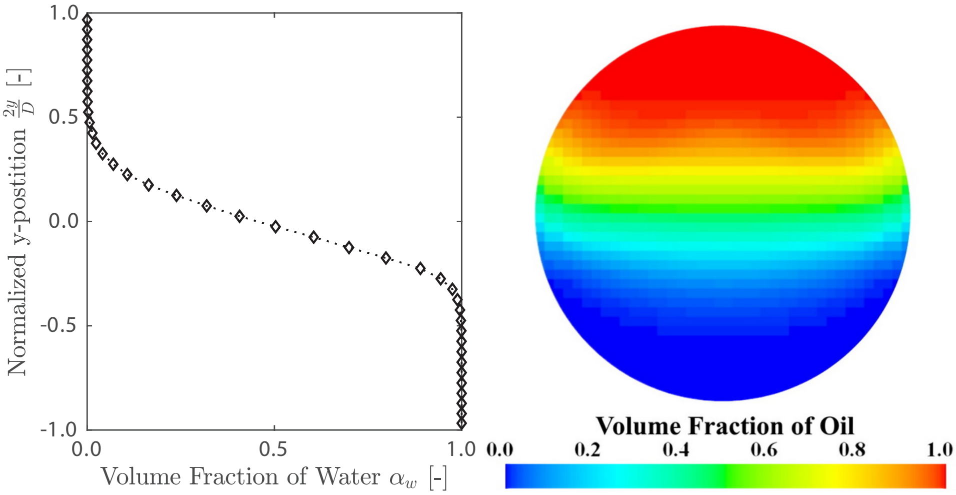

FIG. 4: (left) Postprocessing illustration of cross-sectional volume fraction density and (right) the corresponding phase distribution

the denser fluid and higher holdup of water is expected. The holdup of water increases water-wetting in the pipe and thus increases the risk of exposing the surface to corrosion and scale formation. On the phase distribution profiles, liquid holdup is indicated by the area under the curve differing from the water-cut. The rate of dispersion is indicated by the slope of the curve. The liquid holdup of water, Z_w, is postprocessed as the volume integral of the volume fraction of water divided by the total volume V_T in a five diameter long section of the pipe. A volume integral is used to average the cross-sectional area based liquid holdup smoothing out small variations in the axial direction of the pipe

$$Z_w = \frac{1}{V_T} \int_{V_T} \alpha_w dV \tag{32}$$

The numerical model implemented solves for averaged flow quantities due to the Reynolds averaging as well as the Eulerian description of the phase distribution in each computational cell. Consequently, an assumption is taken to provide a description of the wetting of the walls. In this study, the water-wetting of the wall, W_w, is assumed equal to the surface integral of the extrapolated water volume fraction from the adjacent cells, $\alpha_{w,\text{wall}}$ divided by the total area of the wall A_{wall}:

$$W_w = \frac{1}{\text{A}_{\text{wall}}} \int_{\text{A}_{\text{wall}}} \alpha_{w,\text{wall}} d\text{A} \tag{33}$$

This assumes the wetting to be independent on the expected underlying flow pattern (e.g., water droplets dispersed in oil).

3. RESULTS AND DISCUSSION

This section describes the validation of the present CFD model with experimental data from Kumara et al. (2009), and an analysis based on the validated model with purpose of understanding how water-wetting of the surface is controlled by flow properties. The flow cases used for validation are listed in Table 2.

3.1 Pipe Length Independence Study

A study of the pipe length for the CFD model required to converge to a constant phase distribution profile is performed to reduce the number of computational cells used in the subsequent convergence and variation studies. The results from Kumara et al. (2009) are used as a reference.

TABLE 2: Input condition for the different case studies in the validation analysis. U is the mean velocity, ψ is the water cut, Re the Reynolds number, Ri is the Richardson number, Fr is the Froude number, We is the Weber number, and β the inclination angle. The Atwood number is constant ($\text{A} = 0.12$) as no variations in fluid properties have been tested in the experiments referenced

β (deg)	**U (m/s)**	**ψ (%)**	**Re**	**Ri**	**Fr**	**We**
0	1.0	50	38,000	0.13	1.3	1200
0	1.5	50	57,000	0.06	2.0	2600
0	1.5	75	68,000	0.06	2.0	2800
5	1.0	50	38,000	0.13	1.3	1200

The study is performed on a medium-fine mesh of grid size $\hat{\delta} = 0.15$ on a pipe of total length of $265D$. An extract of the results at different x-positions is shown in Fig. 5.

It is observed that while the results, using an intermediate grid size $\hat{\delta} = 0.15$, display some differences with the experimental, the profiles do converge from $\sim$ 50 diameters downstream until approximately five diameters before the outlet where the profile evolves leading up to the boundary. In the remainder of this work, a pipe length of $75D$ is used with sampling at $x = 55D$.

Another study is performed for the necessary pipe length upstream from the mixing point in order for the velocity profile to develop (not shown). Here, a length of 15 diameters is concluded to be sufficient length preceding the mixing point. It is noted that wave in the interface occur in the earlier section of the pipe with a wavelength of approximately five to six diameters. The results are time-averaged over a timespan based on wave period assuming the wave travels with the mean flow velocity.

3.2 Mesh Convergence Study

A study of the spatial resolution is conducted on four cases for horizontal flows with a mean velocity of $U = 1.0$ and $U = 1.5$ m/s using water-cuts of $\psi = 50$ and $\psi = 75\%$ as well as upward inclined flows angled at $\beta = 0$ and $\beta = 5$ deg at $U = 1$ m/s mean velocity and $\psi = 50\%$ water-cut.

For the horizontal flow at $U = 1.0$ m/s with $\psi = 50\%$ water-cut, four mesh sizes are tested, $\hat{\delta} \in [0.4, 0.2, 0.1, 0.05]$. The results are shown in Fig. 6(a). It is seen that the y-position at which the first oil is observed converges toward the experimental observations; whereas, the gradient of the volume fraction converges toward a result with slightly overpredicted dispersion.

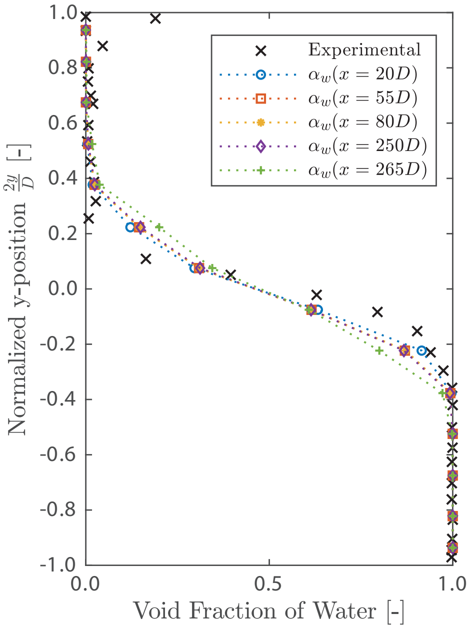

FIG. 5: Comparison of cross-sectional phase distribution at different x-positions. Horizontal flow, $U = 1.0$ m/s, $\psi = 50\%$. Experimental reference by Kumara et al. (2009).

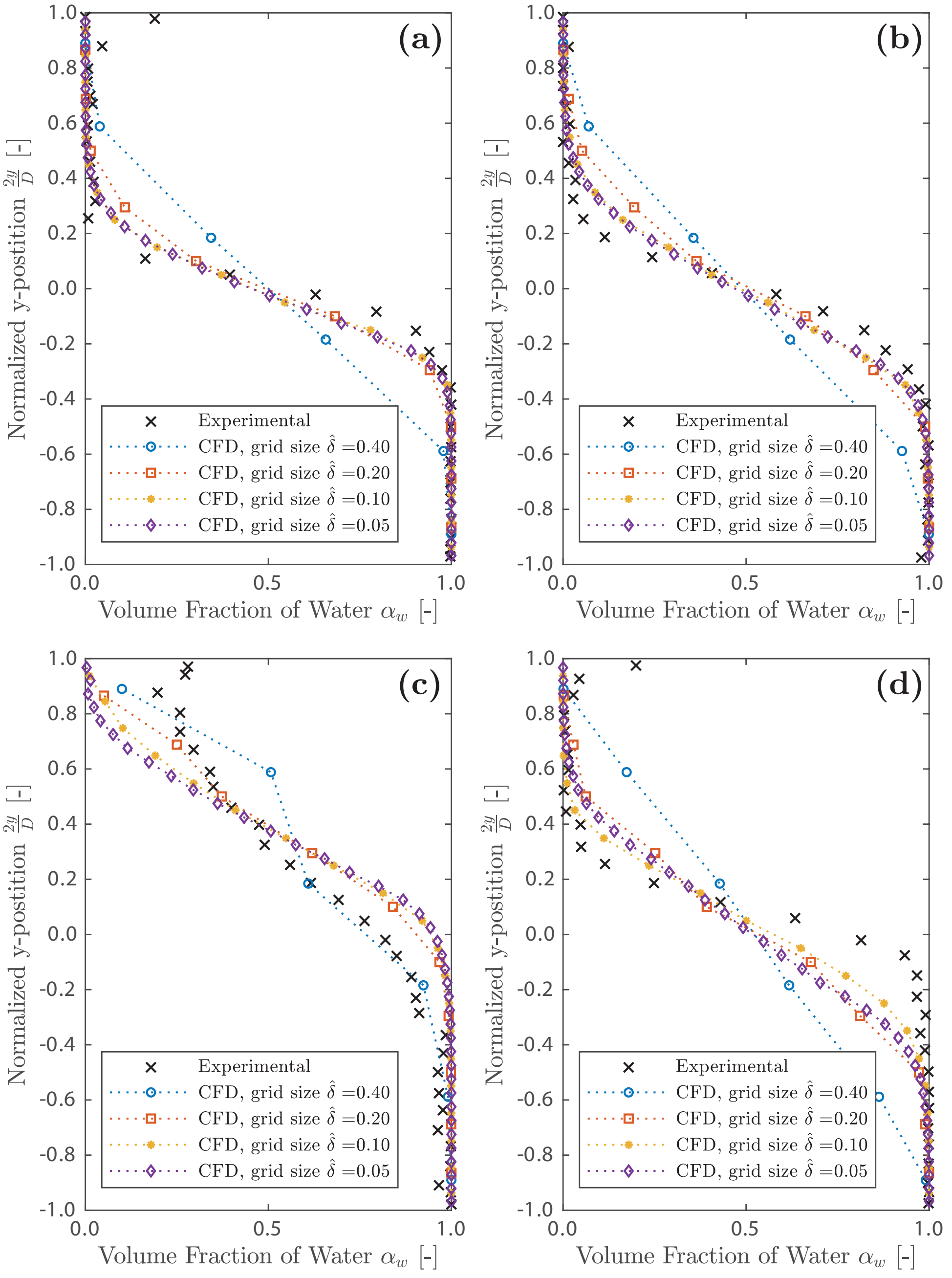

FIG. 6: Mesh convergence study showing cross-sectional volume fraction averages for four successively decrementing grid sizes: (a) horizontal flow, $U = 1.0$ m/s, $\psi = 50\%$; (b) horizontal flow, $U = 1.5$ m/s, $\psi = 50\%$; (c) horizontal flow, $U = 1.5$ m/s, $\psi = 75\%$; and (d) $\beta = 5^\circ$ upward inclined flow, $U = 1.0$ m/s, $\psi = 50\%$. Experimental reference by Kumara et al. (2009).

Near the bottom and top of the pipe ($2y/D = -1$ and $2y/D = 1$), the experimental results are not accurate and the deviations ignored (Kumara et al., 2009). Observed deviations in the experimental data suggest that the deviations lie within the expected uncertainty.

With increasing flow velocity, the phases disperse more. Similarly to the slower flow, the simulation run at $U = 1.5$ m/s mean velocity shown in Fig. 6(b) yields convergence toward a result slightly more dispersed than the experimental. On the contrary, at $\psi = 75\%$ water-cut, as shown in Fig. 6(c) the model does not seem to converge within the mesh sizes and seems to under-predict the level of dispersion.

As the pipe is inclined, transition to a wavy flow is expected where the time average would yield higher dispersion. For the upward inclined flow at 5 deg [Fig. 6(d)] similar convergence as for the horizontal flows is observed. Notably, the phase distribution profiles converges at around $\hat{\delta} = 0.1$ for all the cases.

3.3 Droplet Size Comparison

The droplet size distribution resulting from the S-gamma model is visually shown in Fig. 7 and compared to droplets visually observed during experimental work by Elseth (2001) in Table 3. The modeled droplet sizes were sampled over a five-diameter test section and maximums taken. As the modeled droplets were the Sauter mean diameter, they are divided by 0.48 to compare

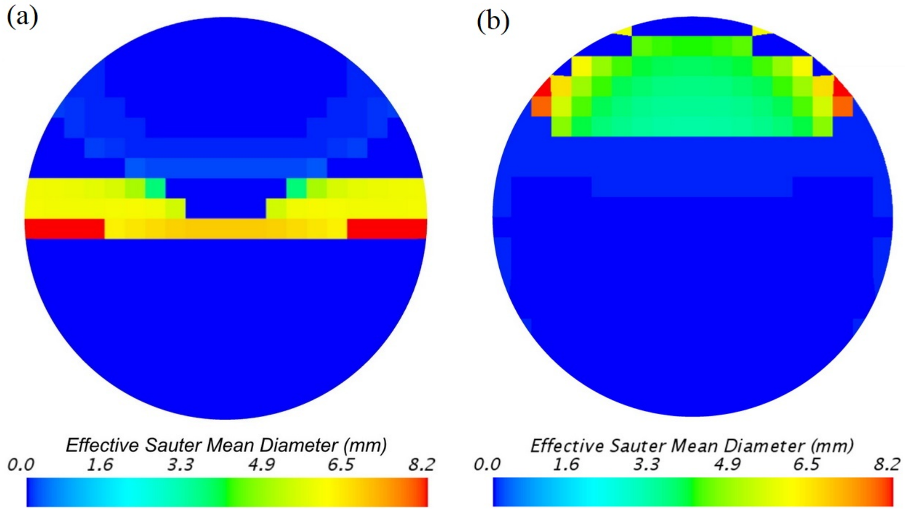

FIG. 7: Cross-sectional droplet Sauter mean diameters d_{32} at $x = 55D$ and horizontal flow, $U = 1.0$ m/s, and (a) $\psi = 50\%$ and (b) $\psi = 75\%$

TABLE 3: Comparison between the experimentally observed droplet sizes from Elseth (2001) and the CFD results taken at $x = 55D$ as well as the empirical correlations from Brauner (2001)

β (deg)	U (m/s)	ψ (%)	Exp. (mm)	CFD (mm)	Emp. (mm)
0	1.0	50	3	12.8	11
0	1.0	75	8	8.1	9

to maximum observed droplet sizes, as described in Eq. (27). From the results, it is seen that the S-gamma model predicts a droplet size consistent with the empirical correlation but seems to overestimate droplet sizes compared to the experimental observations. This could be due to limitations in the breakup and coalescence models or inaccurate model parameters.

3.4 Water-Wetting, Liquid Holdup and Dispersion

A study is performed on quantification of water-wetting along with an estimation of liquid holdup and dispersion with variations in the Froude, Richardson, and Atwood numbers. For this study, a grid size of $\hat{\delta} = 0.1$ is used and the analysis data are extracted from a pipe section between $x = 55D$ and $x = 60D$. The models are run at $\beta = 5°$ inclination with $U = 1.0$ m/s mean velocity and $\psi = 50\%$ water-cut.

The effect of the Froude number is simulated using three different gravitational constants, thereby keeping all other flow parameters constant. The resulting variations of the liquid holdup and water wetting are listed in Table 4. It is seen that the liquid holdup decreases for increasing Froude numbers as the effect of difference in densities is reduced. At the same time, the water-wetting increases slightly. This can be described by a higher dispersion. This is shown in the density-plot in Fig. 8(a), where it is seen that the rate of dispersion increases with the Froude number.

The density difference characterized through the Atwood number is analyzed while keeping the mean density and thus the rest of the flow properties constant. The results are listed in Table 5 and shown as cross-sectional density plots in Fig. 8(b). Here, the increase of the Atwood number shows a larger liquid holdup with a lower dispersion. The water-wetting remains roughly constant.

4. CONCLUSIONS

The present study has employed a CFD model to capture the flow patterns and phase distribution in a two-phase oil and water flow. The model has been refined and validated against experimental data with mean flow velocity of $U = 1.0$ and $U = 1.5$ m/s and water-cuts $\psi = 50$ and $\psi = 75\%$. Here, the model shows good convergence and agreement with the experimental data in terms of phase distribution. The S-gamma model produces droplet sizes in good agreement with empirical correlations but overpredicts compared to those observed in experiments. This suggests that more work is necessary for an accurate prediction of the droplet size distribution. The physics causing the phase distribution are decomposed into dispersion and liquid holdup. This is used to analyze surface wetting for a set of Atwood and Froude numbers. The results show how the Atwood number balances dispersion to liquid holdup having a rather constant water-wetting; whereas, the water-wetting increases with the Froude number, although the liquid holdup is reduced. Both the Atwood number and the Froude number affect the Richardson number. It is clear that an

TABLE 4: Variation of the Froude number and the resulting Richardson number; mean velocity $U = 1.0$ m/s, inclination $\beta = 5$ deg, Re = 38,000, A = 0.12, and We = 1200

Fr	Ri	ψ (%)	Liquid holdup (%)	Water-wetting (%)
1.0	0.51	50	53.5	54.1
1.3	0.26	50	51.4	54.0
1.9	0.13	50	51.0	55.1

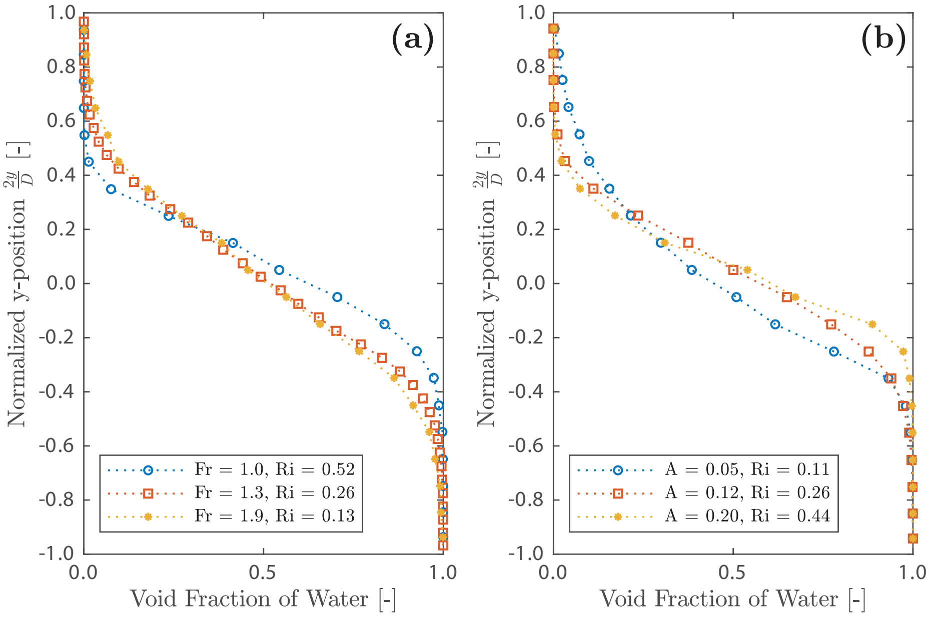

FIG. 8: Cross-sectional density plots at $U = 1.0$ m/s, $\psi = 50\%$, $\beta = 5$ deg, Re = 38,000, We = 1200: (a) variation of the Froude number at A = 0.12 and (b) variation of the Atwood number at Fr = 1.3

TABLE 5: Variation of the Atwood number and the resulting Richardson number; mean velocity $U = 1.0$ m/s, inclination $\beta = 5$ deg, Re = 38,000, Fr = 1.3, and We = 1200

A	Ri	ψ (%)	Liquid holdup (%)	Water-wetting (%)
0.05	0.11	50	50.3	55.2
0.12	0.26	50	51.4	54.0
0.20	0.44	50	54.0	54.7

increased Richardson number stabilizes the flow as expected from the relation to the Kelvin-Helmholtz instability.

REFERENCES

Angeli, P. and Hewitt, G.F., Drop Size Distributions in Horizontal Oil-Water Dispersed Flows, *Chem. Eng. Sci.*, vol. **55**, no. 16, pp. 3133–3143, 2000.

Auton, T.R., Hunt, J.C.R., and Prud'Homme, M., The Force Exerted on a Body in Inviscid Unsteady Non-Uniform Rotational Flow, *J. Fluid Mech.*, vol. **197**, pp. 241–256, 1988.

Brackbill, J.U., Kothe, D.B., and Zemach, C., A Continuum Method for Modeling Surface Tension, *J. Comput. Phys.*, vol. **100**, no. 2, pp. 335–354, 1992.

Brauner, N., The Prediction of Dispersed Flows Boundaries in Liquid-Liquid and Gas-Liquid Systems, *Int. J. Multiphase Flow*, vol. **27**, no. 5, pp. 885–910, 2001.

Cerne, G., Petelin, S., and Tiselj, I., Coupling of the Interface Tracking and the Two-Fluid Models for the Simulation of Incompressible Two-Phase Flow, *J. Comput. Phys.*, vol. **171**, pp. 776–804, 2001.

Coste, P., A Large Interface Model for Two-Phase CFD, *Nucl. Eng. Des.*, vol. **255**, pp. 38–50, 2013.

dos Santos, R.G., Mohamed, R.S., Bannwart, A.C., and Loh, W., Contact Angle Measurements and Wetting behavior of Inner Surfaces of Pipelines Exposed to Heavy Crude Oil and Water, *J. Pet. Sci. Eng.*, vol. **51**, pp. 9–16, 2006.

Drazin, P.G. and Reid, W.H., *Hydrodynamic Stability*, 2nd Ed., Cambridge, UK: Cambridge University Press, 2004.

Elseth, G., An Experimental Study of Oil/Water Flow in Horizontal Pipes, PhD, Telemark University College, 2001.

Glimm, J., Grove, J.W., Li, X.L., Oh, W., and Sharp, D.H., A Critical Analysis of Rayleigh-Taylor Growth Rates, *J. Comput. Phys.*, vol. **169**, no. 2, pp. 652–677, 2001.

Goldstein, S., On the Stability of Superposed Streams of Fluids of Different Densities, *Proc. R. Soc. A*, vol. **132**, no. 820, pp. 524–548, 1931.

Hazel, P., Numerical Studies of the Stability of Inviscid Stratified Shear Flows, *J. Fluid Mech.*, vol. **51**, no. 1, pp. 39–61, 1972.

Hill, D.P., An Experimental Study of Oil/Water Flow in Horizontal Pipes, PhD, University of London, 1998.

Hirt, C.W. and Nichols, B.D., Volume of Fluid (VOF) Method for the Dynamics of Free Boundaries, *J. Comput. Phys.*, vol. **39**, no. 1, pp. 201–225, 1981.

Ishii, M. and Hibiki, T., *Thermo-Fluid Dynamics of Two-Phase Flow*, 2nd Ed., New York: Springer, 2006.

Kumara, W.A.S., Elseth, G., Halvorsen, B.M., and Melaaen, M.C., Computational Study of Stratified Two Phase Oil/Water Flow in Horizontal Pipes, *HEFAT 2008*, Citeseer, 2008.

Kumara, W.A.S., Halvorsen, B.M., and Melaaen, M.C., Pressure Drop, Flow Pattern and Local Water Volume Fraction Measurements of Oil-Water Flow in Pipes, *Meas. Sci. Technol.*, vol. **20**, p. 114004, 2009.

Lamb, S.H., *Hydrodynamics*, 6th Ed., New York: Dover Publications, 1932.

Lance, M. and Bataille, J., Turbulence in the Liquid-Phase of a Uniform Bubbly Air Water-Flow, *J. Fluid Mech.*, vol. **222**, pp. 95–118, 1991.

Lo, S. and Zhang, D., Modelling of Break-Up and Coalescence in Bubbly Two-Phase Flows, *Int. Comm. Heat Mass Transfer*, vol. **1**, no. 1, pp. 23–38, 2009.

Muzaferija, S. and Peric, M., Computation of Free Surface Flows Using Interface-Tracking and Interface-Capturing Methods, *Numer. Heat Transfer, Part B*, vol. **32**, no. 4, pp. 369–384, 1997.

Pouraria, H., Seo, J.K., and Paik, J.K., A Numerical Study on Water Wetting Associated with the Internal Corrosion of Oil Pipelines, *Ocean Eng.*, vol. **122**, pp. 105–117, 2016.

Prosperetti, A. and Tryggvason, G., *Computational Methods for Multiphase Flow*, Cambridge, UK: Cambridge University Press, 2007.

Schiller, L. and Naumann, A., Über Die Grundlegende Berechnungen Bei Der Schwerkraftaufbreitung, *Z. Ver. Deutsch. Ing.*, vol. **77**, no. 12, pp. 318–320, 1933.

Schümann, H., Khatibi, M., Tutkun, M., Pettersen, B.H., Yang, Z., and Nydal, I.J., Droplet Size Measurements in Oil-Water Dispersions: A Comparison Study Using FBRM and PVM, *J. Disp. Sci. Tech.*, vol. **36**, no. 10, pp. 1432–1443, 2015.

Shih, T., Liou, W.W., Shabbir, A., Yang, Z., and Zhu, J., A New k-ϵ Eddy Viscosity Model for High Reynolds Number Turbulent Flows, *Comput. Fluids*, vol. **24**, no. 3, pp. 227–238, 1995.

Strubelj, L., Tiselj, I., and Mavko, B., Simulations of Free Surface Flows with Implementation of Surface Tension and Interface Sharpening in the Two-Fluid Model, *Int. J. Heat Fluid Flow*, vol. **30**, no. 4, pp. 741–750, 2009.

Taylor, G.I., Effect of Variation in Density on the Stability of Superposed Streams of Fluid, *Proc. R. Soc. A*, vol. **132**, no. 820, pp. 499–523, 1931.

Taylor, G.T., The Instability of Liquid Surfaces when Accelerated in a Direction Perpendicuar to Their Planes, *Proc. R. Soc. Lond.*, vol. **201**, pp. 192–196, 1950.

Turner, J.S., *Buoyancy Effects in Fluids,* Cambridge, UK: Cambridge University Press, 1973.

3 Paper 2: The influence of turbulent transport in reactive processes: A combined numerical and experimental investigation in a Taylor-Couette reactor

Chemical Engineering Journal 421 (2021) 129591

Contents lists available at ScienceDirect

Chemical Engineering Journal

journal homepage: www.elsevier.com/locate/cej

The influence of turbulent transport in reactive processes: A combined numerical and experimental investigation in a Taylor-Couette reactor

Benaiah U. Anabaraonye [a,*], Jakob R. Bentzon [b,*], Ishaq Khaliqdad [c], Karen L. Feilberg [a], Simon I. Andersen [a], Jens H. Walther [b,d]

[a] The Danish Hydrocarbon Research and Technology Centre, Technical University of Denmark, Kongens Lyngby 2800, Denmark
[b] Department of Mechanical Engineering, Technical University of Denmark, Kongens Lyngby 2800, Denmark
[c] Department of Chemistry, Technical University of Denmark, Kongens Lyngby 2800, Denmark
[d] Computational Science and Engineering Laboratory, ETH, Zürich CH-8092, Switzerland

ARTICLE INFO

Keywords:
CFD
Taylor-Couette
Turbulence-kinetic interactions
Precipitation
Anisotropic turbulence
Large eddy simulation

ABSTRACT

Turbulent reactive flows are ubiquitous in industrial processes. Decoupling transport effects from intrinsic chemical reactions requires an in-depth understanding of fluid flow physics; computational fluid dynamics (CFD) methods have been widely used for this purpose. Most CFD simulations of reactive liquid-phase flows, where the Schmidt numbers are large, rely on isotropic eddy viscosity models. However, the assumption of turbulent isotropy in most stirred reactors and wall-bounded flows is fundamentally incorrect and leads to erroneous results. Here, we apply a systematic CFD approach to simulate liquid-phase diffusive and convective transport phenomena that occur in a Taylor-Couette (TC) reactor. We resolve the turbulent flow by extracting statistics from large eddy simulation which is used to tune the anisotropic Reynolds stress model. In addition, we conducted a series of turbulent precipitation and mixing studies in a TC reactor that was designed and fabricated in-house. The numerical model is successfully validated against a published torque correlation and it is found to accurately describe the advection and diffusion of chemical species. The validated model is then used to demonstrate key flow properties in the reactor. We define new local turbulent Peclét numbers to characterize the relative increase in diffusivity from turbulent advection and observe a 29% increase in the turbulent contribution as Reynolds number is doubled. Both reactive simulations and experiments show an increase in overall reaction rates with increased turbulence. The results from reactive simulations provide a deeper understanding of flow-kinetics interactions at turbulent conditions.

1. Introduction

The balance between transport phenomena and chemical reactions is typically characterized by the Damköhler number (Da), a ratio of the reaction rate to the transport rate. Depending on the system of interest, Damköhler numbers can either be defined based on advection or diffusion timescales. For instance, in laminar flows, mixing is controlled by molecular diffusion, whereas in a turbulent flow, velocity fluctuations act as an additional diffusion term. In systems where Da $\gg$1 (that is, reaction rates are limited by fluid transport), the presence of turbulence will play a significant role in the local transport of chemical species, and this could affect reactant conversion and product selectivity [1]. Since turbulent flows are fundamental to many industrially relevant chemical processes, the analysis of the turbulence-kinetics interactions (TKI) [2] is necessary to decouple intrinsic chemical reaction rates from the effects of fluid transport. This can be achieved through the numerical modeling of flow and chemistry on a microscale level.

Numerical modeling using computational fluid dynamics (CFD) allows the turbulence and advection of chemical species to be resolved locally. However, it relies on experimental studies to ascertain the validity of the underlying assumptions of the mathematical models. Therefore, a combined experimental and numerical approach is sought to describe and analyze the different phenomena influencing the TKI.

For an experimental cell to be used in parallel with modeling, it would require well-defined boundaries and precise control of the chemical and flow properties. For these reasons, a Taylor-Couette (TC) reactor was designed and employed for this study. TC cells primarily consist of two coaxial cylinders where one or both cylinders are capable

---

* Corresponding authors.
E-mail addresses: bana@dtu.dk (B.U. Anabaraonye), jroben@mek.dtu.dk (J.R. Bentzon).

https://doi.org/10.1016/j.cej.2021.129591
Received 5 December 2020; Received in revised form 23 March 2021; Accepted 26 March 2021
Available online 10 April 2021
1385-8947/© 2021 Elsevier B.V. All rights reserved.

of rotating. The behavior of fluids enclosed in the annulus of a TC cell has been a fascinating area of study for over three centuries and has played a critical role in the current understanding of various aspects of fluid dynamics [3–5]. The ability to independently vary flow regimes and shear forces make TC devices an attractive option in many processes including viscometry [6], precipitation [7–10], flocculation [11,12], polymerization [13,14], and crystal size control [15,16]. Previous experimental investigations in TC cells have included the use of flow visualization methods, particle image velocimetry (PIV), direct wall shear stress and torque measurements, and effluent analysis [7,10,17–19]. Results from these studies have led to the development of several empirical correlations over a wide range of Reynolds numbers (Re), including those that determine the scaling of the rotor torque [17,20,21]. These correlations make the validation of the flow within the TC cell possible without reliance on precise torque and velocity measurements. A significant finding is the occurrence of a transition that occurs at $\mathrm{Re} = 1.3 \times 10^4$ above which TC flow has properties comparable to wall-bounded shear flows (such as pipe and duct flow) and follows a Prandtl-von Karman-type law [4,17,22]. These observations have led to the use of TC-based devices in extracting parameters relevant to turbulent pipe flows [9,23].

CFD models are typically categorized by the degree to which they resolve the turbulent time and length scales [24]. Among the most commonly applied are the Reynolds-averaged Navier-Stokes (RANS) models which simulate time-averaged solutions and use closure models to account for the influence of flow fluctuations on the diffusivity of momentum, mass, and energy. These models rely on empirical correlations to estimate the magnitude of these diffusivities. Thus, they require a similarity between the flow from which they are validated and tuned to, and the attempted simulated flow. In contrast, direct numerical simulations (DNS) resolve all lengths and time scales of the flow [25]. While a DNS simulation would be ideal, computational resources limit such attempts in terms of domain size and simulated physical time. An increasingly applied method is the large eddy simulation (LES) which uses spatial low-pass filtering to resolve the larger energy-carrying turbulent eddies while the smaller dissipative eddies are modeled with closure terms [24]. By only filtering out the smaller eddies, high-accuracy LES simulations can be achieved with significantly lower computational costs compared to DNS. Furthermore, results from LES simulations can be used to tune the empirical correlations of RANS simulations to resolve a longer time scale. This is the modeling approach taken in this study. The most commonly applied RANS models are the two-equation eddy viscosity models k-ε and k-ω. However, wall-bounded and rotational flows are often governed by highly anisotropic turbulence which these simpler RANS models do not resolve. For these complex flows, the Reynolds stress models (RSM) are more appropriate [26,27].

CFD methods have been widely used to simulate reactive flow. For example, Lysenko et al. [28] demonstrated the use of LES and DNS simulations to establish accurate modeling parameters for RANS in a methane-air diffusion flame. Similarly, several TKI studies have revolved around gaseous and liquid spray flows in flow regimes where the Schmidt number (Sc), a ratio of viscous momentum dissipation to molecular diffusivity, was close to unity [28,29]. However, for chemical species in aqueous flows where $\mathrm{Sc} \gg 1$, assuming a direct correlation between the turbulent momentum dissipation and turbulent dissipation of dissolved chemical species, could lead to erroneous results [30,31].

To determine the effect of transport on reaction kinetics, several models have been proposed. Specifically, the eddy dissipation concept model [32] is widely used in reactive flow simulations with $\mathrm{Da} \gg 1$ [29]. This model was extended by using a spectral relaxation method to better account for the spectrum of velocity fluctuations in turbulence [33]. Rizzotto et al. [2] showed the use of such a model in a RANS simulation to account for turbulent dissipation through a constant turbulent Schmidt number ($\mathrm{Sc_t}$). This method relies on correlations between the limiting reaction rate and isotropic turbulent statistics – such as the turbulent kinetic energy (TKE) and the turbulent dissipation rate (TDR) – and thus does not capture more complex anisotropic turbulent transport phenomena. Wang et al. [34] compared PIV measurements with different RANS models highlighting the significance of anisotropic turbulence in a TC flow as well as the challenges inherent in modeling the Reynolds stresses accurately. The main challenge with using a RANS model to simulate transport in a turbulent flow is the modeling of the eddy diffusivity from the Reynolds stresses [35]. RANS models typically assume a correlation between the turbulent diffusive transport and the turbulent Reynolds stresses through a constant $\mathrm{Sc_t}$. This assumption makes the transport highly reliant on the accurate modeling of the Reynolds stresses. Marchisio et al. [10] found that in their simulations of barium sulfate precipitation in a TC cell, an anisotropic RANS model yielded significantly better agreement with experimental results when compared to an isotropic RANS model. In the study [10], they applied a constant $\mathrm{Sc_t}$ multiplied by a term that includes both TKE and TDR. Another commonly used model is the generalized gradient diffusion hypothesis (GGDH) which has proven accurate in several experimental studies [36,37]. However, in a study by Silva and Jose [35], where the GGDH turbulent diffusion was compared to results obtained through DNS, it was shown that the model does not accurately capture the local variation in diffusivity. While the model does not accurately capture all the statistics of turbulence, it does account for the anisotropic behavior of turbulence in the eddy diffusivity. A summary of different turbulent Schmidt number correlations shows that on a macroscale, average Schmidt numbers vary between 0.1 and 2.1 [30].

In the literature, the majority of simulations of liquid-phase reactions rely on assumptions and non-validated tuning parameters of RANS models to account for the effects of turbulence. To the best of the authors' knowledge, these assumptions and parameters have not been thoroughly analyzed using scale resolving models such as LES or from PIV studies. In this study, a combined experimental and numerical investigation of the influence of turbulent transport in reactive processes is shown. The use of a validated RANS RSM model to simulate the effect of anisotropic turbulence in high Reynolds number liquid-phase reactive flows is demonstrated.

In this paper, we present the following:

- **The design of a Taylor-Couette reactor**. We designed and fabricated a modular TC reactor. A series of non-reactive (mixing) and reactive (barium sulfate precipitation) experiments were conducted under turbulent flow conditions (Re up to 4.3×10^4) and at a temperature T of 295 K. The reactor configuration had a radius ratio of 0.82 and an aspect ratio of 15.33.
- **Validation of numerical models.** We validated the numerical simulations in two steps. Firstly, the LES models are validated by performing grid size and time-step independence studies, and by comparing the converged torque values to outputs from a widely-cited empirical correlation [20]. Next, the RANS RSM model are tuned to match the results from LES in terms of simulated torque and Reynolds stresses. Secondly, the ability of the model to capture the advection and diffusion of dissolved chemical species is evaluated against data obtained from mixing studies.
- **A systematic method for validating RANS RSM models using LES.** We apply LES modeling to track temporal concentration gradients and turbulence statistics in non-reactive flow studies. The output is used to provide a basis for accurate RANS RSM modeling and to gain a deeper understanding of the underlying mechanisms governing the flow in a TC reactor and how it may influence chemical reactions.
- **Flow visualizations at turbulent flow conditions.** We apply the validated model to extract information on turbulent transport within the reactor. We demonstrate the different flow features present at the regions of experimental interest, the distribution and magnitude of wall shear stress at various angular velocities, the turbulent Reynolds stresses, and surface-normal pressures.

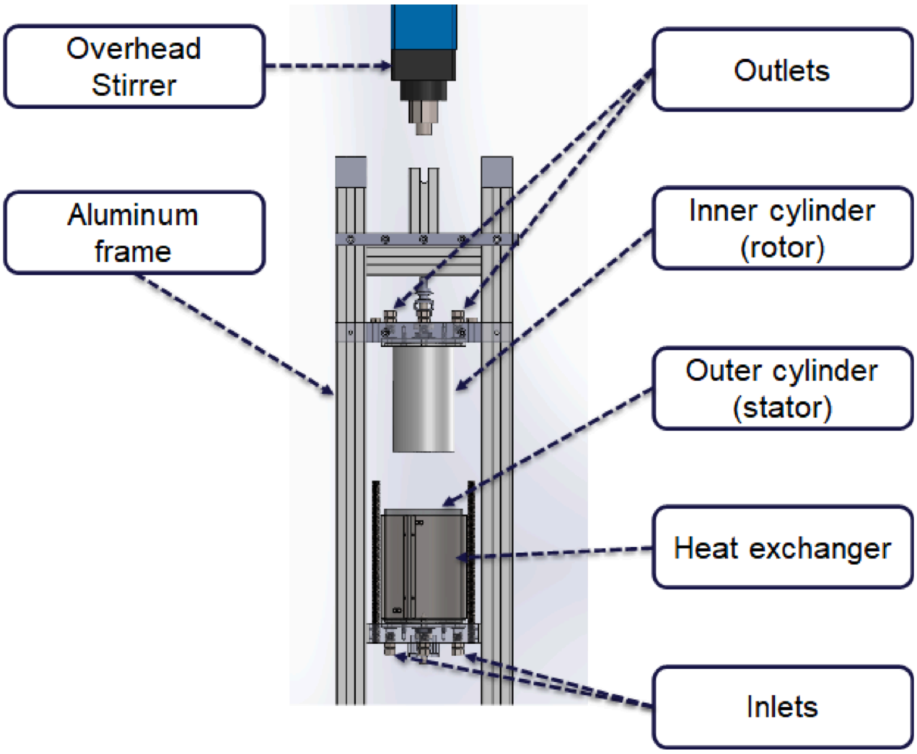

Fig. 1. A CAD representation of the modular TC reactor with key parts labeled.

- **The influence of turbulence on reactive liquid flows.** We apply the validated and tuned models to understand the role of turbulence in a chemical reaction. We introduce turbulent Peclét numbers and relative Damköhler numbers to quantify the effects of turbulence on chemical kinetics. Insights gained from this step are then applied to understanding the precipitation kinetics of barium sulfate at turbulent flow conditions.

2. Experiments

2.1. Taylor-Couette reactor

We designed and constructed a modular TC reactor for turbulent flow studies. The modular design of the reactor allows for flexibility in surfaces and rotor sizes. The reactor and its components were housed in an aluminum frame; a computer-aided drawing (CAD) of the setup is shown in Fig. 1. A detailed description is included in the Supplementary file.

In the current setup, the outer cylinder is stationary while the inner cylinder rotates during operation. The rotor was manufactured in-house from solid polytetrafluoroethylene (PTFE) blocks. Blind holes were drilled on both sides of the cylindrical blocks and were subsequently fitted with stainless steel bushings. At the top, a threaded bushing allowed for attachment to a steering shaft, while at the bottom, the rotor had a SS cone bushing that enabled a non-threaded attachment to the control stick – this minimized undesirable axial rotations. Stable temperatures were achieved using a heat exchanger in contact with the outer surface of the stationary cylinder. Fluid temperatures were measured using a type K thermocouple inserted in the thermowell filled with silicone oil. Rotation in the reactor is provided by a commercial overhead stirrer (IKA® 200 control P4). Rotational speeds were automatically logged in a LabView® based software. We evaluated the control precision of the stirrer and found it to be within ±1% of the desired set points.

Table 1
Properties of the TC Reactor.

Parameter	Value
r_1 (m)	0.040
r_2 (m)	0.049
h (m)	0.138
η	0.82
Γ	15.33

Reynolds number, Re, radius ratio η, and aspect ratio Γ are defined below for a TC setup with a stationary outer cylinder:

$$\mathrm{Re} = \frac{\omega r_1 (r_2 - r_1)}{\nu} \tag{1}$$

$$\eta = \frac{r_1}{r_2} \tag{2}$$

$$\Gamma = \frac{h}{(r_2 - r_1)} \tag{3}$$

here, ω is the angular velocity of the rotating inner cylinder (1/s), r_1 is the radius of the rotating inner cylinder (m), r_2 is the inner radius of the stationary outer cylinder, ν is the kinematic viscosity of the fluid (m^2/s), and h is the rotor height (m). The key properties of the TC reactor are presented in Table 1.

2.2. Materials

All solutions used in this study were prepared gravimetrically. Na_2SO_4, $BaCl_2 \cdot 2H_2O$, and KCl were supplied by Sigma Aldrich® with a stated mass-fraction purity of $\geq$ 99%. Salts were dissolved in ultrapure deionized water produced in-house through reverse osmosis (Millipore ® Q-pod). The injected brine concentrations c_{in} were 8.36×10^{-4} molal and 1.14×10^{-3} molal for barium chloride and sodium sulfate respectively. A solution that quenched barium sulfate reactions was prepared

Table 2
A summary of non-reactive mixing studies.

Experiment	Flow rate (mL/min)	Re
1	16.6	1.1×10^4
2	8.3	2.2×10^4
3	16.6	2.2×10^4
4	16.6	4.3×10^4

using a technical grade diethylenetriamine pentamethylene phosphonic acid (DTMP, ~50%), also supplied by Sigma Aldrich®, and KCl. The mass ratio of DTPMP to KCl in the quenching solution was 1:4.4. The solution *p*H was then adjusted to between 8 and 9 using NaOH.

2.3. Mixing studies

The mixing properties of the TC reactor were investigated at three rotational velocities: 250, 500, and 1000 RPM. A schematic of the overall setup is included in the Supplementary file. At time $t < 0$ s, the reactor was filled with deionized water. At $t \geq 0$ s, both deionized water and a sodium sulfate solution were co-injected at a 1:1 volumetric flow ratio. Four separate mixing experiments, as shown in Table 2, are reported here. Reactor effluents were collected using an autosampler, and temporal changes in both sodium and sulfate concentrations were monitored using an ion chromatography (IC) technique. A solution containing 4.5 mM sodium carbonate and 1.4 mM bicarbonate was used as an eluent for anions whereas, for cations, a 3.0 mM methanesulfonic acid solution was used.

2.4. $BaSO_4$ formation studies

To demonstrate the effects of turbulence on reaction rates, we conducted two reactive studies in the TC reactor. The first study was carried out at 500 RPM and the second at 1000 RPM. Our experimental procedure mirrored that described in the previous section. At time $t < 0$ s, the reactor was filled with sodium sulfate; at $t \geq 0$ s, both solutions (sodium sulfate and barium chloride) were co-injected at a 1:1 volumetric flow ratio. Studies were carried out at ambient conditions ($T = 295$ K) and a total volumetric flow rate of 8.3 mL/min. The formation of barium sulfate is described by

$$BaCl_2 + Na_2SO_4 \rightarrow BaSO_4 + 2NaCl \quad (4)$$

Reactor effluents were collected in vials pre-filled with quenching solutions to prevent further reactions downstream of the reactor. These samples were then filtered using a 0.02 μm syringe filter and diluted in 2% nitric acid. Barium concentrations were measured using an inductively coupled plasma optical emission spectroscopy (ICP-OES) technique. Analytical standards were prepared in a 2% HNO_3 matrix. Samples were run in triplicates; measurements typically had relative standard deviations (RSDs) below 1%.

3. Numerical modeling

The purpose of the models is to generate insights into the interaction between the flow properties, namely turbulence, and chemical kinetics. The numerical model solves the equations of momentum and mass conservation (flow) as well as transport of non-reactive chemical species. As a result, the model predicts the influence of the flow in the reactor on the expected reaction kinetics. In Fig. 2, we illustrate the model validation process applied in this study.

3.1. Empirical models for rotor torque

The numerical model is first implemented and validated using the rotor torque (τ) as the key parameter. This validation is performed first for the LES model to determine the necessary setup of the computational mesh and boundary conditions. We use a correlation first presented by Wendt [20], and discussed in detail by Lathrop et al. [17], that models the non-dimensional torque $G = \tau/(h\rho\nu^2)$ as

$$G = 0.23\frac{\eta^{2/3}}{(1-\eta)^{7/4}}\mathrm{Re}^{1.7} \quad (5)$$

which has yielded accurate results for $10^4 < \mathrm{Re} < 10^5$.

3.2. Flow modeling

CFD flow modeling is carried out using a finite volume method. The models are implemented in STAR–CCM + version 15.02. To model the turbulent flow computationally at both micro and macroscale, both an LES and an RSM model were implemented. Both models assume constant density and molecular diffusivity and apply anisotropic modeling of eddy viscosity on the momentum equation. The dissolved species concentrations are tracked as passive scalars – the effect of their presence on the density and viscosity is neglected.

The CFD models aim to extract statistics on the turbulence in terms of dissipation of momentum and mass. These outputs are used to determine the limiting reaction rate due to species transport. The LES model extracts turbulent statistics on a short timescale to tune turbulence parameters in the time-averaged RSM simulations accurately. The RSM model uses temporal averaging where each parameter, ϕ, is decomposed into a mean, $\overline{\phi}$, and a fluctuating component, ϕ':

$$\boldsymbol{u} = \overline{\boldsymbol{u}} + \boldsymbol{u}', p = \overline{p} + p', c = \overline{c} + c' \quad (6)$$

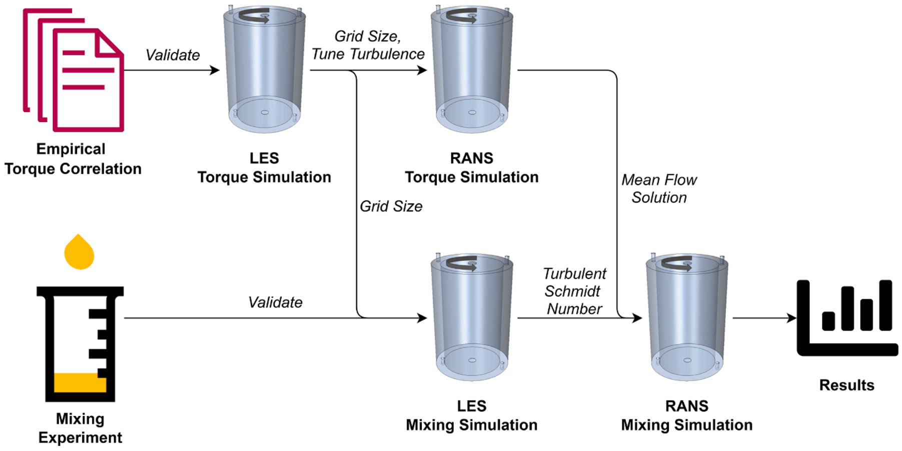

Fig. 2. Illustration of the modeling validation and tuning methodology.

where $\boldsymbol{u}$ is the velocity, p is the pressure, and c is the concentration of a chemical species in molality ($\mathrm{mol/kg_{H_2O}}$). As the momentum conservation equation and transport equations are averaged, a turbulent kinetic energy stress term arises commonly referred to as the Reynolds stress tensor, $\boldsymbol{R} = \overline{\boldsymbol{u}'\boldsymbol{u}'}$. This yields the following Navier-Stokes and transport equations [38]:

$$\frac{\partial\overline{\boldsymbol{u}}}{\partial t}+\nabla\cdot(\overline{\boldsymbol{u}}\otimes\overline{\boldsymbol{u}}) = -\frac{1}{\rho}\overline{p}+\nabla\cdot(v\nabla\overline{\boldsymbol{u}}+\boldsymbol{R}) \tag{7}$$

$$\nabla\cdot\overline{\boldsymbol{u}} = 0 \tag{8}$$

$$\frac{\partial\overline{c}}{\partial t}+\overline{\boldsymbol{u}}\cdot\nabla\overline{c}-\nabla\cdot(D\nabla\overline{c}+\overline{\boldsymbol{u}'c'}) = r_b+r_w \tag{9}$$

where ρ is the density of water (998 $\mathrm{kg/m^3}$), ν is the molecular kinematic viscosity of water ($8.82\times10^{-8}\ \mathrm{m^2/s}$) [39], D is the molecular diffusivity of the dissolved sulfate ($2.13\times10^{-9}\mathrm{m/s}$) [39]. The Kronecker product $\otimes$, the gradient operator ∇, and the time derivatives are numerically approximated using second-order finite volume schemes; r_b is a source term from any bulk reaction and r_w is a source term for a wall reaction.

While the LES model uses spatial – rather than temporal – filtering, the finite grid spacing leads to unresolved eddies that require sub-grid scale (SGS) modeling. These have the same character as the Reynolds stresses and thus an SGS stress tensor, $\boldsymbol{R}_{SGS}$, is introduced based on the wall-adapting linear eddy-viscosity (WALE) model defined in Nicoud and Ducros [40]:

$$\boldsymbol{R}_{SGS} = \nu_{SGS}\nabla\overline{\boldsymbol{u}} \tag{10}$$

where ν_{SGS} is the modeled sub-grid scale viscosity

$$\nu_{SGS} = \Delta^2 S_W \tag{11}$$

here, $\Delta = \min(\kappa d, C_W V^{1/3})$ is the spatial filter width based on the grid cell volume V and the distance to the nearest wall d. The constant C_W is set to 0.325, κ is the von Karman constant. S_W is the deformation parameter defined in Nicoud and Ducros [40].

Utilizing RSM modeling allows simulations to be run at a steady "frozen" flow for a longer time frame at a state of microscale quasi-equilibrium, that is, when turbulence statistics such as the Reynolds stresses have reached a constant mean value. The RSM model is a time-averaged model solving for the mean velocity and pressure and solves a transport equation for each component of the $\boldsymbol{R}(R_{ij})$:

$$\frac{\partial R_{ij}}{\partial t}+\overline{\boldsymbol{u}}\cdot\nabla R_{ij}-\nabla\cdot\left(\nu\nabla R_{ij}+C_S\frac{k_t}{\varepsilon}\boldsymbol{R}\cdot\nabla R_{ij}\right) = P_{ij}+\frac{1}{\rho}\boldsymbol{\phi}-\frac{2}{3}\varepsilon\delta_{ij} \tag{12}$$

where k_t is the turbulent kinetic energy, P_{ij} is the turbulent production tensor [41], $C_s = 0.2$ is a model constant [41], δ_{ij} is Kronecker's delta (1 for $i = j$, else 0) and $\boldsymbol{\phi}$ is the pressure strain tensor. This study uses the elliptic blending model implementation of $\boldsymbol{\phi}$ by Manceau and Hanjalić [26]. The turbulent dissipation rate ε is obtained by solving an additional transport equation:

$$\frac{\partial\varepsilon}{\partial t}+\overline{\boldsymbol{u}}\cdot\nabla\varepsilon-\nabla\cdot\left(\nu+\frac{\nu_t}{\sigma_\varepsilon}\right)\nabla\varepsilon = \frac{\varepsilon}{k}\left(\frac{C_{1\varepsilon}}{\rho}\frac{1}{2}tr(\boldsymbol{P})-C_{\varepsilon2}\varepsilon\right) \tag{13}$$

where σ_ε, $C_{1\varepsilon}$ and $C_{\varepsilon2}$ are model tuning parameters adjusted to align with results from the LES simulations.

3.3. Reactive modeling

To model the reactive studies described in Section 2.4, a bulk reaction source term is included in the transport equation (Eq. (9)). This reaction term is modeled, consistent with previous studies in the literature [42,43], as a second-order reaction:

$$r_b = (\Omega-1)k\alpha_{\mathrm{Ba^{2+}}}\alpha_{\mathrm{SO_4^{2-}}} \tag{14}$$

here $\alpha_{\mathrm{Ba^{2+}}}$ and $\alpha_{\mathrm{SO_4{}^{2-}}}$ are the activities of barium and sulfate, respectively. The activities are the product of the concentration and the activity coefficient, i.e., $\alpha = c\gamma$, where γ is the activity coefficient. The activity coefficients are modeled using an implementation of the Pitzer model [44], k is the rate constant of the bulk precipitation, and Ω the saturation state is related to the equilibrium constant of BaSO4 $K_{\mathrm{BaSO_4}}$ by

$$\Omega = \frac{\alpha_{\mathrm{Ba^{2+}}}\alpha_{\mathrm{SO_4{}^{2-}}}}{K_{\mathrm{BaSO_4}}} \tag{15}$$

$K_{\mathrm{BaSO_4}}$ is set to $10^{-9.87}$ [45]; k is obtained from a second order polynomial:

$$k = c_1\Omega^2+c_2\Omega \tag{16}$$

where the coefficients $c_1 = 1.03\times10^{-4}\ \mathrm{mol^{-1}s^{-1}kg}$ and $c_2 = 8.22\times10^{-3}\ \mathrm{mol^{-1}s^{-1}kg}$ are fitted from batch experimental data, including those reported by Zhen-Wu et al. [46].

Additionally, to account for surface deposition, a wall reaction rate source term is implemented as a boundary flux in the transport equation (Eq. (9)). The reaction has the same second-order form as the bulk reaction, except for the rate constant, k_w, which was set to 1 m/s.

$$r_w = (\Omega-1)k_w\alpha_{\mathrm{Ba^{2+}}}\alpha_{\mathrm{SO_4{}^{2-}}} \tag{17}$$

3.4. Turbulent mixing

Dissolved species are transported in the fluid through both advection and diffusion. Microscale turbulent fluctuations lead to an additional eddy diffusion flux term $\boldsymbol{j} = \overline{\boldsymbol{u}'c'}$ on the macroscale. Also, these turbulent fluctuations diffuse momentum through the Reynolds stresses. In anisotropic turbulence, this additional diffusive term is not uniform across the three Cartesian directions.

The quantities $\overline{\boldsymbol{u}'\boldsymbol{u}'}$ and $\overline{\boldsymbol{u}'c'}$ are statistically gathered from the LES simulations along with computation of k_t and ε. The RSM simulations solve for the Reynolds stresses, whereas the $\boldsymbol{j}$ is approximated using GGDH [41]. GGDH assumes the $\boldsymbol{j}$ proportional to $\boldsymbol{R}$ through the turbulent Schmidt number, Sc_t:

$$\boldsymbol{j} = \overline{\boldsymbol{u}'c'} \approx \frac{C_s}{\mathrm{Sc}_t}\frac{k_t}{\varepsilon}\boldsymbol{R}\cdot\nabla\overline{c} \tag{18}$$

To estimate the Sc_t for the RSM simulations, using the turbulent statistics from the LES simulations, the divergence of the left and right-hand side vectors is used to calculate a local quantity that is then averaged over the fluid volume to establish a global Sc_t:

$$\mathrm{Sc}_t \approx C_s\frac{k_t}{\varepsilon}\frac{\nabla\cdot(\boldsymbol{R}\cdot\nabla\overline{c})}{\nabla\cdot\boldsymbol{j}} \tag{19}$$

From Eq. (9), we define a cell-local Damköhler number based on the species fluxes and reaction rate:

$$\mathrm{Da} = \frac{\text{Reaction Rate}}{\text{Transport Rate}} = \frac{r_b}{\nabla\cdot(D\nabla\overline{c}+\boldsymbol{j})-\overline{\boldsymbol{u}}\cdot\nabla\overline{c}} \tag{20}$$

To quantify the effect of turbulence, a normalized Damköhler number ($\widehat{\mathrm{Da}}_t$) is introduced as the ratio of the laminar Da ($\boldsymbol{j} = 0$) to the local advective Da:

$$\widehat{\mathrm{Da}} = \frac{\mathrm{Da}}{\mathrm{Da}_{\mathrm{laminar}}} = \left(1+\frac{\nabla\cdot\boldsymbol{j}}{\nabla\cdot(D\nabla\overline{c})-\overline{\boldsymbol{u}}\cdot\nabla\overline{c}}\right)^{-1} \tag{21}$$

This definition gives a number that tends to 1 at laminar flow where the mixing is limited by diffusion and tends to 0 in a perfectly mixed flow where the reaction rate is the limiting term.

To extract the diffusive effect of turbulence, the ratio of the turbulent diffusion flux to the molecular diffusivity can be defined as a turbulent

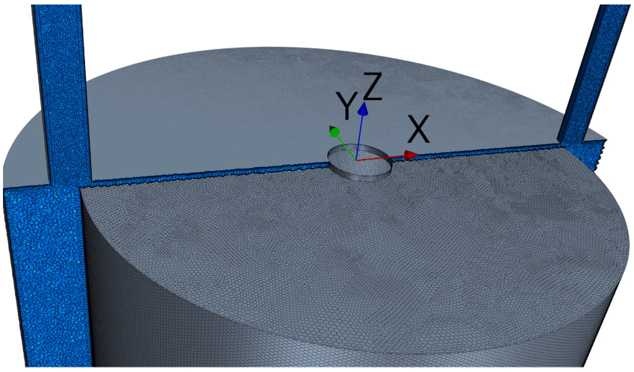

Fig. 3. Illustration of the computational domain clipping the fluid at $Y = 0$m. Mesh size $\widehat{\delta} = 0.05$.

Peclét number:

$$\mathrm{Pe}_t = \frac{\text{Turbulent Advection}}{\text{Molecular Diffusion}} = \frac{\nabla\cdot\boldsymbol{j}}{\nabla\cdot(D\nabla\bar{c})} \tag{22}$$

This turbulent Peclét number is a statistical consequence of Reynolds averaging. It describes the relative increase in mixing from turbulence. A more thorough derivation and explanation is included in the Supplementary file.

4. Results and discussions

A computational domain corresponding to the TC reactor is used to model the experimental setup. The domain is discretized with a mesh grid using a normalized base size $\widehat{\delta} = \delta/(r_2 - r_1)$ and a wall-resolving set of 10 prism layers ensuring the wall y^+ values below one. To further define the mesh, STAR-CCM+ controls of maximum 10° curvature per surface cell and a cell-to-cell maximum volume growth rate of 1.2 were set. Fig. 3 shows an illustration of the computational domain and the mesh grid at $\widehat{\delta} = 0.05$. The model is run using a second-order implicit time integration with time-steps ensuring a convective Courant number

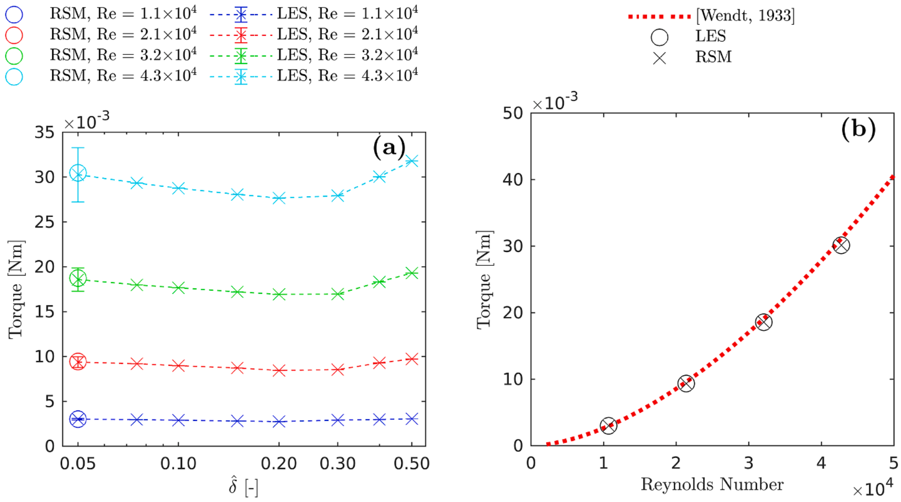

Fig. 4. Validation of the numerical model against an empirical correlation by Wendt [20] for torque scaling. (a) Mesh convergence studies performed for Reynolds numbers using the torque as a metric and Richardson extrapolation-based GCI as a measure of the numerical uncertainty at the finest grid. (b) Simulated torques for the finest mesh size compared to empirical results.

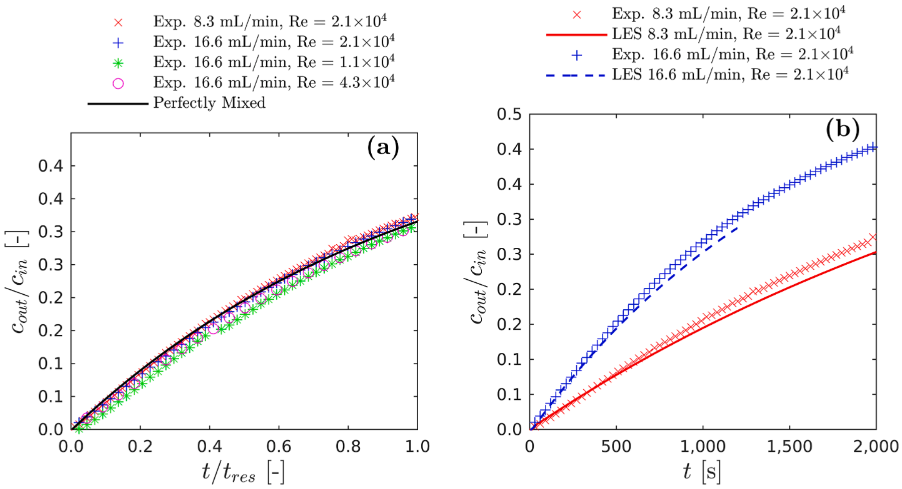

Fig. 5. Effluent concentrations (c_{out}) normalized by the inlet concentration (c_{in}). (a) Experimental data at four different experimental conditions along with the analytical expression for a perfectly mixed CSTR ($c_{out} = c_r$). (b) A comparison of experimental data and LES simulations.

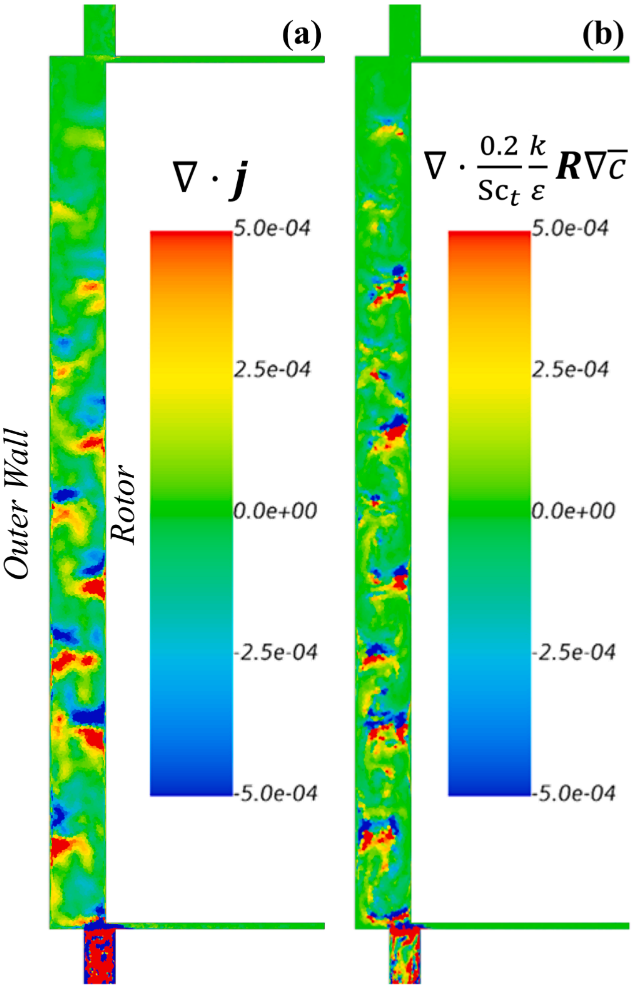

Fig. 6. Comparison of (a) time-averaged LES obtained and (b) RSM fitted turbulent diffusive flux at Re = 4.3 × 10^4.

below one. A Cartesian coordinate system with Z-axis aligned with the rotation axis and the XZ-plane aligned with the inlets is used to describe the results in this section. Simulations are carried out at rotational rates of 250, 500, 750, and 1000 RPM, corresponding to Reynolds numbers of 1.1 × 10^4, 2.1 × 10^4, 3.2 × 10^4, and 4.3 × 10^4, respectively. The inlets were defined numerically using fixed laminar uniform inlet velocities and concentrations and the outlets were defined by a uniform reference pressure.

4.1. *Validation of numerical models*

To ensure time step and grid size independence, convergence studies are carried out at each of the four Reynolds numbers. We investigated eight mesh sizes for every convergence study using Richardson extrapolation [47–49] to estimate the grid convergence index (GCI) as a measure of the uncertainty at the finest mesh size. The results of these studies are presented in Fig. 4a. The converged LES simulation results are validated against the empirical torques obtained from correlations by Wendt [20]. Fig. 4b shows the comparison of the torque measured on the vertical surface of the rotor (excluding the top and bottom) with the correlation.

From the LES torque simulations, statistics on the Reynolds stresses, $\overline{\boldsymbol{u}'\boldsymbol{u}'}$, are sampled over a duration of 10 revolutions after a steady-state has been reached. The obtained Reynolds stresses are compared to those produced from the RSM model, and the coefficients in Eq. (12) and (13) are adjusted to achieve better agreement. The torques obtained by the tuned RSM model are included in Fig. 4a and Fig. 4b and they show a good agreement. The adjusted parameters from Eq (12) and (13) are $C_{1\varepsilon} = 1.44$, $C_{2\varepsilon} = 2.4$, $C_S = 0.21$.

Mixing experiments (as described in Section 2.3) are then used to evaluate the ability of the numerical model to capture the transport of chemical species through the reactor. Effluent sulfate concentrations c_{out}, normalized by the injected concentrations c_{in} for the four studies are shown in Fig. 5a. The effluent concentrations are compared with the analytical expression for the temporal changes in concentration, c_r, in a well-mixed continuous stirred-tank (CSTR) reactor:

$$c_r = 0.5c_{in}\left(1 - e^{-t/t_{res}}\right) \tag{23}$$

Results shown in Fig. 5a suggest that at the four experimental conditions investigated, the TC reactor can be modeled as well-mixed. Two sets of experimental data at Re = 2.1 × 10^4, but at two injection flow rates, are compared to simulation outputs (Fig. 5b). In both cases, the LES simulations predict a slightly lower degree of mixing compared to experimental data.

The LES simulations with brine injection are carried out for $0.5t_{res}$ (t_{res} is the residence time of fluid in the reactor – a ratio of the reactor volume to the total volumetric flow rate) to ensure sufficient concentration throughout the reactor for the gathering of statistics on the contribution from microscale fluctuation on macroscale mixing. These statistics on $\overline{\boldsymbol{u}}$, $\overline{c}$ and $\overline{\boldsymbol{u}'c'}$ are sampled over a duration of 10 revolutions and used to estimate the best fitting turbulent Schmidt number based on GGDH assumptions from Eq. (18). At Re = 2.1 × 10^4 this yields Sc_t = 0.66 whereas at Re = 4.3 × 10^4 the fit yields Sc_t = 0.97, in good agreement with similar studies [30,35]. Fig. 6 compares the fitted GGDH diffusive flux with the gathered LES fluxes at Re = 4.3 × 10^4. In general, the trends are captured by the model, but the local variations are not accurately described. This is similar to the observations by da Silva et al. [35].

4.2. *Flow properties*

Based on the validated flow model, some general insights on the flow properties of the TC reactor are analyzed. The mean XZ-plane velocity profiles for the Re = 4.3 × 10^4 study are presented in Fig. 7a. As expected, the characteristic Taylor vortices are observed. Due to these vortices, the radial flow alternate in direction. This gives a significant advection between the rotor and stator. As these vortices also create almost closed flow structures, recirculation of fluid is high and thereby it can be expected that there is a significant jump in the concentrations of advected species between each closed vortex ring. The advective transport of the dissolved species in the radial direction is illustrated in Fig. 8c, where when comparing with the instantaneous velocity field in Fig. 8b and the mean velocity field in Fig. 8a, the significance of including the effect of the velocity field fluctuations can be seen as the smaller eddies transport fluid in directions varying from the mean flow direction. The instantaneous axial velocities, shown in Fig. 9, illustrate the significant increase in the magnitude and complexity of the secondary flow as the Reynolds number increases [50].

From analyzing the Reynolds stresses (see Fig. 7c and Fig. 7d), it is clear that the turbulence is anisotropic, emphasizing the importance of an RSM model for the correct resolution of the Reynolds stresses and consequently the turbulent advection.

The primary fluid motion is a shear flow between the moving inner wall and the stationary outer wall. As the secondary flow (Taylor vortices) transports fluid to the outer wall, the fluid adjacent to the wall accelerated. This can be illustrated through the fluid kinetic energy (see Fig. 7b). This speedup and the slow-down where the fluid is transported to and from the wall affects the shear rates and pressure on the wall. The obtained pressure and shear forces for Re = 4.3 × 10^4 are shown in Fig. 10a and Fig. 10b. The rings stand out clearly as regions of higher shear stress and pressure where the radial velocity is positive outwards

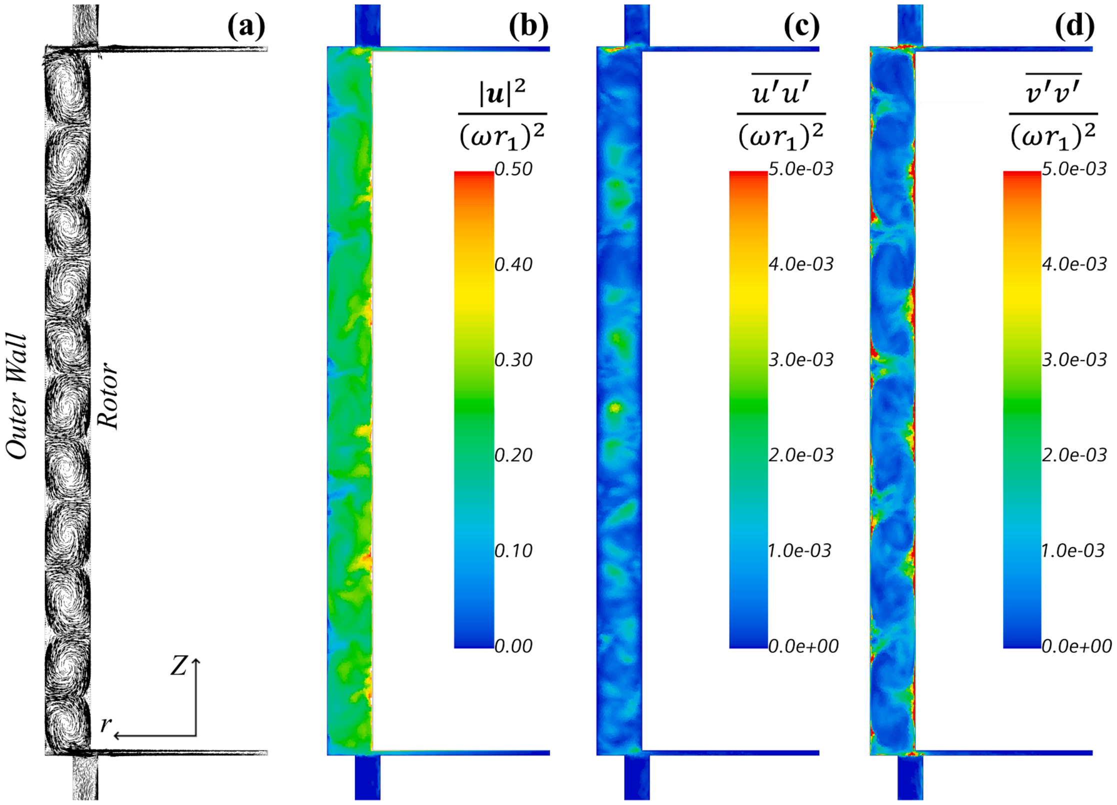

Fig. 7. Flow visualizations of the XZ plane (LES at Re = 4.3 × 10^4). (a) mean velocities showing the Taylor vortices, (b) fluid kinetic energy, (c) Reynolds stress component in the radial direction, (d) Reynolds stress component in the tangential direction.

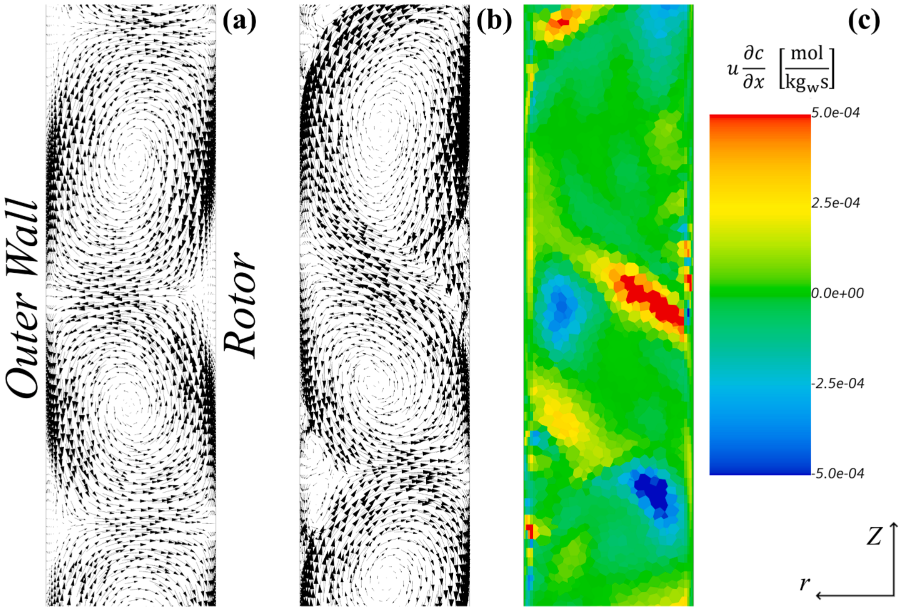

Fig. 8. Fluid transport at Re = 4.3 × 10^4. (a) time-averaged velocity (b) and instantaneous velocity (c) radial component of the advective term of the transport equation (Eq. (9)). The positive (red) transport direction is towards the outer wall.

towards the stator, oppositely as the velocity returns towards the rotor. The absolute shear stresses for each of the four Reynolds numbers are presented in Fig. 10b, as a function of the Z-coordinate.

4.3. Turbulent reactive studies

The formation of barium sulfate is tracked by monitoring concentrations of barium in the effluent, i.e., c_{out}. We define reactant conversion X as

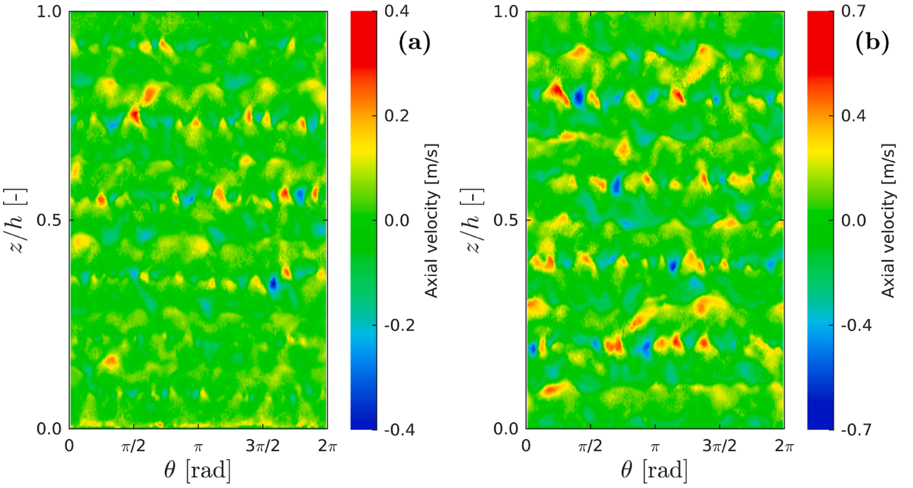

Fig. 9. LES axial velocity contours as a function of the tangential and axial direction in the center of the gap, $r = 0.5(r_1 + r_2)$. (a) Re $= 2.1 \times 10^4$, (b) Re $= 4.3 \times 10^4$.

$$X = \frac{c_r - c_{out}}{c_r} \tag{24}$$

here, c_r previously defined in Eq. (23), is the expected concentration of barium in the reactor in the absence of chemical reactions. From Eq. (23), $c_r = 0.5c_{in}$ as $t \to \infty$.

The instantaneous reactant conversions at the two turbulent flow conditions investigated in this study are shown in Fig. 11. Two key observations can be made from the figure. Firstly, in both systems, we observe a continuous depletion in reactant concentrations typical of chemically reactive systems. Secondly, a faster overall reaction rate is observed at Re $= 4.3 \times 10^4$ as indicated by higher conversions. This increased reaction rate at a more turbulent regime suggests that the system of interest, even under turbulent conditions (at Re $= 2.1 \times 10^4$), is transport-limited, that is, Da > 1.

A previous study of the deposition of $BaSO_4$ on surfaces – at Re and shear rates comparable to this study – reported a continuous increase at more turbulent flow conditions [51]. A similar finding has also been reported in other studies [52,53]. However, Yan et al. [8] reported no differences in barium sulfate precipitation kinetics as a function of Reynolds number. Increased turbulence in TC flows has also been associated with changes in crystal sizes and morphologies [7,8,16]. Here, we focus on the insights generated by the validated RSM model to explore potential interactions between fluid dynamics and reaction kinetics.

The turbulent Peclét numbers for the two reactive studies are presented in Fig. 12a and Fig. 12b. The volumetric-averaged values are included in Table 3. Two key points can be made. Firstly, in both turbulent flows, the diffusion of species due to turbulent advection is several orders of magnitude higher than the molecular diffusivity. It is also worth mentioning that there will remain a thin viscous sublayer near the surface in which the flow is laminar and therefore with a zero turbulent Peclét number. Secondly, doubling the Reynolds number yielded a 29% increase in the average turbulent Peclét number, from 1.94×10^4 to 2.51×10^4. This demonstrates that in the bulk fluid, turbulent mixing is dominant. This implies a significant increase in the effective diffusivity of the reactants and thus a lower effective Damköhler number. The calculated volumetric averages of the cell-local Damköhler numbers, from Eq. (20), show a reduction from 8.44×10^2 to 1.29×10^2 (see Table 3).

We implemented a simplified numerical reaction model to investigate how the increase in turbulent transport affects global reaction rates. These simulations were carried out using the validated RSM model. In the simulations, we assumed a 1:1 volumetric ratio of each brine in the reactor in order to obtain a high saturation state($\Omega = 1096$) where Da $\gg$ 1; in the current experimental setup, this occurs at $t/t_{res} > 4.3$. These simulations were run for a short time, approximately 60 s of simulated physical time. Fig. 12c and Fig. 12d show the local saturation state distribution after these short simulations, normalized with the fluid-volume averaged saturation state measured at the same instance (1035 for Re $= 2.1 \times 10^4$ and 1034 for the Re $= 4.3 \times 10^4$). Reactant conversions obtained from these simulations show a 1.03% and 2.15% for Re $= 2.1 \times 10^4$ and Re $= 4.3 \times 10^4$, respectively. These results are in qualitative agreement with experimental data.

The simple reaction models applied in this work do not comprehensively account for the complex interplay of the different mechanistic processes – including nucleation, growth, adhesion, deposition, and removal – involved in the overall formation of barium sulfate. As recently discussed by Wojtas et al. [54], there is a preponderance of kinetics models describing barium sulfate precipitation in the literature from studies covering a wide range of experimental conditions. A systematic review of these models is beyond the scope of this study.

Nevertheless, the simulation results demonstrate the role of transport in a chemically reactive system. Furthermore, simulation results are consistent with several studies in the literature and follow the same trend as observed in experiments. Finally, the systematic approach described in this work presents a basis for further incorporation of more comprehensive reactive models. This will be the focus of our next study.

While the simulations had only run for a short while, the significance of the vortex flow structure is evident. Within each vortex ring, the alternation of the direction of the radial component of the velocity will control how the bulk concentration is advected to the surface. Vortex pairs could also act as individual reactors by confining reactants within each ring for some time [55]. Further, the vortex patterns also give a distinct pattern to the surface forces (Fig. 10), which could affect near-surface reactions. Changes in the Ω/Ω_b near the surface, due to micro-scale fluctuations, suggest that near-surface reactions will be more strongly affected by turbulent transport compared to reactions in the bulk fluid.

In summary, the distinct patterns of the TC flow are likely to play a significant role in reactions occurring in both the bulk and surface phases. In systems where Da $\gg$ 1, the influence of the flow properties discussed in this work will play a major role. Thus, quantifying the effect of transport parameters on measured reaction rates will provide clearer insights into flow-kinetic interactions.

5. Conclusion

We investigated the impacts of turbulence in reactive processes by combining experiments and numerical simulations. Experimental

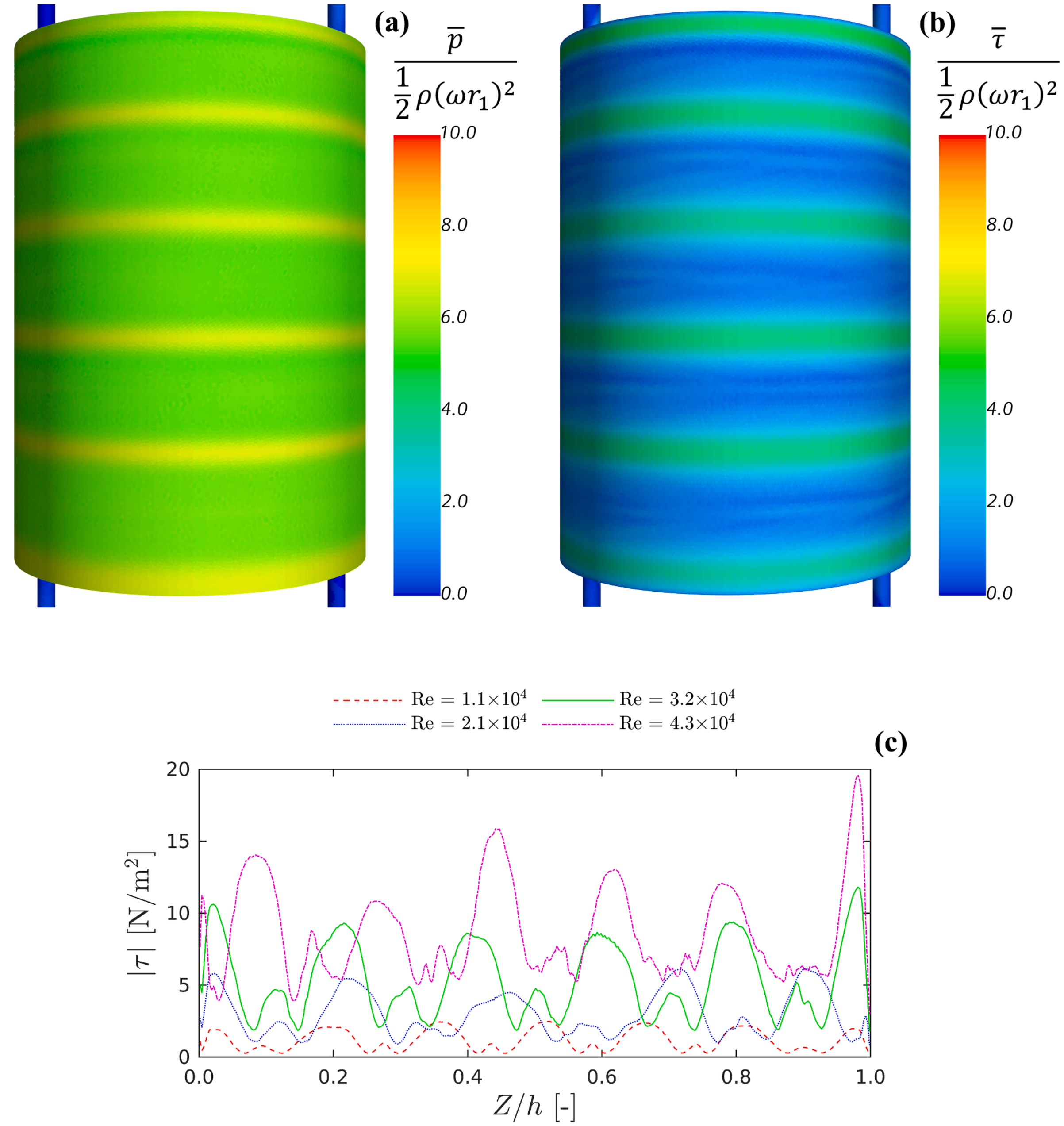

Fig. 10. Surface forces extracted from LES simulations. (a) Mean surface normal pressure on the stator at Re = 2.1 × 10^4. (b) Mean shear stress magnitude on the stator at Re = 2.1 × 10^4. (c) Azimuthally and time-averaged shear stress as a function of the axial position at four different Reynolds numbers.

studies were conducted in a Taylor-Couette reactor at turbulent conditions ($\text{Re} \geq 1.1 \times 10^4$). CFD simulations combining LES and RSM models were used to resolve local turbulence Reynolds stresses and turbulent transport at conditions comparable to experiments. We first validated our simulations against a previously published empirical torque model. Mixing studies were conducted in the TC cell at two flow rates and three rotational speeds. The ability of the model to capture the advection and diffusion of chemical species was successfully evaluated by comparing experimental data to simulation outputs. The validated models were then used to extract flow information relevant to turbulent transport across the cell. The direct applicability of the fitted parameters presented in this study will depend on the flow properties under consideration.

Turbulent precipitation studies were carried out at two Reynolds numbers. Effluent analyses showed an increased overall reaction rate at the more turbulent condition, this suggests a transport-limited reactive system ($\text{Da} \gg 1$). We coupled transport conditions to reaction kinetics to reveal the impacts of turbulence on the overall reaction rates. By defining the local turbulent Peclét number as the ratio of the turbulent advective fluxes to the molecular diffusive fluxes, the additional mixing from increased turbulence was quantified.

These ratios were four orders of magnitude and confirm that in the bulk fluid, diffusive transport is governed by turbulence. A 29% increase of the fluid volume-average turbulent Peclét number was seen from Re = 2.1 × 10^4 to Re = 4.3 × 10^4. This significantly decreased the Damköhler number. These analyses align with an experimentally measured increase in conversion of approximately 5%. Reactive simulation outputs suggest that the measured increase in reaction rates could be attributed to the increase in turbulent mixing.

Our study presents a systematic framework for the decoupling of

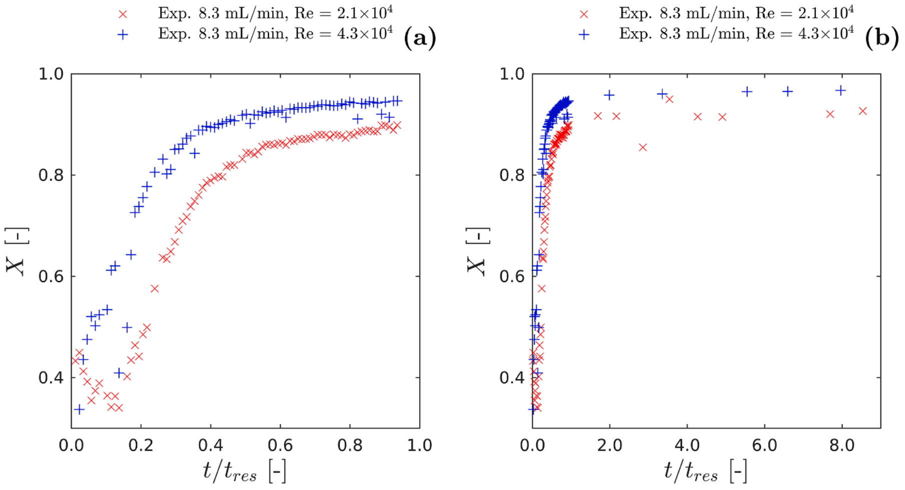

Fig. 11. Reactant conversions at two turbulent conditions. (a) Early experimental period highlighted. (b) Full experimental spectrum.

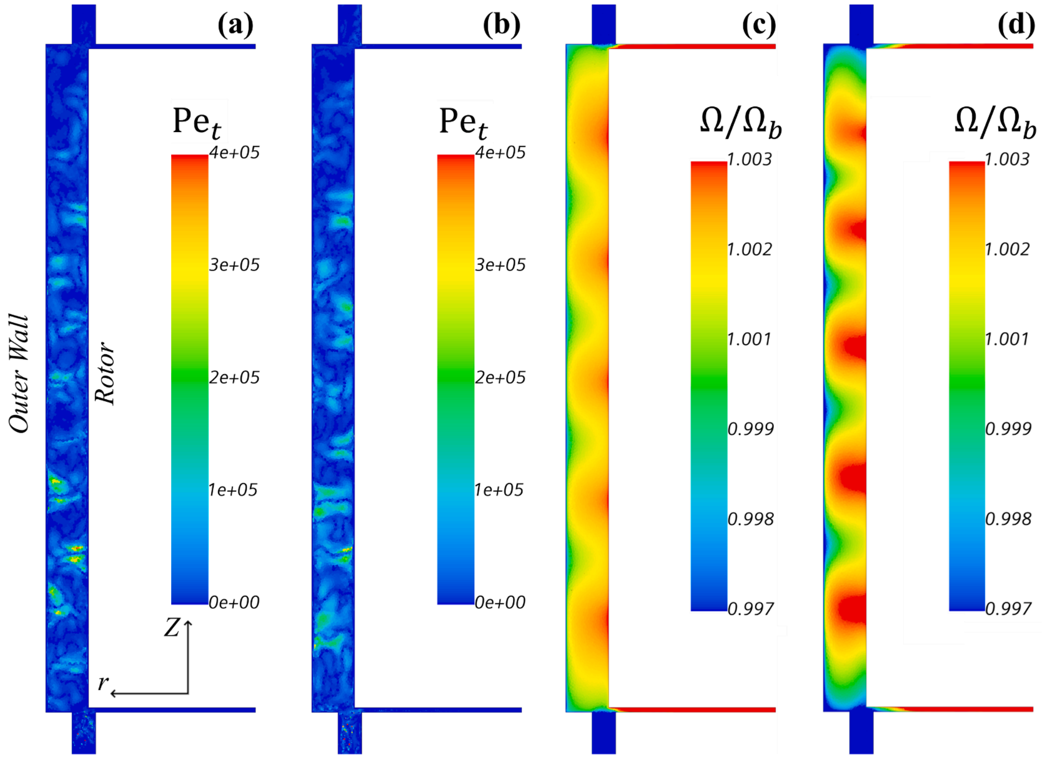

Fig. 12. Turbulent Peclét numbers from LES simulations. (a) Re = 2.1×10^4, (b) Re = 4.3×10^4. Saturation state normalized with reactor average saturation state (Ω_b) for RSM reactive $BaSO_4$ simulations at (c) Re = 2.1×10^4, (d) Re = 4.3×10^4. The reactor average Ω used for normalizing were 1035 for the Re = 2.1×10^4 study and 1034 for the Re = 4.3×10^4 study.

Table 3
Data from experiments and simulations at two Reynolds numbers. Pe_t was calculated as the volumetric average of the definition from Eq.(22), and Da is calculated as the volumetric average of the definition from Eq. (20). Average reactant conversion X_{ave} reported at $t/t_{res} > 4.3$.

		Experiments	Simulations	Simulations
Study	Re	X_{ave}	Pe_t	Da
1	2.1×10^4	0.92	1.94×10^4	8.44×10^2
2	4.3×10^4	0.97	2.51×10^4	1.29×10^2
Ratio (2:1)	2.0	1.05	1.29	0.15

transport phenomena from overall reaction rates in a turbulent system. We demonstrated the effect of anisotropic turbulence in liquid-phase flows using a validated RANS RSM model. We have shown that fluid transport properties play an important role in the net reaction kinetics and it is likely an explanation for some of the discrepancies in the literature. Future studies will explore the complex mechanistic processes involved in the nucleation, growth, and surface reactions of sparingly soluble salts such as barium sulfate.

Declaration of Competing Interest

The authors declare that they have no known competing financial interests or personal relationships that could have appeared to influence the work reported in this paper.

Acknowledgments

The authors kindly acknowledge the Danish Underground Consortium (Total E&P Denmark, Noreco & Nordsøfonden). This research has received funding from the Danish Hydrocarbon Research and Technology Centre (DHRTC) under the CTR2 program. We also thank Professor D. Eskin for helpful discussions and Annette E. Jensen for assisting with effluent analysis.

Appendix A. Supplementary data

Supplementary data to this article can be found online at https://doi.org/10.1016/j.cej.2021.129591.

References

[1] L.K. Hjertager, B.H. Hjertager, T. Solberg, CFD modeling of fast chemical reactions in turbulent liquid flows, Comput. Aided Chem. Eng. 9 (2001) 159–164, https://doi.org/10.1016/S1570-7946(01)80022-5.

[2] M. Rizzotto, F. Florit, R. Rota, V. Busini, A CFD hybrid approach to simulate liquid-phase chemical reactors, Chem. Eng. J. 377 (2019) 120365, https://doi.org/10.1016/j.cej.2018.11.063.

[3] R.J. Donnelly, Taylor-Couette flow: The early days, Phys. Today 44 (11) (1991) 32–39, https://doi.org/10.1063/1.881296.

[4] G.S. Lewis, H.L. Swinney, Velocity structure functions, scaling, and transitions in high-Reynolds-number Couette-Taylor flow, Phys. Rev. E 59 (5) (1999) 5457–5467, https://doi.org/10.1103/PhysRevE.59.5457.

[5] M.A. Fardin, C. Perge, N. Taberlet, "The hydrogen atom of fluid dynamics" – introduction to the Taylor–Couette flow for soft matter scientists, Soft Matter 10 (20) (2014) 3523, https://doi.org/10.1039/c3sm52828f.

[6] A. Mallock, IV. Determination of the viscosity of water, Proc. R. Soc. London 45 (1889) 126–132, https://doi.org/10.1098/rspl.1888.0081.

[7] B. Judat, A. Racina, M. Kind, Macro- and micromixing in a Taylor-Couette reactor with axial flow and their influence on the precipitation of barium sulfate, Chem. Eng. Technol. 27 (3) (2004) 287–292, https://doi.org/10.1002/ceat.200401997.

[8] F. Yan, Z. Dai, G. Ruan, H. Alsaiari, N. Bhandari, F. Zhang, Y. Liu, Z. Zhang, A. Kan, M. Tomson, Barite scale formation and inhibition in laminar and turbulent flow: A rotating cylinder approach, J. Petrol. Sci. Eng. 149 (2017) 183–192, https://doi.org/10.1016/j.petrol.2016.10.030.

[9] K. Akbarzadeh, M. Zougari, Introduction to a Novel Approach for Modeling Wax Deposition in Fluid Flows. 1. Taylor−Couette System, Ind. Eng. Chem. Res. 47 (3) (2008) 953–963, https://doi.org/10.1021/ie0711325.

[10] D.L. Marchisio, A.A. Barresi, R.O. Fox, Simulation of turbulent precipitation in a semi-batch Taylor-Couette reactor using CFD, AIChE J. 47 (2001) 664–676. https://doi.org/10.1002/aic.690470314.

[11] C. Coufort, D. Bouyer, A. Liné, Flocculation related to local hydrodynamics in a Taylor–Couette reactor and in a jar, Chem. Eng. Sci. 60 (8-9) (2005) 2179–2192, https://doi.org/10.1016/j.ces.2004.10.038.

[12] N. Wilkinson, C.S. Dutcher, Taylor-Couette flow with radial fluid injection, Rev. Sci. Instrum. 88 (8) (2017) 083904, https://doi.org/10.1063/1.4997340.

[13] X. Wei, H. Takahashi, S. Sato, M. Nomura, Continuous emulsion polymerization of styrene in a single Couette-Taylor vortex flow reactor, J. Appl. Polym. Sci. 80 (11) (2001) 1931–1942, https://doi.org/10.1002/app.1291.

[14] W. Xue, K. Yoshikawa, A. Oshima, S. Sato, M. Nomura, Continuous emulsion polymerization of vinyl acetate. II Operation in a single Couette-Taylor vortex flow reactor using sodium lauryl sulfate as emulsifier, J. Appl. Polym. Sci. 86 (11) (2002) 2755–2762, https://doi.org/10.1002/app.11256.

[15] A.-T. Nguyen, T. Yu, W.-S. Kim, Couette-Taylor crystallizer: Effective control of crystal size distribution and recovery of l-lysine in cooling crystallization, J. Cryst. Growth 469 (2017) 65–77, https://doi.org/10.1016/j.jcrysgro.2016.10.020.

[16] S.H. Kang, S.G. Lee, W.M. Jung, M.C. Kim, W.-S. Kim, C.K. Choi, R.S. Feigelson, Effect of Taylor vortices on calcium carbonate crystallization by gas–liquid reaction, J. Cryst. Growth 254 (1-2) (2003) 196–205, https://doi.org/10.1016/S0022-0248(03)01152-7.

[17] D.P. Lathrop, J. Fineberg, H.L. Swinney, Transition to shear-driven turbulence in Couette-Taylor flow, Phys. Rev. A 46 (10) (1992) 6390–6405, https://doi.org/10.1103/PhysRevA.46.6390.

[18] R. Ostilla-Mónico, S.G. Huisman, T.J.G. Jannink, D.P.M. Van Gils, R. Verzicco, S. Grossmann, C. Sun, D. Lohse, Optimal Taylor-Couette flow: radius ratio dependence, J. Fluid Mech. 747 (2014) 1–29, https://doi.org/10.1017/jfm.2014.134.

[19] B.W. Thompson, J. Novak, M.C.T. Wilson, M.M. Britton, A.F. Taylor, Inward propagating chemical waves in Taylor vortices, Phys. Rev. E - Stat. Nonlinear, Soft Matter Phys. 81 (2010), https://doi.org/10.1103/PhysRevE.81.047101.

[20] F. Wendt, Turbulente Strömungen zwischen zwei rotierenden konaxialen Zylindern, Ing. Arch. 4 (6) (1933) 577–595, https://doi.org/10.1007/BF02084936.

[21] D. Eskin, An engineering model of a developed turbulent flow in a Couette device, Chem. Eng. Process. Process Intensif. 49 (2) (2010) 219–224, https://doi.org/10.1016/j.cep.2009.12.001.

[22] R.L. Panton, Scaling laws for the angular momentum of a completely turbulent Couette flow, Comptes Rendus l'Académie Des Sci. Série 2, Mécanique, Phys. Chim. Sci. l'univers, Sci. La Terre. 315 (1992) 1467–1473.

[23] D. Eskin, J. Ratulowski, K. Akbarzadeh, S. Pan, Modelling asphaltene deposition in turbulent pipeline flows, Can. J. Chem. Eng. 89 (3) (2011) 421–441, https://doi.org/10.1002/cjce:20507.

[24] D.C. Wilcox, Turbulence Modelling for CFD, DCW industries, La Canada, CA, 1993.

[25] G.K. Batchelor, Small-scale variation of convected quantities like temperature in turbulent fluid Part 1. General discussion and the case of small conductivity, J. Fluid Mech. 5 (1959) 113–133, https://doi.org/10.1017/S002211205900009X.

[26] Rémi Manceau, K. Hanjalić, Elliptic blending model: A new near-wall Reynolds-stress turbulence closure, Phys. Fluids 14 (2) (2002) 744–754, https://doi.org/10.1063/1.1432693.

[27] J.L. Lumley, Computational modeling of turbulent flows, Adv. Appl. Mech. (1979) 123–176, https://doi.org/10.1016/S0065-2156(08)70266-7.

[28] D.A. Lysenko, I.S. Ertesvåg, K.E. Rian, Numerical Simulations of the Sandia Flame D Using the Eddy Dissipation Concept, Flow Turbulence Combust 93 (4) (2014) 665–687, https://doi.org/10.1007/s10494-014-9561-5.

[29] M. Bösenhofer, E.-M. Wartha, C. Jordan, M. Harasek, The Eddy dissipation concept—analysis of different fine structure treatments for classical combustion, Energies 11 (2018) 1902, https://doi.org/10.3390/en11071902.

[30] C. Gualtieri, A. Angeloudis, F. Bombardelli, S. Jha, T. Stoesser, On the values for the turbulent schmidt number in environmental flows, Fluids. 2 (2017) 17, https://doi.org/10.3390/fluids2020017.

[31] C. Walker, A. Manera, B. Niceno, M. Simiano, H.-M. Prasser, Steady-state RANS-simulations of the mixing in a T-junction, Nucl. Eng. Des. 240 (9) (2010) 2107–2115, https://doi.org/10.1016/j.nucengdes.2010.05.056.

[32] B. Magnussen, On the structure of turbulence and a generalized eddy dissipation concept for chemical reaction in turbulent flow, American Institute of Aeronautics and Astronautics, St.Louis, Missouri, 1981 https://doi.org/10.2514/6.1981-42.

[33] R.O. Fox, The spectral relaxation model of the scalar dissipation rate in homogeneous turbulence, Phys. Fluids. 7 (1995) 1082–1094. https://doi.org/10.1063/1.868550.

[34] L. Wang, R.D. Vigil, R.O. Fox, CFD simulation of shear-induced aggregation and breakage in turbulent Taylor–Couette flow, J. Colloid Interface Sci. 285 (1) (2005) 167–178, https://doi.org/10.1016/j.jcis.2004.10.075.

[35] C.B. da Silva, J.C.F. Pereira, Analysis of the gradient-diffusion hypothesis in large-eddy simulations based on transport equations, Phys. Fluids. 19 (2007) 035106. https://doi.org/10.1063/1.2710284.

[36] B.E. Launder, On the Computation of Convective Heat Transfer in Complex Turbulent Flows, J. Heat Transfer. 110 (1988) 1112–1128. https://doi.org/10.1115/1.3250614.

[37] G. Bergeles, A.D. Gosman, B.E. Launder, The Turbulent Jet in a Cross Stream at Low Injection Rates: A Three-Dimensional Numerical Treatment, Numer. Heat Transf. Part B Fundam. 1 (1978) 217–242. https://doi.org/10.1080/10407797809414307.

[38] T. Kajishima, K. Taira, Numerical Simulation of Fluid Flows, in: Comput. Fluid Dyn., Springer International Publishing, Cham, 2017: pp. 1–22. https://doi.org/10.1007/978-3-319-45304-0_1.

[39] W.M. Haynes, D.R. Lide, T.J. Bruno, eds., CRC Handbook of Chemistry and Physics, CRC Press, 2016. https://doi.org/10.1201/9781315380476.

[40] F. Nicoud, F. Ducros, Subgrid-scale stress modelling based on the square of the velocity gradient tensor, flow, Turbul. Combust. 62 (1999) 183–200, https://doi.org/10.1023/A:1009995426001.

[41] B.J. Daly, Transport equations in turbulence, Phys. Fluids 13 (11) (1970) 2634, https://doi.org/10.1063/1.1692845.

[42] G.H. Nancollas, M.M. Reddy, The Kinetics of Crystallization of Scale-Forming Minerals, Soc. Pet. Eng. J. 14 (1974) 117–126. https://doi.org/10.2118/4360-PA.

[43] A.G. Christy, A. Putnis, The kinetics of barite dissolution and precipitation in water and sodium chloride brines at 44–85°C, Geochim. Cosmochim. Acta 57 (10) (1993) 2161–2168, https://doi.org/10.1016/0016-7037(93)90557-D.

[44] K.S. Pitzer, Thermodynamics of electrolytes. I. Theoretical basis and general equations, J. Phys. Chem. 77 (2) (1973) 268–277, https://doi.org/10.1021/j100621a026.

[45] C.A.J. Appelo, Principles, caveats and improvements in databases for calculating hydrogeochemical reactions in saline waters from 0 to 200 °C and 1 to 1000 atm, Appl. Geochem. 55 (2015) 62–71, https://doi.org/10.1016/j.apgeochem.2014.11.007.

[46] B.Y. Zhen-Wu, K. Dideriksen, J. Olsson, P.J. Raahauge, S.L.S. Stipp, E.H. Oelkers, Experimental determination of barite dissolution and precipitation rates as a function of temperature and aqueous fluid composition, Geochim. Cosmochim. Acta 194 (2016) 193–210, https://doi.org/10.1016/j.gca.2016.08.041.

[47] L.F. Richardson, IX. The approximate arithmetical solution by finite differences of physical problems involving differential equations, with an application to the stresses in a masonry dam, Philos. Trans. R. Soc. London. Ser. A, Contain. Pap. a Math. or Phys. Character. 210 (1911) 307–357. https://doi.org/10.1098/rsta.1911.0009.

[48] L.F. Richardson, VIII. The deferred approach to the limit, Philos. Trans. R. Soc. London. Ser. A, Contain. Pap. a Math. or Phys. Character. 226 (1927) 299–361. https://doi.org/10.1098/rsta.1927.0008.

[49] I.B. Celik, U. Ghia, P.J. Roache, C.J. Freitas, H. Coleman, P.E. Raad, Procedure for estimation and reporting of uncertainty due to discretization in CFD applications, J. Fluids Eng. 130 (2008), 078001, https://doi.org/10.1115/1.2960953.

[50] T. Chen, P. Chen, H. Montgomerie, T. Hagen, R. Benvie, Q. Guo, U. Anyanwu, B. Xu, X. Yang, Do we need higher dose scale inhibitors to inhibit scale under turbulent conditions? Insight into mechanisms and new test methodology, SPE Int. Oilf. Scale Conf. Exhib., Society of Petroleum Engineers (2014), https://doi.org/10.2118/169780-MS.

[51] A. Quddus, I.M. Allam, BaSO4 scale deposition on stainless steel, Desalination 127 (3) (2000) 219–224, https://doi.org/10.1016/S0011-9164(00)00012-6.

[52] M.M. Vazirian, T.V.J. Charpentier, Mônica de Oliveira Penna, A. Neville, Surface inorganic scale formation in oil and gas industry: As adhesion and deposition processes, J. Petrol. Sci. Eng. 137 (2016) 22–32, https://doi.org/10.1016/j.petrol.2015.11.005.

[53] K. Wojtas, Łukasz Makowski, W. Orciuch, Barium sulfate precipitation in jet reactors: Large eddy simulations, kinetics study and design considerations, Chem. Eng. Res. Des. 158 (2020) 64–76, https://doi.org/10.1016/j.cherd.2020.03.019.

[54] D. Seo, W.-S. Kim, D.H. Kim, Numerical simulation of Taylor-Couette fluidic device for the exfoliation of two-dimensional materials, Chem. Eng. J. 399 (2020) 125726, https://doi.org/10.1016/j.cej.2020.125726.

4 Paper 3: Scale attachment and detachment: The role of hydrodynamics and surface morphology

Chemical Engineering Journal 430 (2022) 132583

Contents lists available at ScienceDirect

Chemical Engineering Journal

journal homepage: www.elsevier.com/locate/cej

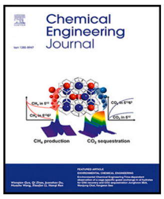

Scale attachment and detachment: The role of hydrodynamics and surface morphology

Isaac A. Løge [a,*], Jakob R. Bentzon [b], Christopher G. Klingaa [b], Jens H. Walther [b,c], Benaiah U. Anabaraonye [d], Philip L. Fosbøl [a]

[a] Department of Chemical Engineering, Technical University of Denmark, Kgs. Lyngby, 2800, Denmark
[b] Department of Mechanical Engineering, Technical University of Denmark, Kgs. Lyngby, 2800, Denmark
[c] Computational Science and Engineering Laboratory, ETH, Zürich CH-8092, Switzerland
[d] Danish Hydrocarbon Research and Technology Centre, Technical University of Denmark, Kgs. Lyngby, 2800, Denmark

ARTICLE INFO

Keywords:
Fouling mechanisms
Surface roughness
CFD
Crystallization fouling
Hydrodynamics

ABSTRACT

Crystallization fouling presents a significant challenge in a wide range of industries. Accurate understanding of crystal formation is crucial for planning preventative measures and maximizing the effectiveness of maintenance interventions. In this study, we demonstrate that understanding net deposition rates depends on the knowledge of the detachment mechanisms and deposition distribution characteristics. We quantify deposition in a once-through flow set-up and visualize crystal formation through high-resolution X-ray micro-computed tomography scanning. Additionally, we quantify the height distribution of deposited crystals through computed surface texture parameters. Finally, we use computational fluid dynamics, implementing large-eddy simulations turbulence modelling and Eulerian transport of chemical species, to describe bulk and wall reactions and quantify energy and mass transport in turbulent eddies. Results show that attachment and detachment processes depend on fluid hydrodynamics; the influx of material determines the overall deposition to the surface, while the deposition pattern is governed by the surface morphology of the initial surface morphology. Our findings provide a foundation for understanding fouling mechanisms and present a template for developing more accurate prediction models.

1. Introduction

Crystallization fouling, i.e., scaling, occurs due to the precipitation and subsequent adhesion of crystals on surfaces. The presence of scaling has a wide range of deleterious effects in several industries. Examples include increased production costs in water treatment processes [1–4], flow assurance challenges in the petroleum industry [5,6], sub-optimal performance of heat exchangers [7,8], and reduced energy transfers in for geothermal energy systems [9].

Effective scale prevention and removal strategies depend on an accurate understanding of the processes preceding surface adhesion [10,11]. Scale formation is a multi-step complex process involving nucleation, adhesion, and growth [12,13]. Chemical inhibitors that either slow nucleation kinetics or prevent crystal growth are widely used [14]. However, these can be detrimental to aquatic life [15]. Deposited crystals are either removed mechanically or through chemical means [16]. The ability to predict the magnitude and location of crystal formation is vital for the planning and managing of both chemical inhibition and removal interventions [17]. Therefore, accurate prediction models are critical.

Nucleation and crystal growth combined with hydrodynamics are complex processes to simulate accurately [18,19]. When modelling the rate of scale formation, two key approaches have been presented in the literature. In the first approach, kinetic rate laws for scale formation are proposed based solely on correlations between various process parameters and the measured deposition rate [20–23]. This approach primarily relies on fitting experimental data and does not account for the actual mechanisms at play. Due to the ease of implementation, this approach is widely used. The second approach explicitly accounts for the competition between adhesion and detachment rates on the net surface deposition rate [24,25]. Recently, a mathematical framework based on the second approach was presented [26,27]. Here an increase in flow was found to result in lower net deposition rates [27]. This is in agreement with the observation that detachment processes are considered correlated with the shear stress exerted by the fluid on

---

[*] Corresponding author.
E-mail address: isacl@kt.dtu.dk (I.A. Løge).

https://doi.org/10.1016/j.cej.2021.132583
Received 23 April 2021; Received in revised form 17 September 2021; Accepted 19 September 2021
Available online 7 October 2021
1385-8947/© 2021 The Authors. Published by Elsevier B.V. This is an open access article under the CC BY license (http://creativecommons.org/licenses/by/4.0/).

the surface [25]. However, due to the limited understanding of detachment mechanisms, accurate prediction of net scale deposition is challenging [28,29]. This is reflected in conflicting findings: Higher net deposition rates have been observed both in systems with increased [20,30,31] and decreased [26,27,32–34] fluid velocities and shear stresses. An increase in surface roughness has been reported to increase the scale formation rate [35,36], whereas other studies found weak or no correlation [30]. Surface texture has been reported to affect the morphology of the formed crystals [37,38]. Anti-scaling materials have been synthesized by engineering low energy surfaces [39].

In this study, we investigate the complex interplay between fluid flow and surface morphology on scale deposition. Two key experimental variables were studied: The fluid hydrodynamics – laminar and turbulent flow regimes – and surface morphology of the deposition cells — smooth and rough. The laminar flow domain represented a low material influx regime where the transport of material to the surface is diffusion-limited. In the turbulent flow regime, where there is a high material influx, the transport limitation was reduced and the effect of a fluid–wall coupling in a turbulent flow domain was illustrated. In addition, we investigated the interaction areas of engineered surfaces resembling that of production equipment at both the beginning (i.e., smooth) and at the end [40] (i.e., rough) of a life cycle. In this study, we engineered threaded surfaces to investigate the role of surface roughness. The key feature of the fluid–wall interaction is the effect of the transport as the boundary layers are affected by the modulation of the bulk turbulence by the surface profile.

We conducted experiments using a once-through flow set-up with a constant flow of $BaSO_4$ saturated brine through the reactor cell. The magnitude of crystal growth is quantified through gravimetric analysis. We use high-resolution X-ray micro-computed tomography (CT) scanning to visualize scale deposition. The surface texture parameters of the scaled deposition cells are quantified using a custom-written Python code [41].

We perform numerical simulations based on computational fluid dynamics (CFD) applying large eddy simulation (LES) turbulence modelling, and Eulerian transport of the chemical species. The CFD simulations are used to illustrate the effects of hydrodynamics on the transport of reacting species.

These cases are designed to explore and understand how detachment processes are flow-dependent. Based on these case studies, we demonstrate the importance of reintroducing an accurate description of the detachment processes to understand overall scale build-up.

2. Materials and method

2.1. Materials

Two brines were prepared: a 2.04 $\frac{\text{mmol}}{\text{kg H}_2\text{O}}$ Na_2SO_4 and a $BaCl_2$ solution with a concentration of 0.972 $\frac{\text{mmol}}{\text{kg H}_2\text{O}}$. Both solutions were prepared with de-ionized water (resistivity 18.2 MΩ cm) at ambient conditions.

2.2. The flow set-up

A custom flow set-up has been built (see Fig. 1), which allows for the investigation of crystal growth and deposition under single throughput flow conditions. Fluids were transported using Masterflex®peristaltic pumps, with an L/S High-Performance Pump Head. Temperature control was achieved with a thermostatic bath. All experiments were performed at a temperature of 60 °C. Mixing of brines was done in a T-piece with an outlet of a 1/8 inch diameter plastic tube which was 14.5 cm long. A custom-built deposition cell was introduced after the plastic line (see Fig. 1a) with the portion in contact with the mixed brine solution being made of steel and the other compartment made of aluminium. The cell outlet was connected to a 55.5 cm long, 1/8 inch diameter plastic tube going to a waste tank.

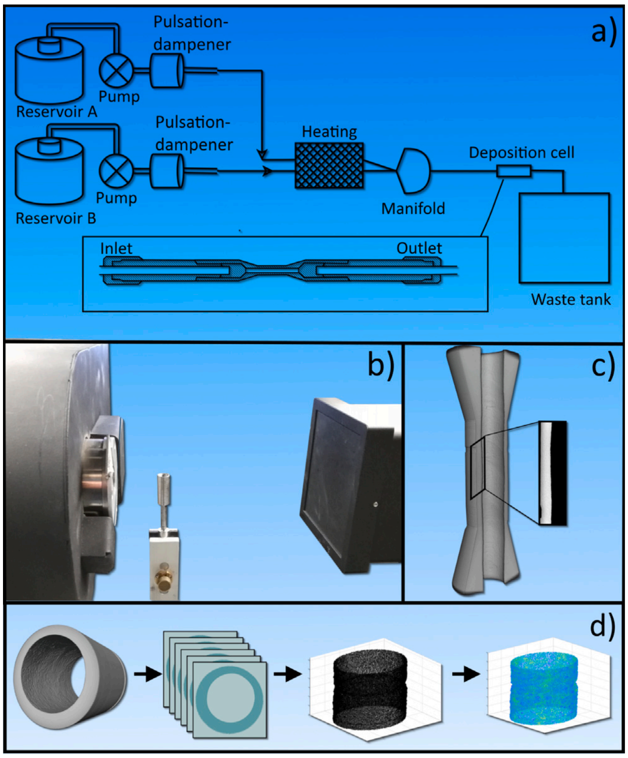

Fig. 1. Description of the workflow utilized in this work. Detailed descriptions of (a), (b) and (d) are found in Section 2.4, 2.5, and 2.7.

2.3. Fabrication of the deposition cell

The cells were sampled and lathed from a tube of X-52 steel. The surface finish of the cell was fabricated in two ways: One smooth and one threaded. The threaded surface was made using an ISO M3 × 0.5 thread cutting tap. The inner diameters of both cells were 3 mm. The nominal surface areas of the smooth and threaded cells were 2.83 cm^2 and 6.13 cm^2, respectively. The surface area, A, of the threaded cell was calculated as

$$A = 1.625\pi L D \tag{1}$$

where L is the length of the cell (3 cm), and D is the diameter of the cell in the threading valleys (0.4 cm).

2.4. The experimental procedure

We investigated the effect of the interplay between flow rate and surface morphology on scale deposition. The experimental conditions investigated can be found in Table 1. Before each experiment, upstream flow lines of the deposition cell were flushed with de-ionized water for a minimum of five minutes to ensure proper cleaning and no leaks. Each cell was weighed before and after deposition. After the mixing point, the cell and plastic lines were positioned in an upright manner, allowing the flow to stabilize and ensuring that no additional turbulence was introduced due to kinks in the tubing. The injected flow rates were 60 mL/min and 280 mL/min for the laminar and turbulent flow, respectively. Brines were injected at a 1:1 volumetric ratio. At the end of each experiment, the cell was rinsed with de-ionized water and placed in an oven to dry at 120 °C for four hours. To test the reproducibility of the experimental procedure, one of the turbulent experiments was repeated four times. This resulted in a relative standard deviation of 2.9% (see Supplementary Material).

Table 1
Experimental conditions investigated: t = experimental duration, Pa = arithmetic mean height, $VtHd$ = Valley to height distance, A = surface area.

Name	Re [-]	t [min]	Pa [μm]	$VtHd$ [mm]	A [cm^2]
[Laminar, smooth]	1080	30	6.44	0.0	2.83
[Laminar, smooth]	1080	90	7.26	0.0	2.83
[Laminar, smooth]	1080	180	5.26	0.0	2.83
[Laminar, threaded]	1080	30	5.86	0.5	6.13
[Laminar, threaded]	1080	90	5.83	0.5	6.13
[Laminar, threaded]	1080	180	7.09	0.5	6.13
[Turbulent, smooth]	4808	15	8.93	0.0	2.83
[Turbulent, smooth]	4808	30	7.46	0.0	2.83
[Turbulent, smooth]	4808	60	8.71	0.0	2.83
[Turbulent, threaded]	4808	15	8.02	0.5	6.13
[Turbulent, threaded]	4808	30	5.79	0.5	6.13
[Turbulent, threaded]	4808	60	8.74	0.5	6.13

2.5. CT scanning

CT scanning of the cells after the experiment was performed with a ZEISS XRadia 410 Versa. 995 projections were acquired per sample over 360° with a beam intensity of 120 kV, where each projection had an exposure time of 3–15 s and an objective of 4× was used. The total volume of the tomographies was 2.56 mm^3 and a voxel size of 4 μm. Furthermore, all cells were scanned with a field of view of 1069 mm^3, which was large enough to capture the whole cell in which deposition occurred. This was done to verify that the smaller segments of the cells, which were used for most of the analyses presented in this study, were representative of the whole cell.

2.6. Computational Fluid Dynamics

CFD modelling is carried out using the finite volume method implemented in STAR–CCM+ version 15.06. A CFD model is implemented with simplified reaction kinetics to provide insights into the effect of the hydrodynamics on the transport of the reactants. The CFD model is based on work performed in a recently published study [19]. The brine is assumed incompressible, and the influence of the solutes on the solvent density and viscosity was neglected. The temperature field is fixed isothermally to 60 °C. The fluid density is set to 983.2 kg/m^3 and the dynamic viscosity to 0.466×10^{-3} kg/(m s).

As all length and time scales are not resolved by the computational grid, spatial filtering using LES turbulence modelling was applied. This yields a generalized conservation equation of a conserved quantity ϕ:

$$\frac{\partial\overline{\phi}}{\partial t}+\frac{\partial\overline{u_i\phi}}{\partial x_i}-\frac{\partial}{\partial x_i}\mathcal{D}\frac{\partial\overline{\phi}}{\partial x_i}=\overline{S} \qquad (2)$$

where the indexing i follows tensor notation, the overbar denotes a spatially averaged quantity, $\mathcal{D}$ is the diffusivity of ϕ and S covers source terms. The model conserves mass ($\phi = \rho$), momentum ($\phi = \rho u_i$), and solute concentration ($\phi = m_s$) where u_i is the velocity vector, ρ the liquid density and m_s the molality of a given solute.

The Pitzer activity model [42] is implemented using an in-house developed C library to compute the saturation ratio (SR) of barium sulfate:

$$\mathrm{SR}=\frac{\alpha_{\mathrm{Ba}^{2+}}\alpha_{\mathrm{SO}_4^{2-}}}{K_{\mathrm{BaSO}_4}} \qquad (3)$$

Here $\alpha_{\mathrm{Ba}^{2+}}$ and $\alpha_{\mathrm{SO}_4^{2-}}$ are the activities of barium and sulphate. $\mathrm{K}_{\mathrm{BaSO}_4}$ is the equilibrium constant.

A reaction model is implemented in both the bulk and on the wall. The bulk reaction term is modelled as a second-order reaction:

$$r_{\mathrm{Ba}^{2+}}=r_{\mathrm{SO}_4^{2-}}=(\mathrm{SR}-1)k\alpha_{\mathrm{Ba}^{2+}}\alpha_{\mathrm{SO}_4^{2-}} \qquad (4)$$

Similar to the previously mentioned paper, [19], k is obtained from a second order polynomial fitting of batch experimental data combined with data from Zhen-Wu et al. [43]. Bulk precipitates are transported passively with the flow. No attachment mechanism is implemented. The surface reaction rate is implemented with a similar second order reaction, using a surface rate constant k_s set to 1m/s to calculate a boundary flux j:

$$j_{\mathrm{Ba}^{2+}}=j_{\mathrm{SO}_4^{2-}}=(\mathrm{SR}-1)k_s\alpha_{\mathrm{Ba}^{2+}}\alpha_{\mathrm{SO}_4^{2-}} \qquad (5)$$

The CFD model accounts for the deposition cell as well as the straight tubing attached on inlet and outlet. The fluid inlet is located 40 diameters of tubing upstream of the cell. The inlet conditions are modelled using a constant mass flow rate. The concentration of the inlet brine is assumed perfectly pre-mixed. The outlet is located 20 diameters of tubing downstream from the cell and is modelled using a fixed uniform atmospheric pressure. Fig. 2 illustrates the layout and dimensions of the threaded deposition cell used for the CFD model. All cell and tubing walls are modelled as no-slip walls. For the reactants the walls are modelled as sinks consuming a prescribed flux. The boundary fluxes are calculated in each boundary cell face for each time step solving Eq. (4). The actual deposition of the material is not modelled, i.e. no changes in solid geometry is implemented. The induction time for scaling under the experimental conditions investigated was calculated based on classical nucleation theory [44], and on literature parameters [45,46]. The calculated induction time was <1 ms, consequently, nucleation processes were not accounted for in the model. Temporal discretization is performed using second order implicit time stepping with Courant numbers below one. Reported time-averaged results are sampled over 5 times the residence time of the entire domain.

The computational domain is discretized using a set of 10 prism layers near the wall in both tubing and cell to resolve boundary layer flow and diffusion. The prism layers encapsulate a polyhedral mesh core with gradual refinement going from a coarser core to finest grid near the cell wall.

In terms of surface deposition rates, modelling uncertainties from the simplification of the kinetics and thermodynamics are considerably larger compared to the uncertainties of the flow model, and thus the CFD model is aimed at describing the flow-related effects rather than as a deposition prediction model. A sensitivity study is performed to test the effect of variations to the rate constants k and k_w. While the absolute fluxes and saturation ratio fields are impacted by changing these parameters, the key conclusions remain unchanged.

As a baseline for comparison, a simple one-dimensional plug flow model (PFM) is also implemented. This model relies on an axial discretization of the cell and inlet tubing and is solved temporally through forward integration. This effectively models the kinetics without radial transport limitation and, thus, compared to the CFD model, can be used to highlight the effects of transport.

The domain of the implemented PFM comprises of the deposition cell as well as 40 cell diameters tubing upstream of the cell. The reaction model from Eq. (4) is implemented in each axial cell. All precipitated products are assumed to deposit immediately in the same cell. Thus the PFM model does not account for bulk precipitates being transported with the flow.

2.7. Surface analysis

The surface texture characterization performed in this study was based on the methodology proposed by Klingaa et al. [41], which uses

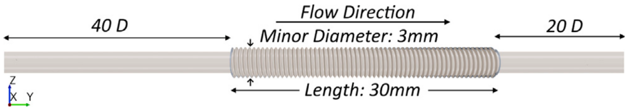

Fig. 2. Illustration of the computational domain for the threaded deposition cell.

an in-house Python code to extract surface texture information from 3D point cloud data, generated from the exported stack of images. The surface profile parameters used in this work are defined as:

$$Pa = \frac{1}{l}\int_0^l |Z(x)|dx \tag{6}$$

where l is the length of investigated surface in the flow direction, x, and $Z(x)$ is the surface height. The spikiness, Pku, is defined as:

$$Pku = \frac{1}{Pq^4}\left(\frac{1}{l}\int_0^l Z(x)^4 dx\right) \tag{7}$$

where Pq is the variation of the surface height:

$$Pq = \sqrt{\frac{1}{l}\int_0^l Z(x)^2 dx} \tag{8}$$

If $Pku < 3$ the profile consists of soft peaks and deep valleys. If $Pku = 3$ the profile has an equal distribution of soft and sharp peaks and valleys. If $Pku > 3$ the profile is characterized as being spiked [41]. These can therefore be used to quantify what kind of height distribution deposited material exhibit on a surface. Pa is the arithmetical mean height of the assessed profile, compared to the mean line of the profile, and gives a general description of the surface texture over the profile length. An increased surface roughness is likely to yield more nucleation sites.

3. Results and discussion

3.1. Attachment and detachment of scale

The rate of scale formation in a system with a high ratio of reaction rate to transport is limited by the transport of ions to the surface. CFD was utilized to investigate the transport phenomenon of the dissolved ions. Turbulent flow is governed by an unsteady turbulent core transitioning into a thin laminar sub-layer near the wall, whereas the laminar flow remains steady and stratified through the fluid bulk. In the stratified layers, the transport of the material towards the wall is limited by diffusion, whereas within the turbulent core, small scale convection due to turbulence drastically increases the transport towards the wall [47]. Transport considerations are neglected in traditional simple reactor models such as the PFM implemented in this study.

The saturation profiles of the bulk fluid, at the investigated conditions, are shown in Fig. 3. The inserts on the right in Fig. 3 illustrate the differences in the concentration gradients near the wall. The laminar flow over the smooth surface has a steeper boundary gradient compared to that of the laminar flow over the threaded surface. This is expected as irregular surfaces are known to increase the size of the boundary layer [48]. From Fig. 3cd it can be observed that for the turbulent-threaded condition, the onset of turbulence occurs closer to the inlet than for the smooth case.

Differences in bulk flow profile affect the influx of material to the surface. To compare the influx between different conditions, Fig. 3e shows the mean material influx for all four cases. Based on these results, the laminar and turbulent flow regimes will be referred to as the low and high influx regimes, respectively.

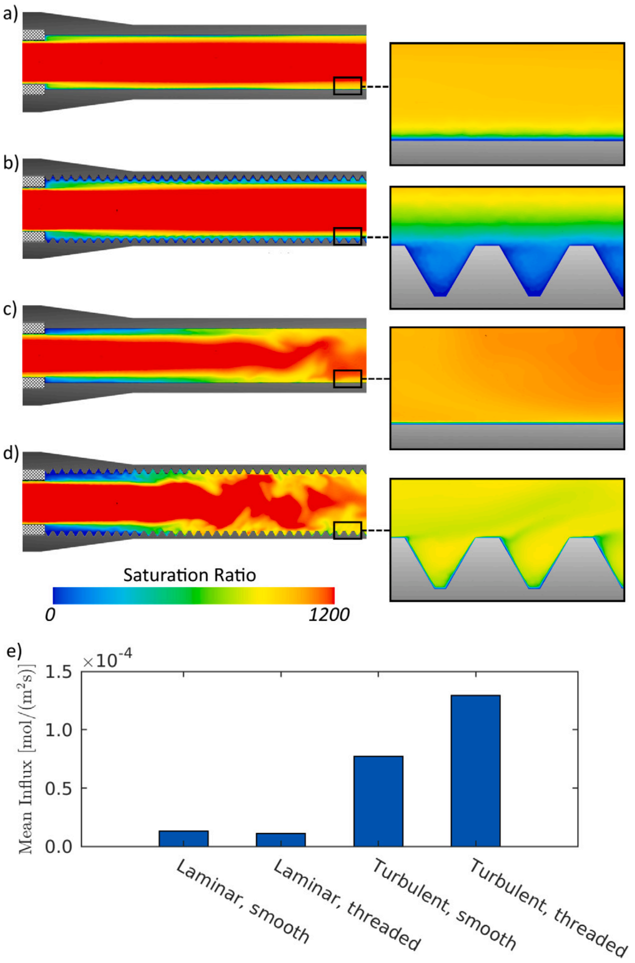

Fig. 3. Simulated bulk saturation profiles. Inserts showing the boundary layer thickness. (a) Laminar, smooth. (b) Laminar, threaded. (c) Turbulent, smooth. (d) Turbulent, threaded (e) Mean material influx.

The main difference between the CFD model and the simpler PFM reactor model is their ability to capture the effects of high vs. low ionic flux towards the cell surface. In Fig. 4 we compare the average surface flux between the CFD and PFM reactor models to put these effects into perspective. Two key aspects governs the difference between the laminar and turbulent conditions. Firstly, the turbulence significantly increases the aforementioned ionic influx, effectively shortening the diffusion time from bulk to wall. Conversely, the residence time becomes significantly lower for the turbulent flow due to the higher flow rate, and consequently, each fluid volume injected has a shorter time span to react onto the cell surface. The PFM model shows a monotonically decreasing flux in the axial direction due to consumption and thus gradually lower concentration, whereas the CFD model shows the combination of an axially increasing flux due to dispersion and axially decreasing due to reaction. The resulting flux is reasonably uniform in the axial direction for both the smooth and threaded cells when averaging over a full pitch length for the laminar flow. In the laminar model, the magnitude of the average fluxes is also similar across the two surface conditions. While the bulk of the flow remains

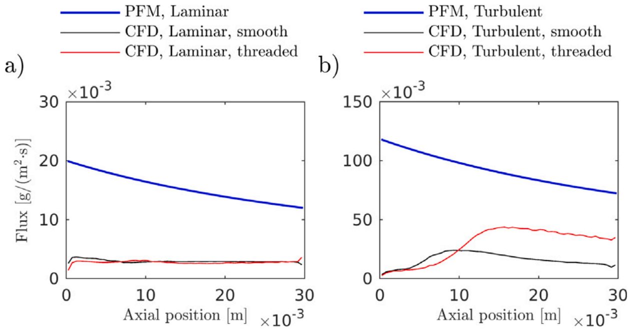

Fig. 4. Comparison between the CFD modelled distribution of deposition compared to the simple plug flow model (PFM). The plotted data from the CFD model is averaged over a thread pitch length to avoid showing the variations over the profile for the threaded models.

laminar, the threading adds rotation and thus increased mixing near the surface. The increased influx is shared over a 1.625 times larger area, and thus surface averaged fluxes remain similar in magnitude. The turbulent flow has a net significant larger influx. This is mainly due to the 4.5 times higher flow rate and thus higher average concentration in the cell, but other factors will be discussed further in this section. In the turbulent flow, the threaded surface gives rise to a significantly higher flux downstream. This is likely explained by the surface texture further increasing the turbulence as the flow develops in the cell.

In Fig. 5 we present the experimentally observed deposited mass and compare it with extrapolated values based on the fluxes obtained from the CFD and PFM models. From the experiments, in both the laminar and turbulent flow, we observe that more mass is deposited on threaded surfaces. As the material is transported to the surface, the crystal growth is determined by either nucleation at new crystal sites or by growth on existing crystal surfaces. While the observation aligns with the higher expected influx in the turbulent case, the CFD results from the laminar studies indicate that the threaded surface experience a similar influx as the smooth surface (see Fig. 5c). However, the observed experimental deposition for the laminar case is significantly higher for the threaded compared to the smooth. This suggests that growth in the low influx regime is not only limited by the material influx.

A surface's potential for scaling could be characterized by its roughness [30]. As the nucleation sites on the clean surface, which in this study were characterized by *Pa*, are identical, it is not the amount of nucleation sites that govern the net deposition. Surface crystallization of low soluble salts has been proposed to be kink limited [49], i.e. more viable nucleation sites exist on the threaded surface. Therefore, the low influx regime's overall deposition is driven by favourable nucleation sites rather than by the overall influx. In the turbulent high influx regime, the material transport governs net deposition. The effect of increased injection rate on the deposited mass is identical for the two surface morphologies: with the same amount of liquid injected through the deposition cell, more mass is deposited under high influx. Fig. 3e shows that the mean flux is significantly increased for the threaded surface compared to the smooth surface under turbulent flow. Under turbulent flow conditions, both smooth and threaded surfaces experience an increase in deposition, which is in line with the calculated influx. The observed mass deposition rate for the [Turbulent, threaded] setup is in line with that of the PFM model, exceeding the extrapolated rate obtained from the CFD simulations. This could either indicate that the effective kinetics are significantly faster than modelled or could be explained by attachment of upstream precipitate particles captured from the flow. The rest of the experiments show more mixed comparison with the extrapolated model fluxes.

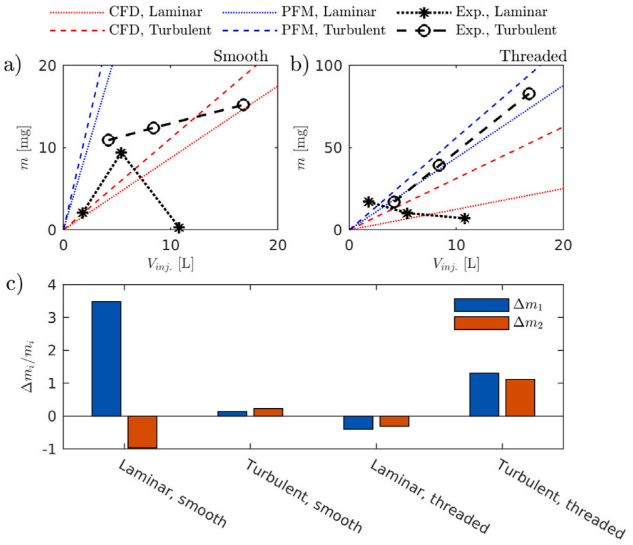

Fig. 5. Mass deposited as a function of injected brine v_{inj}, comparing experimental to PFM and CFD model on (a) smooth surfaces and (b) threaded surfaces as a function of injected brine. The CFD and PFM lines are based on the average deposition rates after they have reached a quasi-steady state. (c) Difference in mass (Δm) deposited between the observations. Δm_i is defined as $m(t_{i+1})$-$m(t_i)$, where t_i refers to the experimental time steps.

Fig. 5c suggests that deposition is not the only process at play; detachment processes also affect the net deposition rate. In the low influx regime, there is evidence for a loss of mass between subsequent time steps. The impact of scale detachment on the net deposition rate can be investigated through the difference in mass between two experimental durations, ($\Delta m = m(t_{i+1}) - m(t_i)$ see Fig. 5c). Hence, $\Delta m < 0$ describes a case of detachment. There is an overall tendency for Δm to be larger on the smooth surface compared to the threaded in the low influx regime. This suggests that detachment processes are more prominent per detachment event on the smooth surface, while the threaded surface has a continuous removal of smaller amounts of deposited mass.

Under high material influx, the deposited mass consistently increased linearly as a function of injected fluid volume (see Fig. 5ab). In contrast, no clear increasing trend is observed under low influx. Since the mass deposited under high influx is observed to increase continuously with injected brine volume, it can be inferred that the impact of detachment is more pronounced in the low influx regime. Based on the results presented so far, no conclusion to the mechanism that causes more pronounced detachment under low influx can be established. It cannot be concluded whether the detachment behaviour occurs periodically or is part of an initial transient.

We have shown how deposition can be quantified through gravimetric data and that both scale attachment and detachment occur. However, to understand these processes, the surface crystal growth distribution must also be quantified.

3.2. Distribution of crystal deposits

To quantify the surface growth distribution, CT scans of deposition cells were performed before and after each study. An axial view of a magnified area of the 2D orthoslices is shown in Fig. 6 to emphasize the location and magnitude of scale deposition. 3D representation of one experiment with related CFD simulations is shown in Fig. 7. The

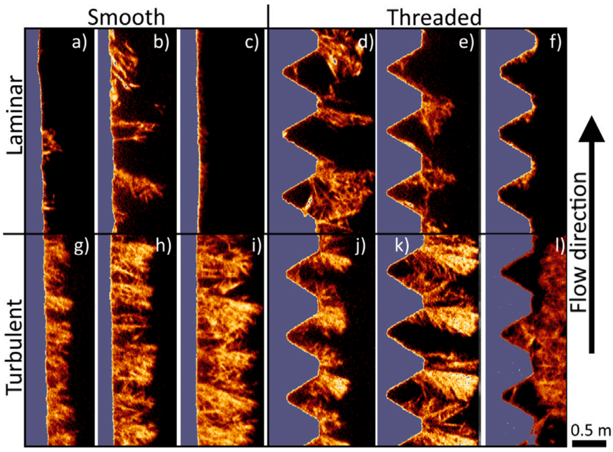

Fig. 6. Orthoslices of micro-CT scans showing a 3 mm long section of each sample. (a)-(c) and (g)-(i) refer to $t_{L,1}$, $t_{L,2}$, $t_{L,3}$, respectively. (d)-(f) and (j)-(l) refer to $t_{T,1}$, $t_{T,2}$, $t_{T,3}$, respectively.

full orthoslices are located in the Supplementary Material. In all cases (Fig. 6), the deposited crystals appear dendritic, similar to previous studies on $BaSO_4$ [50,51]. The deposition distribution vary with surface morphology and fluid hydrodynamics.

The deposition distribution across the threaded surface, observed in Fig. 6df and Fig. 6jl, supports that a spatial modulation of material influx exists. There exist a sizeable local influx of material on the threadings facing the fluid stream (Fig. 7a). By correlating the increased influx with the deposition distribution from Fig. 6jl and Fig. 7c it becomes evident that there is a strong correlation between the material influx and the location at which growth occurs.

The periodicity on the threaded surfaces imposes a material influx pattern which is nonexistent on the smooth surfaces. Therefore, on the smooth surfaces, there is no distinct pattern in which the scaling occurs in either the low or the high influx regimes.

There are two main effects of the effect of hydrodynamics that are present from Fig. 6. First, there is a difference in the deposition features between laminar and turbulent flow conditions. In the low influx regime, the scale is removed and rearranged as more brine is injected. At high material influx, the crystal growth on the threaded surface is located on the area with a locally high influx. Furthermore, the formed crystals possess a larger branching density from the primary dendrites compared to those from the laminar cases. As the experimental duration is increased, the following processes occur: The initiation of dendritic branching, followed by the merging of dendritic branches, and finally, the detachment of adhered crystals. The second effect is that the regime of influx determines the distribution of scale formation. In the low influx regime, crystal growth is localized in clusters and randomly distributed across the surface. Under high influx, the growth is uniformly distributed across the surface.

To quantify this distribution, the micro-CT tomographies were treated with the code previously described in Section 2.7. The output of the code is seen in Fig. 8 and shows a perspective view down the scanned segments, where the colorbar denotes the height deviation from an ellipsoid fitted to the mean plane. For example in Fig. 8.1a few clusters can be observed, while Fig. 8.3f shows a uniform deposition. By tracking the average profile roughness (*Pa*) and the spikiness of the crystal height distribution (*Pku*) in successive order of the experimental duration, it becomes clear that two different physical mechanisms are at play.

For the first time step, $t_{L,1}$, on the smooth surface under low material influx (see Fig. 8.1a, growth occurred in a few scattered localized clusters. This is reflected in the low roughness and the large spikiness (see Fig. 9ab). At the next time step, $t_{L,2}$, deposition still occurs in clusters, but they are more evenly spread (Fig. 8.1b). This deposition characteristic is supported by the increased roughness and the decrease in spikiness. Finally, at $t_{L,3}$, (see Fig. 8.1c, only a few clusters can be observed. However, there is now a thin evenly spread layer of crystals all over the surface. At $t_{L,3}$ for the smooth surface, the least amount of mass was deposited, however from Fig. 8.1c the deposition can be seen as an effect that has occurred on the whole surface, which in addition led to an increase in the roughness from $t_{L,1}$.

The same trend is observed for the threaded surface. While the smooth surface had the highest amount of mass at $t_{L,2}$, for the threaded cell under laminar conditions, the highest amount of deposited mass occurs at $t_{L,1}$. This is supported by the type of height distribution measured on the surface. The high roughness of the surface indicates a large mass deposition, while the low spikiness confirms that deposition is spread over multiple locations. At $t_{L,2}$, crystals were partially removed, and the deposited layer is more scattered. In comparison to the $t_{L,2}$, a decrease of the roughness has occurred, while there is a strong increase in the spikiness. Similar to the data point for the smooth surface at $t_{L,3}$, a more uniformly distributed layer is observed. The changing type of height distribution indicates that the stage of growth can be tracked by the profile texture parameters. This trend of a change in deposition distribution as a function of time is not present in the high influx regime. Here, a new trend can be observed, that is shared across both the smooth and threaded surfaces. The crystals form an evenly distributed layer across the whole surface under these conditions. As mentioned, a more significant degree of dendritic branching and merging of deposited crystals are observed under turbulent conditions. Before branching, at $t_{T,1}$, a large roughness is observed, reflecting large local dendrites emerging from the surface. As the secondary branches merge, the roughness is decreased and the outermost layer becomes more smooth (Fig. 9b). The spikiness varies little (less than 1.5) at all experimental conditions, suggesting that the type of distribution does not change with time.

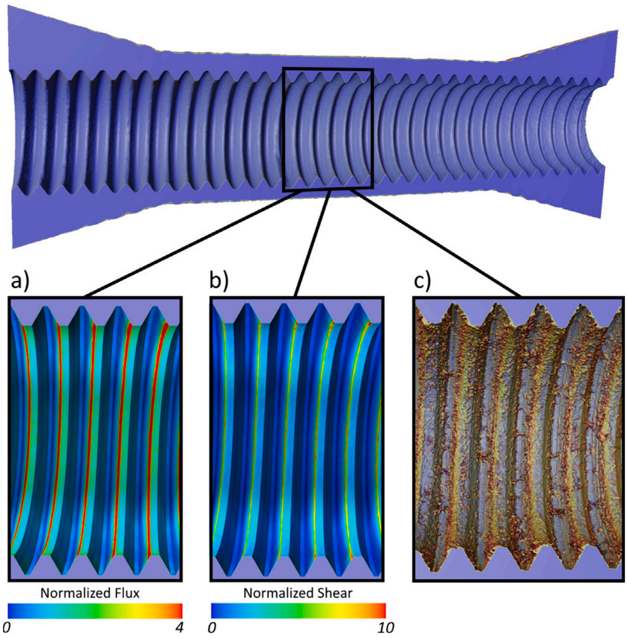

Fig. 7. Threaded surfaces at a high influx regime. (a) simulated time-averaged material influx, (b) simulated time-averaged shear forces and (c) location of scale deposition from CT tomography. The fluxes and shear forces are normalized with the surface-average of the deposition cell wall.

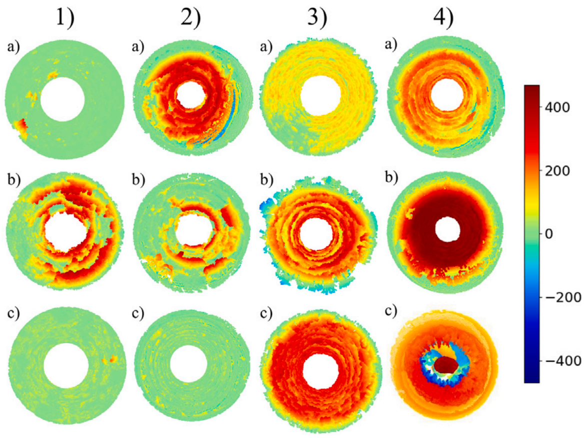

Fig. 8. Perspective view of the analysed cell section. The arrow indicates increased experimental duration. 1 = [Laminar, smooth], 2 = [Laminar, threaded], 3 = [Turbulent, smooth], 4 = [Turbulent, threaded]. (a), (b), and (c) refer to $t_{L,1}$, $t_{L,2}$, $t_{L,3}$, respectively. (d), (e), and (f) refer to $t_{T,1}$, $t_{T,2}$, $t_{T,3}$, respectively.

3.3. Flow dependent growth mechanism

Surface deposition rates are largely controlled by the material flux to the surface. From a thermodynamic consideration, growth is more energetically favourable on existing phases than the formation of a nucleus. A theory used to describe molecular self-assembly provides a framework for a deeper understanding of scaling growth in low and high influx regimes [52]. From molecular self-assembly, the rate governing regime growth can be classified as either thermodynamic or kinetic based on the competition between the diffusion of adsorbents and the magnitude of material influx [52]. In the thermodynamic regime, growth is limited by favourable nucleation sites, where on the contrary, the kinetic regime is when the material supply limits growth. In this study, the molecular surface diffusion is identical because the temperature and material of the surface are the same. However, there is a variation in the surface influx. For large material influx studies, the growth will be of a kinetic character i.e. the movement of a particle is confined to the spatial dimension of the surface and has a small mean path before it adheres completely, either on the pristine surface or with another particle. In the low influx regime, the growth governing mechanism will be of a thermodynamic character as the influx of material is low, resulting in only the most energetically favourable sites occupied [52].

At laminar flow conditions, deposition was observed at a limited number of sites. From this, we infer that nucleation has only occurred at the most thermodynamically favourable sites. Consequently, a phase space where thermodynamics play a more dominant role than the kinetics can be derived. Under turbulent flow, i.e. higher influx to the surface, the uniform deposition pattern suggests that growth and deposition have occurred in multiple nucleation sites. Under these conditions, it can therefore be stated that the contribution of kinetics is more significant than that of thermodynamics.

Local crystal growth is self-reinforcing in the low influx regime. As scale formation occurs in small clusters, this will modulate the flow by creating a shadow zone behind existing crystals. Thereby further transport of material to the surface is limited, and reaction with nucleation sites is inhibited. We illustrated the shadow zone by simulating the flow around a crystal (Fig. 10). Behind the crystal there is a reduced fluid saturation further downstream in the laminar flow condition than under the turbulent conditions. This difference is a consequence of the increased mixing from the eddies in the turbulent flow. This effect is clearly observed from the experimental results in Fig. 10b and d, where the laminar flow conditions yield solitary crystals versus more and denser structures in the turbulent case.

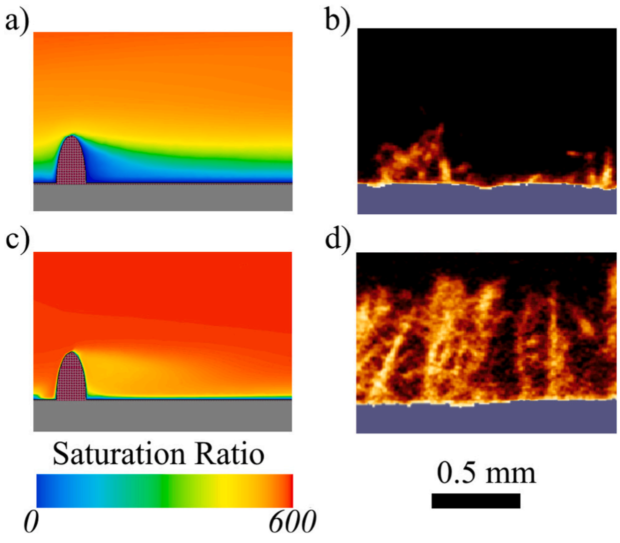

Fig. 10. Visualization of shadowing on a smooth surface. (a) CFD, laminar conditions (b) CT scan of crystal grown under laminar conditions. (c) CFD, turbulent conditions (d) CT scan of crystal grown under turbulent conditions.

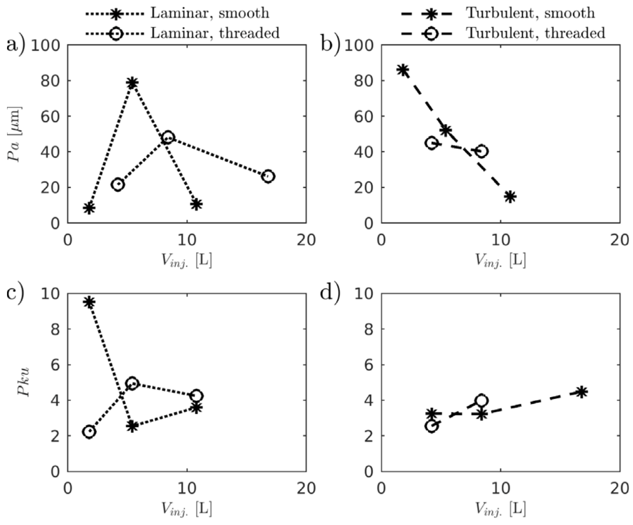

Fig. 9. Texture parameters observed after experiments. (a) *Pa* for laminar flow experiments. (b) *Pa* for turbulent flow experiments. (c) *Pku* for laminar flow experiments. (d) *Pku* for turbulent flow experiments.

Furthermore, the growth on the threading tops facing the fluid stream is enhanced by the increased fluid kinetic energy from turbulence. A temporal periodicity in the influx was revealed to exist on the threadings (see Fig. 11). A time series of the influx was extracted from the CFD model at the top, middle, and bottom of a threading. A correlated periodicity in the influx existed between the three positions. However, the signal from the top and middle positions appears more convoluted. The overall flux magnitude is lower at the bottom of the threading. As the kinetic energy and frequency is correlated, a higher kinetic energy state of the ions would be observed at the top positions on the threadings. The differences in the energy spectrum from the threading valleys to the tops provides further explanation to why there is a significantly higher amount of deposition on the top.

In Fig. 12, the mechanisms behind flow-dependent crystal growth are outlined. In the low influx regime, there are three key steps:

1. **Nucleation in clusters**, where the growth is spatially confined to local clusters, having a high spikiness. Here, deposition is limited by the density of favourable nucleation sites. A consequence of this is that higher deposition will be observed on threaded surfaces in the low influx regime as more viable nucleation sites exist. Solitary growth is self-reinforcing as low mixing in the shadow zones of existing crystals occurs.

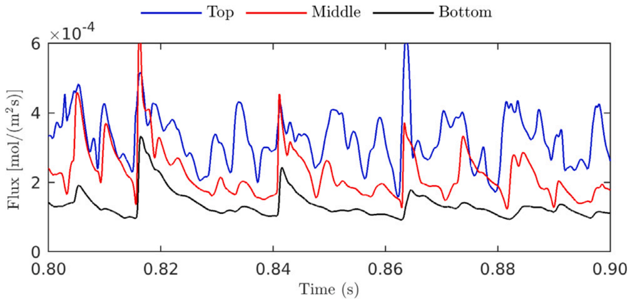

Fig. 11. Spatiotemporally resolved influx experienced by a threading; time series of three locations (top, middle and bottom) on the front of a threading.

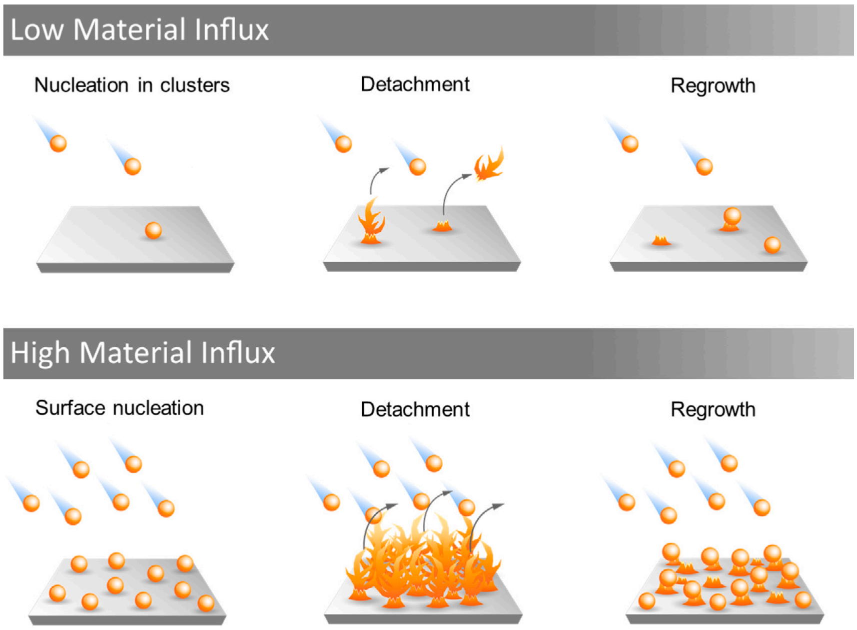

Fig. 12. Mechanistic principles behind the flow dependent growth. Orange spheres represent $BaSO_4$, either as incoming flux or deposited clusters. Low material influx favours local growth of dendrites, whereas many interlinked dendrites are favoured in the high material influx regime.

2. **Detachment** of the crystals occurs when they have reached a size where the forces exerted by the fluid becomes too large. Just before the detachment the growth is characterized by a very high surface roughness. However, as the mean line is shifted and the crystal height distribution is broader, a lower spikiness will be measured.
3. **Regrowth** of new clusters occur on pre-existing deposited material, reflected in an increased spikiness. Regrowth differs from the first step as secondary nucleation occurs on the roots of the detached particles. Thereby, a significantly lower energy is associated with regrowth, caused by the increase of nucleation sites due to the presence of pre-existing deposited material.

Similarly, crystal formation at high material influx conditions can be divided into three key steps:

1. **Initial surface nucleation** is the result of a large influx of material to the surface, and growth occurs as a global phenomenon occupying a larger density of nucleation sites and not only the most favourable sites. Here, the growth rate is kinetically limited as the growth is uniform across the surface. This is confirmed by the low spikiness observed.
2. **Detachment** in the regime with high material influx to the surface occurs with crystals exhibiting a larger height. This is due to the dendritic branching that interlocks existing crystals, giving them an increased surface attachment strength.
3. **Regrowth** will occur after the detachment, however, under turbulent flow conditions, this will be identical to initial surface nucleation, as the deposition is not spatially confined but is seen across the whole surface.

The growth mechanisms described above confirm the observations for laminar flow. Even though the total amount of mass on the surface does not increase with injected fluid, the crystals will be redistributed continuously. This creates a gradually increasing dense crystal layer, resulting in an eventual complete blocking of the cell, impeding the fluid flow. As crystals formed under laminar flow grow locally they will have a relatively small area adhered to the surface. As the shear forces and momentum on the crystals increase with their increasing length, the maximum tension they can withstand will depend on their surface attachment area. As they are not interlinked to other crystals, which is the case in the high influx regime, they will have a relatively weak attachment. On the other hand, crystals formed in the high influx regime will be interconnected and therefore have a relatively larger area of contact to the surface than the crystals formed under low influx.

3.4. Implications for future prediction models and field operators

The findings of this work demonstrate the importance of accounting for detachment in a comprehensive prediction of scale build-up. Previous prediction models have overestimated fouling rates because either the effect of detachment was not accounted for [53] or not incorporated correctly [54]. Newer models, accounting for the effect of scale detachment and attachment strength, have also been developed [26,55]. However, these models are insufficient, as their description of scale attachment strength is incomprehensive. We have shown in Section 3.2 that the distribution of crystal on the surface is directly linked to the surface attachment strength. These models fail because they do not account for crystal distribution. Consequently, detachment processes cannot be addressed comprehensively. To create a unified prediction model, it would be necessary to describe surface attachment strength accurately.

Real-world challenges exist where field operators experience the consequences of crystal distribution. For example, in transport pipelines, scaling and corrosion will, throughout its life-cycle, change the surface texture and alter the fouling formation rate. We have shown how deposition will vary in a non-linear manner throughout the life-time of production equipment. A smooth newly fabricated pipeline will experience a random distribution, whereas a worn surface will agitate turbulence in the fluid flow and reduce energy requirements for surface deposition, thereby reinforcing scale deposition.

Ageing of fouling deposit is the temporal transformation of a deposited layer and is considered one of the principal mechanistic stages of overall deposition [25]. In heat exchangers, ageing is seen to drastically increase fouling rate at production equipment's end life-time [34]. Our findings demonstrate how detachment can occur after a longer period when there is a larger interlocking between deposited scale. Scale removal devices based on fluid agitation operates on these basic mechanisms [56]. Based on our findings, the mechanism of this device can be deduced. As crystal growth is removed before interlocking occurs, the crystal distribution is of a singular manner. This prevents larger sections from interlocking, and overall scale deposition is minimized as the surface attachment strength is lowered.

The nature of fouling is complex and determines the strength of the surface attachment. Crystallization fouling, adhering through nucleation, has a strong attachment, while biological fouling has a weaker adherence to the surface [57]. Biofouling was reduced in decentralized wastewater treatment operating at low aeration shear force [58]. Our findings support the notion that the deposition distribution and its interaction with shear forces will redistribute the fouling layer, resulting in a more dense layer being formed over time. This layer is known to be more resistant to mechanical removal [57]. Therefore, to understand the net formation of fouling, the distribution of deposition must be considered.

The distribution of fouling deposition has real-world implications, where the spatial modulation of fluid will create a deposition distribution, which will reinforce itself over time. The interlocking of crystals results in stronger attachment strength, and by minimizing the interconnection between deposited material, overall deposition can be reduced. As singular crystals are iteratively redistributed, more resilient scaling is formed.

4. Conclusion

In summary, we revealed novel insights about scaling. We show that the impact of attachment and detachment processes is surface and flow-dependent. Smooth surfaces experience an areal uniform material influx, as demonstrated by the random deposition observed, irrespective of the flow regime. Threaded surfaces modulate flow profile and increased material influx locally; this variation in material influx caused patterned deposition distribution. Flow facing protuberances have a high deposition, which can be correlated to the areas where the material is transported. Areas with low material transport (such as valleys and the shadow side of the threads) showed reduced surface deposition. In the laminar low influx regime, solitary crystals formed due to few nucleation sites being occupied. The increase in favourable nucleation site on threaded surfaces acted as a growth template, thereby increasing formation on threaded surfaces compared to the smooth. The formation of these crystals created a shadow region behind them, decreasing the likelihood for further growth. Calculations of shear stress distribution revealed a correlation between locations of high shear forces and detachment processes of solitary crystals. Deposits on threaded surfaces experienced more local shear stress, which likely resulted in more frequent detachment of material on the threaded surfaces than on the smooth. Consequently, iterative detachment processes resulted in an increasingly dense adhered layer. In the turbulent high material influx regime, numerous nucleation sites were occupied; this is in contrast to the confined crystals observed under low material influx. Interlocking crystal branches increase surface attachment strength, thereby delaying detachment events.

Combining these mechanistic insights provides a template for scaling prediction models to be developed where the importance of material detachment, surface texture, and influx regimes are incorporated.

Acknowledgments

The authors acknowledge the Danish Underground Consortium (TotalEnergies, E&P Denmark, Noreco & Nordsofonden). This work was funded by the Danish Hydrocarbon Research and Technology Centre (DHRTC) under the CTR2 program. The authors also acknowledged the 3D Imaging Center (3DIM) at The Technical University of Denmark (DTU) for their support on X-ray computed tomography acquisition.

Declaration of competing interest

The authors declare that they have no known competing financial interests or personal relationships that could have appeared to influence the work reported in this paper.

Appendix A. Supplementary data

Supplementary material related to this article can be found online at https://doi.org/10.1016/j.cej.2021.132583.

References

[1] K.M. Sassi, I.M. Mujtaba, Optimal design and operation of reverse osmosis desalination process with membrane fouling, Chem. Eng. J. 171 (2) (2011) 582–593, http://dx.doi.org/10.1016/j.cej.2011.04.034.

[2] I. Sreedhar, S. Khaitan, R. Gupta, B.M. Reddy, A. Venugopal, An odyssey of process and engineering trends in forward osmosis, Environ. Sci. Water Res. Technol. 4 (2) (2018) 129–168, http://dx.doi.org/10.1039/c7ew00507e.

[3] A. Deshmukh, C. Boo, V. Karanikola, S. Lin, A.P. Straub, T. Tong, D.M. Warsinger, M. Elimelech, Membrane distillation at the water-energy nexus: Limits, opportunities, and challenges, Energy Environ. Sci. 11 (5) (2018) 1177–1196, http://dx.doi.org/10.1039/c8ee00291f.

[4] R. Sharifian, R.M. Wagterveld, I.A. Digdaya, C. Xiang, D.A. Vermaas, Electrochemical carbon dioxide capture to close the carbon cycle, Energy Environ. Sci. 14 (2) (2021) 781–814, http://dx.doi.org/10.1039/D0EE03382K.

[5] J. Li, M. Tang, Z. Ye, L. Chen, Y. Zhou, Scale formation and control in oil and gas fields: A review, J. Dispersion Sci. Technol. 38 (5) (2017) 661–670, http://dx.doi.org/10.1080/01932691.2016.1185953.

[6] Q. Zhao, Y. Liu, C. Wang, S. Wang, H. Müller-Steinhagen, Effect of surface free energy on the adhesion of biofouling and crystalline fouling, Chem. Eng. Sci. 60 (17) (2005) 4858–4865, http://dx.doi.org/10.1016/j.ces.2005.04.006.

[7] G. Geovani, M. Argueta, Rehabilitation of geothermal wells with scaling problems, Technical Report, The United Nations University, 1995, pp. 207–240.

[8] H. Müller-Steinhagen, Heat transfer fouling: 50 years after the Kern and Seaton model, Heat Transfer Eng. 32 (1) (2011) 1–13, http://dx.doi.org/10.1080/01457632.2010.505127.

[9] R. Boch, A. Leis, E. Haslinger, J.E. Goldbrunner, F. Mittermayr, H. Fröschl, D. Hippler, M. Dietzel, Scale-fragment formation impairing geothermal energy production: interacting H_2S corrosion and $CaCO_3$ crystal growth, Geotherm. Energy 5 (1) (2017) 4, http://dx.doi.org/10.1186/s40517-017-0062-3.

[10] A. Boersma, F. Vercauteren, H. Fischer, F. Pizzocolo, Scaling assessment, inhibition and monitoring of geothermal wells, in: 43rd Workshop on Geothermal Reservoir Engineering, 2018, pp. 1–13.

[11] A. Ruiz-García, N. Melián-Martel, I. Nuez, Short review on predicting fouling in RO desalination, Membranes 7 (4) (2017) 1–17, http://dx.doi.org/10.3390/membranes7040062.

[12] A. Alabi, M. Chiesa, C. Garlisi, G. Palmisano, Advances in anti-scale magnetic water treatment, Environ. Sci. Water Res. Technol. 1 (4) (2015) 408–425, http://dx.doi.org/10.1039/c5ew00052a.

[13] A. Yi-Tsung Lu, A.T. Kan, M.B. Tomson, Nucleation and crystallization kinetics of barium sulfate in the hydrodynamic boundary layer: An explanation of mineral deposition, Cryst. Growth Des. 21 (3) (2021) 1443–1450, http://dx.doi.org/10.1021/acs.cgd.0c01027.

[14] M.A. Jafar Mazumder, A review of green scale inhibitors: Process, types, mechanism and properties, Coatings 10 (10) (2020) 1–29, http://dx.doi.org/10.3390/coatings10100928.

[15] D. Hasson, H. Shemer, A. Sher, State of the art of friendly "green" scale control inhibitors: A review article, Ind. Eng. Chem. Res. 50 (12) (2011) 7601–7607, http://dx.doi.org/10.1021/ie200370v.

[16] R. Benvie, T. Chen, S. Heath, P. Chen, H. Montgomerie, T. Hagen, New environmentally acceptable chemistry and evaluation methods for scale inhibitor testing under turbulent flow and harsh scaling conditions, in: SPE International Oilfield Scale Conference and Exhibition, 2012, pp. 1–12, http://dx.doi.org/10.2118/155428-MS.

[17] Z.J. Dai, Y.T. Lu, A. Kan, C. Leschied, Y. Zhao, C. Dai, X. Wang, S. Paudyal, S. Ko, M. Tomson, A mechanistic software platform for mineral surface deposition and inhibition prediction under different flow conditions, Desalination 509 (January) (2021) 115071, http://dx.doi.org/10.1016/j.desal.2021.115071.

[18] T. Karmakar, P.M. Piaggi, M. Parrinello, Molecular dynamics simulations of crystal nucleation from solution at constant chemical potential, J. Chem. Theory Comput. 15 (12) (2019) 6923–6930, http://dx.doi.org/10.1021/acs.jctc.9b00795.

[19] B.U. Anabaraonye, J.R. Bentzon, I. Khaliqdad, K.L. Feilberg, S.I. Andersen, J.H. Walther, The influence of turbulent transport in reactive processes: A combined numerical and experimental investigation in a Taylor-Couette reactor, Chem. Eng. J. (2021) 129591, http://dx.doi.org/10.1016/j.cej.2021.129591.

[20] A. Quddus, I. Allam, $BaSO_4$ scale deposition on stainless steel, Desalination 127 (3) (2000) 219–224, http://dx.doi.org/10.1016/S0011-9164(00)00012-6.

[21] Q. Wang, T. Chen, F. Al-Dawood, New understanding on calcium carbonate scaling kinetics, in: NACE - International Corrosion Conference Series, 2019.

[22] A.B. BinMerdhah, A.A.M. Yassin, M.A. Muherei, Laboratory and prediction of barium sulfate scaling at high-barium formation water, J. Pet. Sci. Eng. 70 (1) (2010) 79–88, http://dx.doi.org/10.1016/j.petrol.2009.10.001.

[23] M. Tranter, M. De Lucia, M. Wolfgramm, M. Kühn, Barite scale formation and injectivity loss models for geothermal systems, Water 12 (11) (2020) http://dx.doi.org/10.3390/w12113078.

[24] E.F. Somerscales, Fundamentals of corrosion fouling, Exp. Therm. Fluid Sci. 14 (4) (1997) 335–355, http://dx.doi.org/10.1016/S0894-1777(96)00136-7.

[25] N. Epstein, Thinking about heat transfer fouling: A 5 × 5 matrix, Heat Transfer Eng. 4 (1) (1983) 43–56, http://dx.doi.org/10.1080/01457638108939594.

[26] Z. Han, Z. Xu, X. Yu, CFD modeling for prediction of particulate fouling of heat transfer surface in turbulent flow, Int. J. Heat Mass Transfer 144 (2019) 118428, http://dx.doi.org/10.1016/j.ijheatmasstransfer.2019.07.078.

[27] D. Yang, J. Liu, E. Xiaoxue, L. Jiang, Model for seawater fouling and effects of temperature, flow velocity and surface free energy on seawater fouling, Chin. J. Chem. Eng. 24 (5) (2016) 658–664, http://dx.doi.org/10.1016/j.cjche.2016.01.012.

[28] A.J. Karabelas, Scale formation in tubular heat exchangers - Research priorities, Int. J. Therm. Sci. 41 (7) (2002) 682–692, http://dx.doi.org/10.1016/S1290-0729(02)01363-7.

[29] M.J. Li, S.Z. Tang, F. long Wang, Q.X. Zhao, W.Q. Tao, Gas-side fouling, erosion and corrosion of heat exchangers for middle/low temperature waste heat utilization: A review on simulation and experiment, Appl. Therm. Eng. 126 (2017) 737–761, http://dx.doi.org/10.1016/j.applthermaleng.2017.07.095.

[30] M.M. Vazirian, T.V. Charpentier, M. de Oliveira Penna, A. Neville, Surface inorganic scale formation in oil and gas industry: As adhesion and deposition processes, J. Pet. Sci. Eng. 137 (2016) 22–32, http://dx.doi.org/10.1016/j.petrol.2015.11.005.

[31] X. Xing, C. Ma, Y. Chen, Mechanism of calcium carbonate scale deposition under subcooled flow boiling conditions, Chin. J. Chem. Eng. 13 (4) (2005) 464–470, http://citeseerx.ist.psu.edu/viewdoc/summary?doi=10.1.1.463.3717.

[32] G. Graham, L. Boak, C. Hobden, Examination of the effect of generically different scale inhibitor species (PPCA and DETPMP) on the adherence and growth of barium sulphate scale on metal surfaces, in: SPE International Oilfield Scale Conference and Exhibition, 2001, pp. 1–15, http://dx.doi.org/10.2118/68298-MS.

[33] M. Pourbozorg, T. Li, A.W. Law, Effect of turbulence on fouling control of submerged hollow fibre membrane filtration, Water Res. 99 (2016) 101–111, http://dx.doi.org/10.1016/j.watres.2016.04.045.

[34] A. Janzen, E.Y. Kenig, S.E. Gmbh, R. Federation, Understanding and analysis of fouling behavior of bare-wire heating elements in electric water heating, in: Heat Exchanger Fouling and Cleaning, 2019, pp. 1–8.

[35] S. Keysar, R. Semiat, D. Hasson, J. Yahalom, Effect of surface roughness on the morphology of calcite crystallizing on mild steel, J. Colloid Interface Sci. 162 (2) (1994) 311–319, http://dx.doi.org/10.1006/jcis.1994.1044.

[36] S. Kazi, G. Duffy, X. Chen, Mineral scale formation and mitigation on metals and a polymeric heat exchanger surface, Appl. Therm. Eng. 30 (14–15) (2010) 2236–2242, http://dx.doi.org/10.1016/j.applthermaleng.2010.06.005.

[37] V. Eroini, N. Kapur, A. Neville, M. Euvrard, Preventing scale formation using modified surfaces, in: NACE - International Corrosion Conference Series, 2011, pp. 1–15.

[38] H. Wang, V. Alfredsson, J. Tropsch, R. Ettl, T. Nylander, Formation of $CaCO_3$ deposits on hard surfaces - Effect of bulk solution conditions and surface properties, ACS Appl. Mater. Interfaces 5 (10) (2013) 4035–4045, http://dx.doi.org/10.1021/am401348v.

[39] A.K. Halvey, B. Macdonald, A. Dhyani, A. Tuteja, Design of surfaces for controlling hard and soft fouling, Philos. Trans. R. Soc. A 377 (2138) (2019) 20180266, http://dx.doi.org/10.1098/rsta.2018.0266.

[40] N. Gathimba, Y. Kitane, T. Yoshida, Y. Itoh, Surface roughness characteristics of corroded steel pipe piles exposed to marine environment, Constr. Build. Mater. 203 (2019) 267–281, http://dx.doi.org/10.1016/j.conbuildmat.2019.01.092.

[41] C. Klingaa, T. Dahmen, S. Baier, S. Mohanty, J. Hattel, X-ray CT and image analysis methodology for local roughness characterization in cooling channels made by metal additive manufacturing, Addit. Manuf. 32 (2020) 101032, http://dx.doi.org/10.1016/j.addma.2019.101032.

[42] K.S. Pitzer, Thermodynamics of electrolytes. I. Theoretical basis and general equations, J. Phys. Chem. 77 (2) (1973) 268–277, http://dx.doi.org/10.1021/j100621a026.

[43] B.Y. Zhen-Wu, K. Dideriksen, J. Olsson, P.J. Raahauge, S.L. Stipp, E.H. Oelkers, Experimental determination of barite dissolution and precipitation rates as a function of temperature and aqueous fluid composition, Geochim. Cosmochim. Acta 194 (2016) 193–210, http://dx.doi.org/10.1016/j.gca.2016.08.041.

[44] Z. Dai, F. Zhang, F. Yan, N. Bhandari, G. Ruan, Z. Zhang, Y. Liu, H.A. Alsaiari, Y.T. Lu, G. Deng, A.T. Kan, M. Tomson, A new theoretical model for the induction time and scale inhibitor dosage predictions for calcite and barite over wide ranges of temperature, inhibition concentration and saturation index, in: SPE International Symposium on Oilfield Chemistry, 2017, pp. 647–657, http://dx.doi.org/10.2118/184547-ms.

[45] D. Bosbach, Linking molecular-scale barite precipitation mechanisms with macroscopic crystal growth rates, in: Water-Rock Interactions, Ore Deposits, and Environmental Geochemistry: A Tribute to David A. Crerar, 2002, pp. 97–110.

[46] F. Yang, A.G. Stack, V. Starchenko, Micro-continuum approach for mineral precipitation, Sci. Rep. 11 (1) (2021) 1–14, http://dx.doi.org/10.1038/s41598-021-82807-y.

[47] F.M. White, Fluid Mechanics, seventh ed., McGraw Hill, Inc., 2011.

[48] A. Ivask, I. Kurvet, K. Kasemets, I. Blinova, V. Aruoja, S. Suppi, H. Vija, A. Käkinen, T. Titma, M. Heinlaan, M. Visnapuu, D. Koller, V. Kisand, A. Kahru, Size-dependent toxicity of silver nanoparticles to bacteria, yeast, algae, crustaceans and mammalian cells in vitro, PloS One 9 (7) (2014) 102108, http://dx.doi.org/10.1371/journal.pone.0102108.

[49] J.J. De Yoreo, L.A. Zepeda-Ruiz, R.W. Friddle, S.R. Qiu, L.E. Wasylenki, A.A. Chernov, G.H. Gilmer, P.M. Dove, Rethinking classical crystal growth models through molecular scale insights: Consequences of kink-limited kinetics, Cryst. Growth Des. 9 (12) (2009) 5135–5144, http://dx.doi.org/10.1021/cg900543g.

[50] J.M. García-Ruiz, F. Otálora, Crystal growth in geology: Patterns on the rocks, in: Handbook of Crystal Growth: Bulk Crystal Growth: Second Edition, second ed., 2015, pp. 1–43, http://dx.doi.org/10.1016/B978-0-444-63303-3.00001-8.

[51] N.S. Dera, F. Fatra, G. Ivanto, S. Muryanto, A.P. Bayuseno, Phase analysis and crystal morphology of barium sulphate precipitated from the laminar flowing water, in: IOP Conference Series: Materials Science and Engineering, vol. 202, 2017, 012029, http://dx.doi.org/10.1088/1757-899X/202/1/012029.

[52] J.V. Barth, G. Costantini, K. Kern, Engineering atomic and molecular nanostructures at surfaces, Nature 437 (7059) (2005) 671–679, http://dx.doi.org/10.1038/nature04166.

[53] D. Hasson, M. Avriel, W. Resnick, T. Rozenman, S. Windreich, Mechanism of calcium carbonate scale deposition on heat-transfer surfaces, Ind. Eng. Chem. Fundam. 7 (1) (1968) 59–65, http://dx.doi.org/10.1021/i160025a011.

[54] X. Yang, W. Li, L. Guo, X. Liu, H. Feng, Prediction of $CaCO_3$ scaling in water injection wellbore, Appl. Therm. Eng. 98 (2016) 532–540, http://dx.doi.org/10.1016/j.applthermaleng.2015.12.048.

[55] C. Paz, E. Suárez, M. Conde, J. Vence, Development of a computational fluid dynamics model for predicting fouling process using dynamic mesh model, Heat Transfer Eng. 41 (2) (2020) 199–207, http://dx.doi.org/10.1080/01457632.2018.1522108.

[56] A. Krueger, F. Pouponnot, P. Houston, S.A. Petroval, Heat exchanger performance enhancement through the use of tube inserts in refineries and chemical plants – successful applications, in: International Conference on Heat Exchanger Fouling and Cleaning VIII, 2009, pp. 399–406.

[57] S. Fernandes, I.B. Gomes, L.C. Simões, M. Simões, Overview on the hydrodynamic conditions found in industrial systems and its impact in (bio)fouling formation, Chem. Eng. J. 418 (2021) 129348, http://dx.doi.org/10.1016/j.cej.2021.129348.

[58] A. Ding, H. Liang, G. Li, N. Derlon, I. Szivak, E. Morgenroth, W. Pronk, Impact of aeration shear stress on permeate flux and fouling layer properties in a low pressure membrane bioreactor for the treatment of grey water, J. Membr. Sci. 510 (2016) 382–390, http://dx.doi.org/10.1016/j.memsci.2016.03.025.

5 Paper 4: The impact of spatio-temporal variability on the reaction kinetics of miscible fluids

The Impact of Spatio-Temporal Variability on the Reaction Kinetics of Miscible Fluids

Jakob Roar Bentzon*
Department of Civil and Mechanical Engineering,
Technical University of Denmark, Kgs. Lyngby, Denmark

Benaiah U. Anabaraonye
The Danish Hydrocarbon Research and Technology Centre,
Technical University of Denmark, Kgs. Lyngby, Denmark

Jens Honore Walther
Department of Civil and Mechanical Engineering,
Technical University of Denmark, Kgs. Lyngby, Denmark and
Computational Science and Engineering Laboratory,
ETH, Zürich, CH-8092, Switzerland

(Dated: January 16, 2023)

The mixing of miscible fluids is a ubiquitous process relevant to a wide range of reactive systems. Adequate mixing is essential in experimental procedures for determining reaction kinetics. Homogeneity is often assumed yet seldomly verified experimentally or through simulations. This work proposes a numerical approach with a relevant kinetics-based homogeneity index quantifying the mixing state and providing a kinetic correction factor for subsequent model fitting. We show examples of this approach applied to in-house experiments at varying stirring rates. Our results highlight the potential of quantifying reaction inhomogeneity and its effect on experimental data. However, while we indicate that finer computational refinement could theoretically achieve the necessary gradient resolution, we show that current computational resources and performance limit such refinement. This argument presents the cause for the further development of computational sub-grid-scale models to account for the spatial averaging of reactivity through micro-mixing. The introduction of the kinetics-based homogeneity index is the first step in introducing a sub-grid-scale rate correction term in LES modelling and a metric for scientifically describing hydrodynamics of kinetic experiments. We compare this homogeneity index to the EDC inhomogeneous reaction model as well as a probability density function approach. Finally, we propose a simple transport based inhomogeneity reaction model as an alternative to the former two and discuss the advantages of such a model.

Highlight 1: We highlight the non-diminishing effect of fluid mixing on observed rate constants under relatively well-stirred conditions.

Highlight 2: A kinetics-based homogeneity index is proposed as a reactor-state model to include mixing rates in the derivation of reaction rates from experiments

Highlight 3: Modelling the reactive homogeneity state of reactors at varying Reynolds numbers highlights the ability of this model to explain differences in observed rate constants

Highlight 4: We highlight gaps in current LES modelling to accurately model micro-mixing in reactive turbulent flows based on fundamental principles

Highlight 5: We discuss the current approaches to sub-grid scale kinetic modelling within LES modelling and propose a simple transport-based approach

I. INTRODUCTION

In chemical engineering, mixing miscible reacting fluids is ubiquitous [1]. Consequently, simulations modelling species transport in reactive flows play a significant role in many industrial aspects. Accurately capturing the physics of diffusive and advective transport is especially important in circumstances where the Damköhler number is high, i.e., where the underlying kinetics are much faster than the rate of transportation and, consequently, the net reaction rates are strongly affected by transport.

Spatial and temporal modelling of reactive flow using, e.g., *computational fluid dynamics* (CFD), is increasingly widespread. Over the last few decades, such models have presented a fundamental shift from similarity-driven empirical methods toward more fundamental physics-driven numerical approaches. This shift has, in consequence, shifted the prerequisites for accurate modelling from experimental similarity to accurate mathematical descriptions of fundamental physical chemistry.

Adequate mixing is particularly relevant in experimental work to determine fundamental reaction models. Experiments conducted in stirred reactors are widely used to determine reaction kinetics and thermodynamics for subsequent modelling. Reactors are stirred to achieve a near-homogeneous solution under which the spatial reactant concentration gradients are minimal. Under such conditions, the reaction rates are negligibly spatially variant; thus, transport affects the reaction minimally. Such conditions justify the derivation of reaction models based on measured sample concentrations rather than determining spatio-temporal reactant distributions. Unfortunately, such conditions are seldomly achievable in laboratories, and thus the experimental output contains a non-negligible artefact from the mixing state [2, 3].

---

* jroben@mek.dtu.dk

Due diligence studies such as those performed in [3] can determine the stirring rates at which changes in observed reaction rate with increased mixing are acceptably low and indicate the magnitude of these mixing-related artefacts to the reader. While these are suggested as *best practices* [4], their application is far from prevalent. Moreover, increasing stirring rates might not linearly increase the rate of reactant mixing, leading to the potentially erroneous conclusion that the reactant concentrations are homogeneous. Where variations remain, quantifying their significance in terms of the effect on net kinetics would be beneficial.

Through the application of CFD, this paper proposes a kinetics-based homogeneity index of the experimental conditions through relatively simple considerations. Thus, we propose a simple framework for presenting academic readers with more accurate descriptions of reaction rate experiments and accompanying models. In addition, such an index supplies a framework for approximating a correction factor to the observed kinetics.

This paper focuses on the relatively simple precipitation dynamics of barium sulphate. While reactive modelling ranges widely across reactive systems, the underlying principles of this study can be transferred to a wide range of disciplines and systems.

II. MIXING PROCESSES

Mixing refers to the process of transforming a solution from heterogeneous to homogeneous. Mixing of miscible fluids occurs through the diffusion of species across concentration gradients. Diffusion in turbulent flows, such as those observed in stirred reactors, is enhanced through small-scale advective processes that stretch and fold the interfaces between the fluids [2, 5–7].

In many reacting flows, two or more miscible brines containing various reacting and non-reacting species are typically mixed. In such systems, two parallel processes control the spatio-temporal state; firstly, the above-mentioned mixing process, and, secondly, the reaction kinetics converting reactants to products. These two processes are strongly interlinked, and consequently, any modelling effort is limited to the accuracy of the lesser accurate.

In some processes, such as crystallization and corrosion, fluid-solid interfaces such as walls or particles alter the local thermodynamics and reactivity near those interfaces [8]. Consequently, spatial gradients arise between faster and slower reacting zones adding further transport-coupled inhomogeneity to the reaction kinetics.

Various metrics have been proposed for the quantification of mixing [9]. For a single specie dissolved in a solvent, both the concentration variance and the ratio of the volume containing more than or equal to the average concentration has been proposed as homogeneity measures by Rao *et al.* [10]. Experimental methods using fluorescent dyes have been used in mixing two or more species, utilizing the resulting fluorescent intensities from photographs as data. From such data, the root-mean-square difference between local and average intensities presents a measure of homogeneity [9, 11]. In some reactors, three-dimensional spatial gradients make photographic methods more challenging [9]. With the maturation of computational methods and resources, numerical modelling offers a more universally applicable solution for analyzing spatio-temporal variations in mixed solutions.

Although computational resources continuously improve, directly simulating all the physics of most real-life systems is seldomly feasible. For this reason, simulations are typically used to gather statistical insights that are generally applicable to the system analyzed. Therefore, efficient modelling hinges on effectively gathering representative data from simulations. This paper explores the current numerical modelling practices to gather such insights and highlights the significance of interpreting the kinetics as part of the obtained statistic in a generic way.

III. NUMERICAL MODELLING OF REACTIVE FLOWS

Numerical analyses, such as CFD simulations, offer a range of methods to simulate the dynamics, mixing and kinetics of fluids in a coupled model. The most explicit methods within CFD are *direct numerical simulations* (DNS) of the governing physical equations using, e.g., finite-difference modelling. For such methods to capture the relevant variations, the computational model must resolve gradients down to the finest length scales. These length scales can be experimentally determined or estimated through stability analyses.

The Kolmogorov length scale estimates the finest velocity field wavelength sustainable in a viscous fluid. Similarly, the Batchelor length scale estimates the finest concentration variation wavelengths sustainable before being cut off by molecular diffusivity [12]. While DNS provides an essential tool to model fundamental physics and small scales, limitations on computational power render refinement down to these length scales infeasible for nearly all engineering scale applications. Consequently, simulations implicitly or explicitly filter the wavelengths resolved by modelling within finite computational grid sizes.

Accounting for implicit and explicit filtering effects from the smaller wavelengths becomes critical when simulating at feasible spatial and temporal refinement levels. *Large-eddy simulations* (LES) and *Reynolds averaged Navier-Stokes* (RANS) are the most commonly applied group of methods [13].

RANS models generally aim at modelling the temporally averaged conditions, whereas LES models provide spatial filtering down to the computational grid but keep larger variations unfiltered. Hence, the LES approach allows for a partially resolved modelling of the spatio-temporal variations. The increasing adoption of LES has improved the modelling of reactive flows over the last decades [14–16].

In LES, a spatial filter function, G, is applied to the spatially variant fields, $f(\mathbf{x}, t)$, such that

$$\overline{f}(\mathbf{x}, t) = \int_{\Omega} G(\mathbf{x} - \mathbf{x}', \Delta) f(\mathbf{x}', t) d\mathbf{x}' \tag{1}$$

where Δ is the filter width and $\overline{f}(\mathbf{x}, t)$ the filtered field. The filtering may be implemented explicitly through defining G and filtering the governing equations or implicitly recognizing that the numerical discretization will act as a low-pass filter. The advantages of either method have been thoroughly discussed in the literature and will not be touched upon in this paper.

Artefacts caused by sub-grid-scale variation affecting the super-grid-scale physics materialize upon filtering the non-linear terms in the governing equations. In order to account for these, the field of *sub-grid-scale* modelling is introduced. SGS modelling implements closure models for higher-order quantities into the numerical representation of the governing equations. These closure models combine physical considerations and data fitting to achieve general applicability across different flow regimes.

The most central sub-grid-scale artefact in LES modelling is the increased momentum dissipation from filtering the momentum-convective term. This increase in momentum dissipation is modelled by introducing a sub-grid-scale viscosity (ν_{SGS}). The most commonly applied sub-grid-scale viscosity models are the *dynamic Smagorinsky model* [17], and the *wall-adaptive large eddy* (WALE) model described in [18]. These models have yielded good results for a wide range of applications [19].

Similar to adding momentum diffusivity, the small-scale fluctuations affect the diffusion of reactant concentrations. Such sub-grid-scale diffusivity (D_{SGS}) is commonly modelled using a transformation of ν_{SGS}, e.g., by applying a constant turbulent Schmidt number $\mathrm{Sc}_t = \nu_{SGS}/D_{SGS}$.

While sub-grid-scale fluctuations in the reactant concentrations increase overall diffusivity, the filtering step removes the information about the distribution of concentrations within the cell. The effective kinetic rates within the cell are thus calculated based on the average concentrations. The gap between the average actual kinetic rate and the one based on the average reactant concentrations presents the need for a third sub-grid-scale model to couple the kinetics and turbulence. Such a model has typically been denoted as a *turbulence-kinetics interaction* (TKI) model.

A common TKI model is the *eddy dissipation concept* (EDC) [20]. EDC is built on the assumption that the reaction is confined to the cell domains governed by fine turbulence structures and assumed homogeneous reaction herein. The EDC model introduces a *mean reaction rate ratio*, κ, denoting the fraction of the cell volume occupied with fine turbulence structures and a corrected cell reaction rate:

$$R_{\mathrm{EDC}} = \kappa R_{\mathrm{Homogeneous}} \tag{2}$$

where $R_{Homogeneous}$ is the cell reaction rate assuming homogeneous reactant distribution.

Some more low-level TKI approaches introduce a probability density function (PDF) model for each cell reactant concentration. The PDF representation of the reactant concentration can be expressed using an analytical distribution such as the gamma distribution proposed in [21] or numerically by binning the concentration range. Both methods effectively allow the simulation to calculate the cell-averaged kinetic rate by integrating the reactant concentration joint probability and rate from a given kinetic model. For a two-reactant kinetic model $r(x, y)$, the cell reactivity R_{Cell} would be:

$$R_{PDF} = \int_x \int_y r(x, y) g(x, y) dx dy \tag{3}$$

where $g(x, y)$ is the joint probability function for reactants of concentrations x and y.

Implementing $g(x, y)$ can be rather complex. Due to the nature of mixing, reactant concentrations are unlikely to be independent random variables but rather related with a negative covariance. Hence, to implement a simple PDF-based TKI model, the variances and covariances of the reactant and reactant pairs also have to be modelled. Consequently, the PDF-based methods have a wide degree of freedom, and thus their implementation relies on further modelling or experimental fitting. While studies have implemented PDF-based approaches [22], no *off-the-shelf* implementation has been established across liquid phase systems.

IV. METHODOLOGY OF THE PRESENT STUDY

CFD simulations are carried out in STAR–CCM+ replicating in-house experimental studies of barium chloride and sodium sulphate mixing. The concentrations of chemical species are modelled in molality, m_i, using an Eulerian convection-diffusion equation with an optional source term to include reactions:

$$\frac{\partial m_i}{\partial t} = \nabla \cdot (D_{\mathrm{eff}} \nabla m_i) - \nabla \cdot (\mathbf{u}\ m_i) + r_i \tag{4}$$

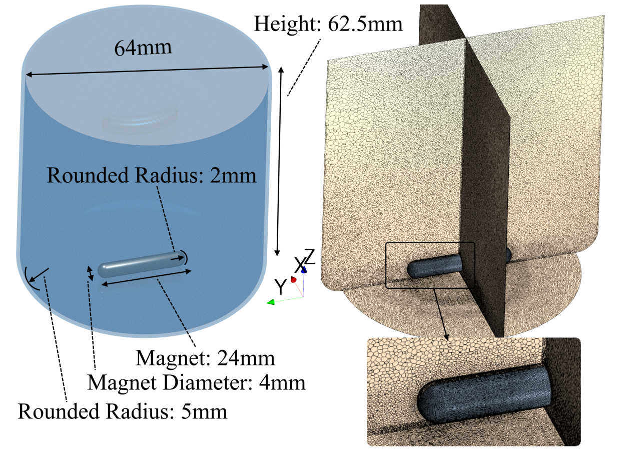

FIG. 1. Illustration of the computational setup for the stirred batch reactor.

where $\mathbf{u}$ is the velocity field. D_{eff} is the effective diffusion coefficient, comprising the molecular diffusion and the sub-grid-scale diffusivity. The fluid velocity is solved through finite-volume modelling of the incompressible Navier-Stokes equations using the LES turbulence modelling framework with the WALE sub-grid-scale model. The implementation of this approach, including the used grid topology and validation steps, is described in more detail in a separate paper by Anabaraonye *et al.* [2].

Two experimental setups are replicated in this work; a mechanically stirred batch reactor and an in-house built Taylor-Couette continuous stirred tank reactor (CSTR) described in detail by Anabaraonye *et al.* [2]. The batch reactor represents a transient reaction where the reactant concentrations are measured as a function of time as they deplete. The CSTR reactor runs at a steady state with a continuous inflow of fresh reactants and outflow of mixed brine that has had an average residence time to react. Reactant concentrations are measured periodically at the outlet.

The batch reactor comprised a Schott Ø86 mm glass bottle of height 176 mm. The reactor was stirred with a round magnet of dimensions; 35 mm in length and 10 mm in diameter at varying rotational rates. The reactor was filled with 400 ml of brine, corresponding to a liquid height of 70 mm at rest.

The CSTR reactor is modelled based on known dimensions illustrated in Figure 2. The reactor has two inlets and two outlets, with one outlet shut. The tank has a static cylindrical outer casing and a rotating inner cylinder. The tank is initially filled with sodium sulphate brine of 1.1 mmol/kg concentration. The first inlet has a steady flow of the same brine at 4.15 ml/min and the second has an inflow of a barium chloride brine of concentration 0.8 mmol/kg at the same flow rate. The active outlet is located vertically above the first inlet. The grid size is defined to ensure a minimum of 20 cells between rotor and stator, resulting in a grid totalling 29.2 M cells.

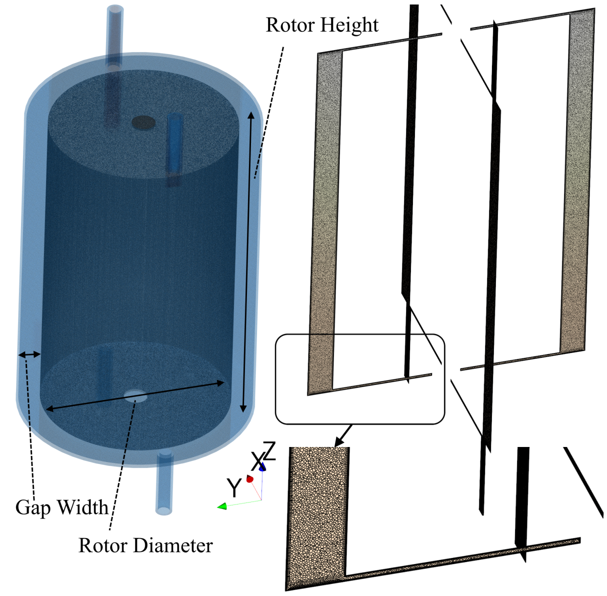

FIG. 2. Illustration of the computational setup for the continuous stirred tank reactor (CSTR). A rotor with outer diameter $D_{\text{Rotor}} = 80$ mm is rotated in a fixed stator with inner diameter $D_{\text{Rotor}} = 98$ mm used leaving a gap width of 9 mm between stator and rotor ($\eta = D_{\text{Rotor}}/D_{\text{Stator}} = 0.82$). Rotor height is 138 mm. Further dimensions not shown on this drawings; cell height (rotor height + 2 mm), inlet tube diameters (5 mm), inlet tube length (30 mm), radial position of inlets (41 mm), shaft diameter (10 mm).

V. PRECIPITATION KINETICS

Various kinetics models are used to estimate the rate at which a chemical reaction occurs as a function of conditions such as reactant concentrations and thermodynamic states. Depending on the scientific scope of a kinetic model, model definitions may include hydrodynamic considerations, e.g., through the Reynolds' number. However, for kinetic models to be widely applicable, parameters should be general rather than specific and thus rely on fundamental physics rather than system-specific statistics.

The most fundamental and idealized models are often built on the law of mass action, applying the simple statistical consideration that the kinetic rate is proportional to the *effective concentrations* of the reactants [23]. The effective concentration was coined *chemical activity* by Lewis [24]. The chemical activity a_i is defined as the reactant corrected by an activity coefficient γ_i that accounts for interactions with other ions in the solution that reduces its reactivity:

$$a_i = m_i \gamma_i \tag{5}$$

The determination of activity coefficients has been studied extensively over the last century and presents an additional source of variability of the kinetics. In this study, we will apply the Pitzer model [25, 26] to estimate the activity coefficients. Rate models based on the law of mass action often comprise a fitted rate constant, k, multiplied with a function, f, that includes the product of the reactant activities as well as thermodynamic attributes such as the temperature, T, and thermodynamic solubility K_p:

$$r = k\ f(K_p, T, a_1, a_2, .., a_N) \tag{6}$$

While some studies add a degree of variability to k, this paper considers the definition of k independent of the concentration state in the mixture and hence, spatially uniform within an isothermal and isobaric fluid.

In this study, we analyze reactor mixing of two brines of dissolved barium chloride ($BaCl_2$) and sodium sulphate (Na_2SO_4), leading to supersaturation and precipitation of barite ($BaSO_4$). Each anion/cation pair has an equilibrium state with corresponding forward and backwards reactions. However, for the studied system, it is reasonable to assume that the two brines are fully dissolved and that the forward reaction of barium sulphate is the only reaction present. Thus the only reaction included in the model is

$$\mathrm{Ba}^{2+} + \mathrm{SO_4}^{2-} \rightarrow \mathrm{BaSO_4} \tag{7}$$

with a kinetic rate modelled using the following second-order model

$$f = a_{\mathrm{Ba}} a_{\mathrm{SO_4}} e^{-\Delta G/RT} \tag{8}$$

where ΔG is the Gibbs free energy driving the reaction [27] defined as

$$\Delta G = RT \ln\left(\frac{a_{\mathrm{Ba}} a_{\mathrm{SO_4}}}{K_{p,\mathrm{BaSO_4}}}\right) \tag{9}$$

where $K_{p,\mathrm{BaSO_4}}$ is the solubility product of barium sulphate set to 1.35×10^{-10} [28]. R is the universal gas constant, and T is the temperature measured in Kelvin.

VI. EVALUATING THE KINETIC HOMOGENEITY STATE

In the present study, the homogeneity of the reactivity is observed using a simple consideration; a kinetic homogeneity index Φ is defined as the ratio of the effective kinetic rate to the kinetic rate which would be observed in a homogeneous mixture. This index bears a resemblance to the definition of activity coefficients or fugacity in its definition and hence, once determined, allows for a linear correction of the reaction state from an idealized state:

$$\Phi = \frac{R_{\mathrm{BaSO_4}}}{R_{\mathrm{BaSO_4|Homogeneous}}} \tag{10}$$

In a reactor with volume, Ω, the net production rate of barium sulphate becomes

$$R_{\mathrm{BaSO_4}} = k \int_{\Omega} f \rho d\Omega \tag{11}$$

Combining (10) with (11) based on the in-situ activities for the numerator and the system-averaged activities for the denominator, a general kinetic homogeneity is obtained:

$$\Phi = \frac{\int_{\Omega} f(K_{p,\mathrm{BaSO_4}}, T, a_{\mathrm{Ba}}, a_{\mathrm{SO_4}}) \rho d\Omega}{\int_{\Omega} f(K_{p,\mathrm{BaSO_4}}, T, a_{\mathrm{Ba|Avg}}, a_{\mathrm{SO_4|Avg}}) \rho d\Omega} \tag{12}$$

As the rate in the denominator denotes a system-averaged and therefore uniform quantity, f_{Avg}, the definition may be simplified to

$$\Phi = \int_{\Omega} \frac{f}{f_{\mathrm{Avg}}} \rho d\Omega \tag{13}$$

For a simple transient reactant mixing system such as the stirred batch reactor, the system-global homogeneity Φ will start at zero for completely segregated reactants and be driven towards one as the reactants are mixed. In contrast, most quasi-steady reactors, such as continuously stirred reactors, will level on a constant homogeneity index below one. It is worth noting that based on the choice of the global system volume in which Φ is calculated, ranges can be shifted, e.g., above one or below zero.

VII. BARIUM SULPHATE BATCH EXPERIMENTS

Batch reactor experiments where two brines are added to a container and stirred are commonly used to determine kinetic models by measuring the transient concentration of either one of the reactants or the product. The transient development of the measured concentrations develops simultaneously with that of the homogeneity state. Hence, in the initial stages of such an experiment, where reactants concentrations are highest, the kinetic rate might be strongly reduced due to inhomogeneity. Such observations were documented by Rizkalla [3], where sulphate and barium chloride were mixed under different stirring conditions leading to significant differences in the observed apparent kinetic rates. In these experiments, apparent kinetic rate constants varied by 32 % from 380 RPM to 1140 RPM and 2 % from 760 RPM to 1140 RPM.

The paper by Rizkalla [3] does not provide sufficient details on the experiment for a meaningful numerical replication attempt. However, an indicative simulation has been carried out to demonstrate the general transient of mixing in a mechanically stirred batch reactor with the same brine compositions and volume at stirring rates of 380 RPM, 760 RPM and 1140 RPM. Figure 3 shows the transient in the first few seconds of stirring for the three rates in terms of the Homogeneity Index. Three contour illustration of the spatio-temporal distribution of local homogeneity defined as the ratio f/f_{Avg} is shown for the least stirred simulation. These simulations were carried out at a coarse grid resolution without a sub-grid-scale kinetic model, and hence, the speed at which the reactor reaches a homogeneity of near-unity is not accurate.

From these indicative simulations, we can observe that super-grid scale Φ reaches 99 % homogeneity after 3 s at 1140 RPM stirring and after 8 s at 380 RPM. Consequently, we conclude that super-grid scale variations alone do not justify the significant difference in apparent kinetic rate between the three stirring speeds.

VIII. BARIUM SULPHATE CSTR EXPERIMENTS

Experiments of barium sulphate precipitation were carried out in the CSTR Taylor-Couette cell and described in [2], the effluent concentrations are shown in Figure 4. The herein presented experimental data highlights that effective reaction rates for well-stirred systems still vary with increased mixing. The paper cited above examines effluent concentration time series for non-reactive brine injection and concludes that on a system scale, the reactor behaves near-perfectly mixed at Reynolds numbers ranging from 1.1×10^4 to 4.3×10^4. While the non-reactive effluents time series are near-independent from the Reynolds number of the reactor, the reactive experiments show a significant difference, suggesting a potential coupling of increased turbulence on the reactivity.

Reactive CFD simulations have been conducted in this study to test the idea that the observed increased reactivity can be explained from an Eulerian rate-homogeneity consideration. Similarly to the batch reactive study, the temporal evolution of the rate-homogeneity parameter Φ from these simulations, shown in Figure 5 illustrates that the macro-scale gradients stabilize quickly with a non-unity asymptotic Φ. However, similar to the conclusions from the batch experiments, these experiments show that the super-grid scale Φ does not explain the difference in reactivity between the two systems.

From the two initial studies, we infer that the resolvable fluid dynamics are not fine enough to capture the effects of turbulence on the kinetics. The observed modelling gap possibly consists of a combination of the unaccounted sub-grid-scale variations and other kinetic aspects enhanced by turbulence, e.g., added molecular level collisions due to increased fluid shear stress. To explore the former, we investigate the introduction of current state-of-the-art sub-grid-scale kinetic correction models and discuss potential areas of improvement in the coming sections.

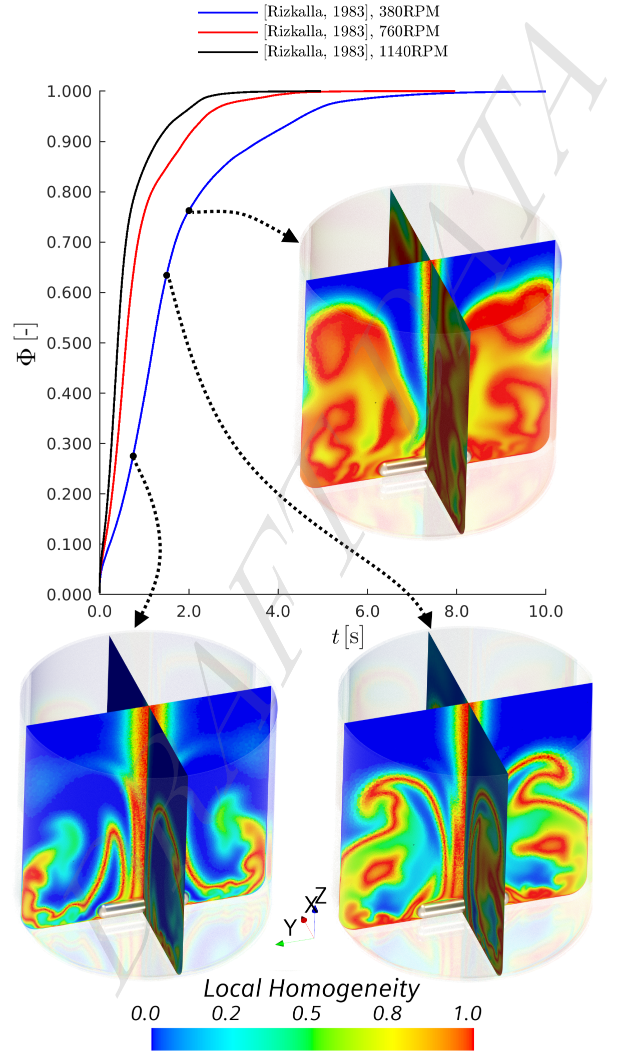

FIG. 3. Simulation of homogeneity development for the batch reactor experiments replicating work by Rizkalla [3]. The graph shows the simulation of the three different rotational speeds. The renderings show the distribution of the local reactivity ($\phi = f/f_{\mathrm{Avg}}$) for three different times (0.75 s, 1.5 s and 2.0 s) for the 380 RPM case.

IX. MODELLING OF SUB-GRID SCALE KINETICS

To examine the impact of the sub-grid variability of reactants and hence kinetic rates, we begin by briefly aligning the concept of sub-grid-scale reaction homogene-

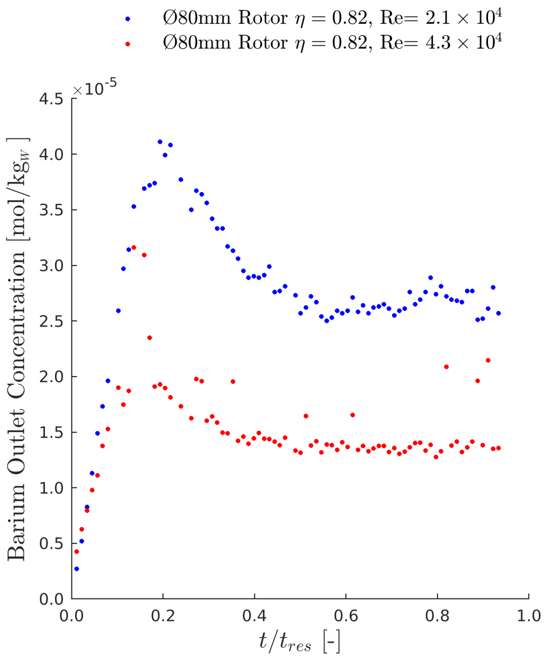

FIG. 4. Experimentally obtained outlet concentration of barium. Taylor-Couette reactor study with $\eta = 0.82$ (Ø80 mm rotor in Ø98 mm cell) at Reynolds numbers 2.1×10^4 and 4.3×10^4 (corresponding to 500 RPM and 1000 RPM). The experimental time t has been normalized by the residence time t_{res}.

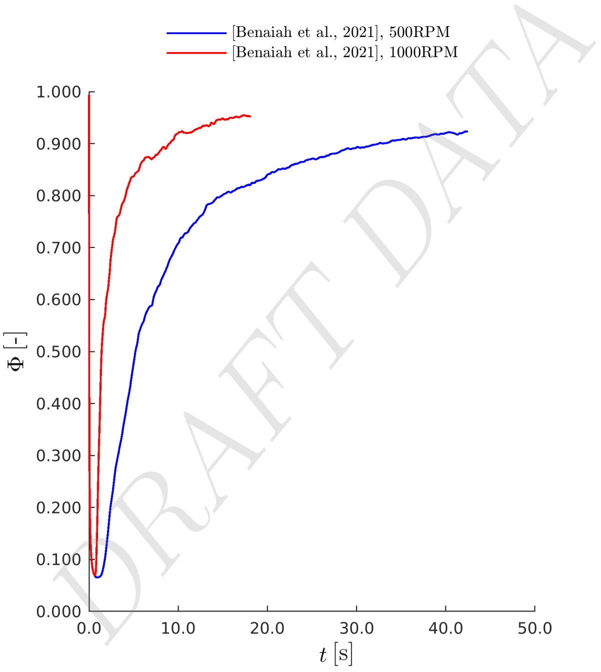

FIG. 5. CFD obtained homogeneity indexes (Φ) as a function of time for a combination of continuously stirred tank reactor (CSTR).

ity with the two previously described approaches, namely the EDC model and PDF-based kinetic modelling. For simplicity, we assume constant density within a cell such that the sub-grid-scale kinetic only varies with f. A kinetic homogeneity-index-based sub-grid-scale reaction rate is defined as

$$\phi_{\text{SGS}} = \frac{f_{\text{Cell}}}{f_{\text{Cell,Avg}}} \equiv \frac{1}{f_{\text{Cell,Avg}}} \int G(x - x', \Delta) f(x_i', t) dx' \tag{14}$$

In summary, it corresponds to treating each cell with sub-grid concentration variations as an individual reactor where ϕ_{SGS} corresponds to Φ from Eq. (10). The effect of ϕ_{SGS} can be included in the reaction term of Eq. (4) as:

$$\begin{aligned} \frac{\partial \overline{m_i}}{\partial t} = \; & \nabla \cdot (\overline{\mathbf{u}}\; \overline{m_i}) \\ & - \nabla \cdot (D \nabla \overline{m_i} + \overline{\mathbf{u}' m_i'}) \\ & + k \phi_{\text{SGS}} f_{\text{Cell,Avg}} \end{aligned} \tag{15}$$

The implementation of such a sub-grid-scale reaction homogeneity is comparative to that of the Eddy Dissipation Concept, where κ is used as a correction factor for the cell reactivity calculated from a perfectly mixed model. In a simulation applying a PDF approach to reactant concentrations f_{Cell} can be directly determined from a stochastic integration of f across the joint probability space of the reactants.

Due to the inaccessibility of computational resources to fully resolve the aforementioned two stirred reactors in a simulation, a much simpler conceptual system is used to compare the EDC and PDF approaches. An accurate benchmark is essential to such comparison, and hence, a numerical domain which is possible to simulate using DNS modelling is devised. For this purpose, a two-inlet baffle-segregated channel flow with a backwards-facing-step at the inlet mixing point is chosen. This domain is illustrated in Figure 6. Dimensions are set with a step height of 0.5 and a total channel height of 1.0 and inlets of width 0.45 and height 0.5 yielding a baffle width of 0.1. All walls are modelled as slip-walls with homogeneous Neumann boundary conditions to avoid unnecessary boundary layer complexity. The inlets are injected with brine of density 1.0 and dynamic viscosity 1.0×10^{-3} flowing at a uniform laminar flow velocity of 1.0. Two different (denoted A, B) passive non-reacting scalars are added to each inlet with concentrations of 1.0 each. The diffusion coefficient of these scalars is set to 1.0.

In order to evaluate the grid resolution, the Kolmogorov η and Batchelor γ_B length scales are estimated by running the grid on a standard $k - \epsilon$ turbulence

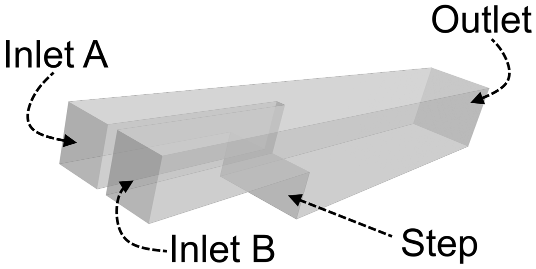

FIG. 6. Illustration of the conceptual backwards-facing-step baffle reactor used to compare existing non-homogeneous kinetic modelling approaches with well-resolved simulation.

model, using the following models:

$$\eta = \frac{\nu^3}{\epsilon} \tag{16}$$

$$\lambda_B = \frac{1}{\mathrm{Sc}} \tag{17}$$

where ν is the kinematic viscosity and ϵ the turbulent dissipation rate from the $k - \epsilon$ transport equations. The timestep is tuned to ensure a maximum Courant number of 0.5 in all the simulations. The simulations are run for a duration of 16 flow-through times, after which the observed Φ values of the entire domain have been quasi-steady for about 6 flow-through times.

The model is simulated at six conditions. The first simulation is solved using a grid size smaller than the Batchelor length scale at all places. The second, third and fourth simulations are run with LES turbulence modelling and a grid size twice the estimated Kolmogorov length scale. The second simulation is run without any added sub-grid-scale kinetic inhomogeneity model. The third and fourth simulations use the EDC and PDF approaches to modelling sub-grid-scale kinetic inhomogeneity. The fifth simulation is run with a standard $k - \epsilon$ RANS model using the same grid size as the three LES simulations. Finally, the same simulation has been run with LES using a novel approach described in the next section.

The third simulation employs the *off-the-shelf* Star–CCM+ implementation of the EDC model based on [20]. This implementation defines the mean reaction rate correction factor as

$$f_{\mathrm{Cell}} = f_{\mathrm{Cell,Avg}} \left(\left(C_l \left(\frac{\nu t_t}{L_t^2} \right)^{0.25} \right)^{-3} \right)^{-1} \tag{18}$$

where C_l is a constant set to 2.1, t_t is the turbulent time scale, and L_t is the turbulent length scale based on the WALE LES model.

For the fourth simulation, a PDF approach is tested. In order to minimize the degrees of freedom in model parameters, a simple gamma distribution is implemented for each scalar concentration using a fixed shape constant ($\alpha = 2$). Furthermore, the covariance of the scalars A and B is approximated from the dot-product of their respective gradient vectors. This implementation of the covariance is a simple attempt to account for a covariance closer to negative unity at mixing fronts and a covariance closer to unity where premixed brines are mixed with, e.g., pure water zones.

The simulated Φ values are plotted in Figure 6. The comparison shows an approximately 20 % difference in Φ between the DNS and LES when no kinetic sub-grid-scale model is used in the LES simulation. The EDC model yields a small improvement but does not capture the full magnitude of the sub-grid scale inhomogeneity.

The PDF-based approach to sub-grid-scale variations yields promising results. However, it should be noted that in order to achieve reasonable covariances and hence ϕ values, the dot-product of the gradients were corrected with an arbitrary tuning factor, and hence, the accuracy of the results hinges on this tuning parameter.

X. PROPOSED 1-EQUATION SUB-GRID-SCALE KINETICS MODEL

A transport-equation-based model is proposed as a more direct implementation of a sub-grid-scale kinetic homogeneity. This model combines the covariance considerations from the above-used PDF model and the methodology used in the most commonly applied typical turbulence modelling approaches.

From a basic physical consideration, ϕ_{SGS} has to have the following properties:

1. Unity for homogeneous reactants, zero for completely unmixed reactants
2. May exceed unity but can only be negative if f can be negative
3. Is transported through convection and diffusion
4. Decreases asymptotically towards zero if concentration gradient vectors of the reactants are in an opposite direction
5. Decays exponentially towards unity with a decay constant correlated with molecular and turbulent diffusion

The first two properties are directly observable from Eq. (14). The convection-diffusion properties are intuitive and easily verifiable from numerical simulations. A numerical experiment is carried out and described in the supplementary material. This experiment provides a rough idea of the magnitude of a ratio between the molecular diffusivity of the reactants and the diffusivity of ϕ_{SGS}. This ratio is estimated to be $C_d = 2.9$.

Numerical experiments are also carried out in the supplementary material to verify the fourth property; when a cell observes reactant concentration gradients from opposite directions, i.e., when it is located on a mixing interface between two different brine compositions, then the inhomogeneity of that cell increases. This change in cell-internal concentration covariance due to mixing interfaces is the primary principle driving inhomogeneous kinetics. From simulations described in the supplementary material, the production constant is estimated to be $C_p = 7.4$.

Finally, within the cell, diffusion gradually reduces the gradients and thus makes the inhomogeneous mixture more homogeneous. The balance between this fifth and fourth property controls the transient and stability of the homogeneity of the system. From a third simulation described in the supplementary material, the decay constant is estimated to be $C_\epsilon = 15$. The rate of this transition is driven by the diffusion properties of the reactants and the interface folding and stretching between the brines.

The above-stated properties allow a simple proposal for a ϕ_{SGS} transport equation that is easily implemented in a CFD framework:

$$\begin{aligned}\frac{\partial \phi_{\mathrm{SGS}}}{\partial t} = {} & \nabla\cdot(\bar{\mathbf{u}}\,\phi_{\mathrm{SGS}}) \\ & - \nabla\cdot C_d D_{\mathrm{avg}}\nabla\phi_{\mathrm{SGS}} \\ & - C_\epsilon D_{\mathrm{avg}}\Delta^2(\phi_{\mathrm{SGS}}-1) \\ & + C_p\frac{\phi_{\mathrm{SGS}}}{f_{\mathrm{Avg}}}\Delta^2\nabla\overline{m_{\mathrm{Ba}}}\cdot\nabla\overline{m_{\mathrm{SO_4}}}\end{aligned} \tag{19}$$

where D_{avg} is the average effective (molecular and turbulent) diffusivity of the reactants, Δ is a cell length scale set to the cubic root of the cell volume.

To compare this suggested approach with the previous two models, a simulation of the backwards-facing step using this approach is included in Figure 7. The model shows promising results, albeit yielding a slightly lower ϕ_{SGS} than expected.

XI. CONCLUSION

Accounting for variation in the kinetics within mixed brine reactive systems is a significant challenge but also presents a scientific necessity. This study outlines that partially resolved simulations such as LES-based numerical models do not capture sub-grid-scale variability, which for liquid phase conditions, can be highly significant due to high Schmidt numbers. As the availability of computational resources increases, numerical models can resolve increasingly fine gradients. However, in most industrial mixed brine systems, the combination of high Reynolds numbers and high Schmidt numbers makes the Batchelor length scale so small that such simulations are infeasible at the time of writing.

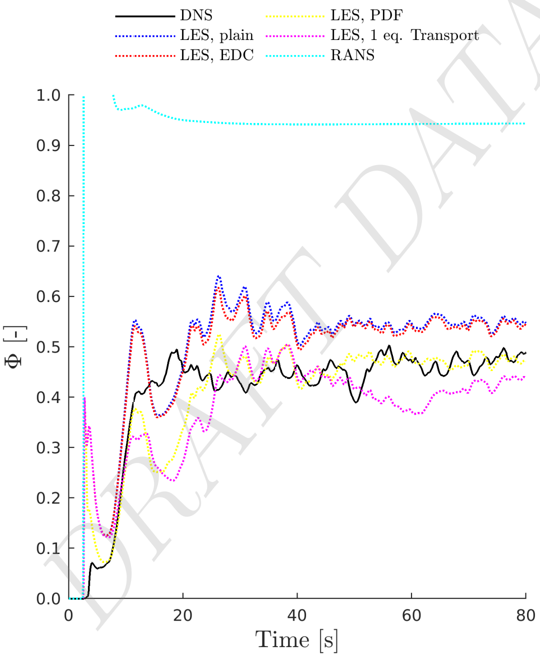

DRAFT DATA

FIG. 7. Comparison of simulation of the backwards-facing step reactor using four different modelling approaches; DNS with resolution down to the Batchelor length scale, LES with no sub-grid-kinetics model (plain) as well as LES with EDC and with a PDF sub-grid-scale kinetics model

We compare two known methods for modelling the sub-grid-scale variations in the kinetic rates caused by cell reactant concentration variations. The EDC method is a well-established model often implemented in, e.g., combustion simulations. While we did not tune parameters to fit data, our preliminary conclusion is that the model does not accurately capture the sub-grid variations in the liquid phase kinetics. We show promising results with the probability density function representation of the reactant concentrations and a covariance approach accounting for the brine displacement in mixing layers. However, due to sparse literature and empirical data on such implementation, our success somewhat hangs on tuning the covariance model. Finally, we compare the LES-based methods to a typical RANS implementation, demonstrating that non-temporally and spatially resolving methods cannot capture the effects of temporal and spatial gradients on reactivity.

Additionally, we propose a transport equation approach in line with typical sub-grid-scale models estimating, e.g., droplet sizes and turbulent kinetic energy. This model again shows promising results. While it has a set of tuning parameters attached, using simple estimates from basic simulations gives usable parameters that hold a physical meaning. This makes the model more self-sufficient and less reliant on empirical observations.

In summary, we highlight the prospects of accurate spatio-temporal modelling of kinetics in reactive systems with LES by implementing sub-grid-scale models on a known miscible brine system where DNS is achievable. However, the field of sub-grid-scale modelling has proven vastly uncovered for use in liquid-phase systems. Therefore, we emphasize the importance of multidisciplinary research in coupling fluid dynamics and chemical engineering. The examples used in this paper barely scratch the complexity of spatio-temporal effects in mixed brine systems. Other significant spatio-temporal effects, such as wall or surface interaction, are omitted in this study.

Better insight and ability to perform accurate spatio-temporal analyses of reactive systems can better qualify reactive experiments and help determine reaction models with higher accuracy. It can also significantly improve reactive prediction models such as scale formation or corrosion studies, or optimization studies for industrial chemical process reactors.

DRAFT NOTES

This manuscript is currently in writing, and the described studies are in progress. This section has been added because the manuscript, in its current state, is attached to a paper-based PhD thesis. The following points outline the author's current list of remaining tasks to complete this research study and manuscript:

1. Simulation of in-house batch experiments as replacement for the *illustrative* simulations done replicating work by Rizkalla [3]
2. Grid sensitivity study of batch and CSTR reactor to confirm the hypothesis that further grid-refinement will reduce $\Phi(t)$
3. Test parameter tuning and sensitivity of the EDC, PDF and proposed transport equation approach to sub-grid-scale reaction inhomogeneity
4. Simulation of both batch experiments and CSTR experiments using proposed and tested sub-grid-scale reaction inhomogeneity approaches
5. Generalization of the gradient dot-product covariance approach to n reactants
6. More thorough validation of computational models through grid independence checks

[1] R. K. Thakur, C. Vial, K. D. Nigam, E. B. Nauman, and G. Djelveh, Static mixers in the process industries - a review, Chem. Eng. Res. Des. **81**, 787 (2003).

[2] B. U. Anabaraonye, J. R. Bentzon, I. Khaliqdad, K. L. Feilberg, S. I. Andersen, and J. H. Walther, The influence of turbulent transport in reactive processes: A combined numerical and experimental investigation in a Taylor-Couette reactor, Chem. Eng. J. **421**, 129591 (2021).

[3] E. N. Rizkalla, Kinetics of the crystallisation of barium sulphate. Effect of additives, stirring rate and barium:sulphate ratio on the rate of precipitation, J. Chem. Soc., Faraday Trans. 1 **79**, 1857 (1983).

[4] O. Levenspiel, Chapter 16 - Earliness of Mixing, Segregation, and RTD, in *Chem. React. Eng.* (John Wiley & Sons, 1962) pp. 350–365.

[5] J. M. Ottino, *The kinematics of mixing: Stretching, chaos, and transport* (Cambridge Univ. Press, 1989).

[6] D. H. Kelley and N. T. Ouellette, Separating stretching from folding in fluid mixing, Nature Physics **7**, 477 (2011).

[7] K. Southerland, R. Frederiksen, W. Dahm, and D. Dowling, Comparisons of mixing in chaotic and turbulent flows, Chaos, Solitons & Fractals **4**, 1057 (1994), Special Issue: Chaos Applied to Fluid Mixing.

[8] J. W. Mullin, *Crystallization*, 4th ed. (Butterworth-Heinemann, Oxford, 2001).

[9] P. M. Wheat and J. D. Posner, Quantifying mixing using equilibrium reactions, Phys. Fluids **21**, 037101 (2009).

[10] P. Rao, A. Duggleby, and M. A. Stremler, Mixing analysis in a lid-driven cavity flow at finite Reynolds numbers, J. Fluids Engng. **134**, 10.1115/1.4006361 (2012).

[11] A. D. Stroock, S. K. W. Dertinger, A. Ajdari, I. Mezić, H. A. Stone, and G. M. Whitesides, Chaotic mixer for microchannels, Science **295**, 647 (2002).

[12] G. K. Batchelor, Small-scale variation of convected quantities like temperature in turbulent fluid Part 1. General discussion and the case of small conductivity, J. Fluid Mech. **5**, 113 (1959).

[13] D. C. Wilcox, *Turbulence modeling for CFD* (DCW Industries, Inc, 1993).

[14] D. Guha, Ramach, P. A. Ran, M. P. Dudukovic, and J. J. Derksen, Evaluation of large eddy simulation and Euler-Euler CFD models for solids flow dynamics in a stirred tank reactor, AIChE J. **54**, 766 (2008).

[15] D. A. Lysenko, I. S. Ertesvåg, and K. E. Rian, Numerical simulations of the Sandia flame D using the eddy dissipation concept, Flow Turbul. Combust. **93**, 665 (2014).

[16] P. Priyadarshini, A. Sofianopoulos, S. Mamalis, B. Lawler, D. Lopez-pintor, and J. E. Dec, Understanding partial fuel stratification for low temperature gasoline combustion using large eddy simulations, Int. J. Engine Res. **22**, 1872 (2021).

[17] M. Germano, U. Piomelli, P. Moin, and W. H. Cabot, A dynamic subgrid-scale eddy viscosity model, Phys. Fluids **3**, 1760 (1991).

[18] F. Nicoud and F. Ducros, Subgrid-scale stress modelling based on the square of the velocity gradient tensor, Flow, Turbul. Combust. **62**, 183 (1999).

[19] Y. Kang and J. X. Wen, Large eddy simulation of a small pool fire, Combust. Sci. and Tech. **176**, 2193 (2004).

[20] B. Magnussen, On the structure of turbulence and a generalized eddy dissipation concept for chemical reaction in turbulent flow, in *19th Aerospace Sciences Meeting* (1981).

[21] E. Yee and R. Chan, A simple model for the probability density function of concentration fluctuations in atmospheric plumes, Atmos. Environ. **31**, 991 (1997).

[22] J. Bakosi, P. Franzese, and Z. Boybeyi, Probability density function modeling of scalar mixing from concentrated sources in turbulent channel flow, Phys. Fluids **19**, 115106 (2007).

[23] C. M. Guldberg and P. Waage, Ueber die chemische affinität. § 1. Einleitung, J. prakt. Chem. **19**, 69 (1879).

[24] G. N. Lewis, Outlines of a new system of thermodynamic chemistry, Proc. Am. Acad. Arts Sci **43**, 259 (1907).

[25] K. S. Pitzer, Thermodynamics of electrolytes. I. Theoretical basis and general equations, J. Phys. Chem. **77**, 268 (1973).

[26] K. S. Pitzer, Electrolyte theory - improvements since Debye and Hueckel, Acc. Chem. Res. **10**, 371 (1977).

[27] G. N. Lewis and M. Randall, *Thermodynamics, Revised by Kenneth S. Pitzer and Leo Brewer*, 2nd ed. (McGraw-Hill, New York, 1961).

[28] C. A. J. Appelo, Principles, caveats and improvements in databases for calculating hydrogeochemical reactions in saline waters from 0 to 200°C and 1 to 1000atm, Appl. Geochem. **55**, 62 (2015), geochemical Speciation Codes and Databases.

6 Conclusion and ongoing work

This chapter serves to summarize the outcomes of each individual concrete research study, of the project in a broader context, and of the unpublished studies with perspectives on commenced and planned areas of future research.

6.1 Conclusions from the published studies

From a general review of the governing physics supported by recent and current research, it is evident that scale formation and crystallization in an industrial context is a complex multi-disciplinary challenge. In my PhD studies, I have sought to add knowledge from the field of fluid dynamics and computational methods to both qualitatively and quantitatively unravel some of the complexities arising from spatio-temporal effects of the flow in which the scale-forming reactions occur.

Motivated by concrete challenges faced in hydrocarbons production in the North Sea, barium sulphate deposition under comparable flow conditions has been considered. These challenges occur under a turbulent multi-phase flow of mixtures with a wide range of electrolytes dissolved. As parallel studies are undertaken to study the significance of complex brine compositions, the scope has been reduced to simple brines consisting of dissolved sodium sulphate and barium chloride.

The first research paper explores the influence of multi-phase flow conditions on the scale formation rates in oil-water flow. It was conducted to evaluate relatively novel methods to obtain key quantitative measures such as droplet size and surface wetting. The ability to predict these measures can, for example, help predict the effects of different water cuts and the placement and design of flow-obstructing equipment. The concrete outcome of the research paper was validation of the ability of the tested methods to obtain such data with a lower requirement for supporting experimental studies under the given flow conditions.

The second paper explores the influence of varying turbulence intensity on reactant transport and mixing in the aspect of barite deposition. This paper is the first outcome of a decision taken to build a novel reactor to provide data for combined numerical and experimental studies into scale formation under varying hydrodynamic conditions. As a first step in a range of studies in this reactor, the study focuses on validating a structured methodology for CFD simulations on the reactor. The simulations use a combination of large eddy simulations (LES) to harvest microscale statistical insights, and Reynolds stress models (RSM) to produce Reynolds averaged simulation results. The outcome of this study is a foundation for concrete studies into flow-reactive studies with a wide degree of freedom to examine different flow regimes, surface characteristics and chemical combinations.

Additional to a novel reactor accompanied by a validated CFD approach, the paper delves into ways of deriving relevant statistical insights from microscale LES simulations for subsequent use in Reynolds averaged simulations. We illustrate a model for obtaining an estimate for the turbulent Schmidt number from LES simulations, although these were subjected to a high degree of variability from our results. We also suggested a new turbulence-mixing quantity, namely the turbulent Peclét number, which we compared across different experiments with varying degrees of turbulence. Observing this turbulent Peclét number from non-reactive simulations shows that microscale mixing was significantly increased at the higher Reynolds number, even between two turbulent conditions. These findings align with observations from reactive experiments showing a significant increase in reactivity between the two cases.

The third paper has been conducted to take the first steps to enhance the phenomenological understanding of scale formation in different flow conditions over different surfaces. A simple sample of two different surface designs with two flow rates has been used to generate four different experimental situations. CT scans have been obtained after three different experimental durations and reconstructed to 3D surfaces, allowing us to visualize scale growth accurately. The CT reconstructions are supported by simple numerical simulations of the reactive transport in the cell without attempting predictive precision. The paper presents a qualitative review of a range of previous studies, with their conclusions discussed through relatively simple means of experimental and numerical observations along with an inference of the characteristics of the results we obtained.

Through the publications mentioned above, our phenomenological understanding of the impact of fluid dynamics on the formation and growth of scale has been improved. Furthermore, a solid basis is laid for further research into concrete unresolved questions. This has led to the conduction of a range of experiments and simulations that will lead to more publications on the subject in the coming months and years.

6.2 Prospective outcomes of ongoing and future work

At the time of this writing, large efforts have been made to progress the state of knowledge in the field of flow-kinetic modelling surrounding the area of scale precipitation. The devising of the Taylor-Couette reactor and the models to simulate its operation has a range of prospective studies lined up.

Furthermore, the studies into surface deposition using CT morphology has left a range of questions unanswered, to which a new range of experiments, with finer time resolution of in-situ deposition scans are possible. These studies will allow us to make much more accurate flow modelling including the formation of crystals and how fluid forces act on those.

6.2.1 The significance of spatio-temporal variability on global reaction kinetics

Attached in Chapter 5, a manuscript presents a study-in-progress on accurate modelling of inhomogeneous reaction kinetics within stirred reactors. Stirred reactors are used widely to examine kinetic rates. Stirring is an essential process to mix miscible brines added at the beginning of the experiment or continuously through the experiment. The current work attempts to use CFD simulations to examine the mixing rate of the brines to measure the effect on reactivity. It aims to bridge the difference between the ideal state of mixing, where reactant concentrations and thus kinetic rates are uniform throughout the reactor, and the actual state, where the global kinetic rates are reduced due to partial separation of the reactants.

The study sets out from simple considerations about the local and global scale kinetics. From CFD simulations, super-grid scale inhomogeneities can be explicitly monitored as a function of time, whereas the sub-grid scale variations are harder to estimate. Different turbulence-kinetic interaction models are examined and compared to experimentally obtained rates at different stirring intensities. The final goal of the work is to provide the reader with a structured method for obtaining the mixing state time series to account for reactive inhomogeneity in kinetic studies.

6.2.2 Decoupling shear forces from turbulence in flow-kinetic interaction and surface deposition

In many studies, a simple challenge is faced when examining the influence of fluid dynamics on the formation, growth, attachment and detachment of crystals on surfaces. Namely that significant flow properties such as shear and turbulence are tightly coupled. This coupling occurs naturally in fluids with constant viscosity; fluid shear is directly correlated with the velocity gradient and increased velocities generally destabilizes the flow. The Taylor-Couette reactor offers a way of retaining flow stability by narrowing the gab between the rotor and stator. In summary, by increasing the rotor diameter, the narrower gap will increase the shear stresses and, at the same time, reduce the Reynolds number of the flow.

At the time of writing, nine sets of experiments have been carried out using three different rotor sizes. Hopefully, by analyzing and simulating these experiments, we can provide meaningful data on how increased shear stress affect early deposition, decoupled from the added transport of reactants from bulk to surface observed in a turbulent flow. This can verify or negate the theory that early deposition is enhanced by shear due to increased molecular collisions on the solid surface.

6.2.3 In-situ measurements and simulations of surface crystal growth

The third published paper infers that the surface morphology affects the energy barrier to initiate surface nucleation and growth. A reactor has been devised to verify and quantify such influence and estimate the required saturation state for surface nucleation to onset onto different surfaces. The reactor works by injecting sodium sulphate and barium chloride in two parallel separated channels. The channels merge while the height of the cell is expanded so that the brines experience a “backwards-facing step”. Such a step has been studied extensively from a fluid dynamic perspective. Hence, numerical modelling requirements are well-understood, and a quasi-static model for the flow can be obtained.

Behind the step, a “shadow zone” is present in which the fluid recirculates. Consequently, the majority of the injected brine passes over this zone. A quantitative measure is obtained by comparing the distance from the step to the first observed scale. This measure can be used to validate deposition models within numerical simulations. By placing different surfaces at the bottom of the step and by using different brine concentrations, it is the hope to generate a series of data that will serve to validate complex kinetic models from well-validated flow solutions obtained through CFD.

Technical
University of
Denmark

Nils Koppels Allé, Building 403
2800 Kgs. Lyngby
Tlf. 4525 1700

www.contruct.dtu.dk